

DISS. ETH NO. 26617

Development of energy-selective fast neutron imaging for nondestructive elemental analysis

A thesis submitted to attain the degree of
DOCTOR OF SCIENCES of ETH Zürich
(Dr. sc. ETH Zürich)

Presented by

Benoît Pierre Soubelet

MSc EPF Lausanne - ETH Zürich - MSc Ecole Centrale de Lille
born on 03.02.1991
citizen of France

accepted on the recommendation of

Prof. Dr. Horst-Michael Prasser, examiner
Prof. Dr. Igor Jovanovic, co-examiner
Dr. Volker Dangendorf, co-examiner

2020

A mes parents.

Acknowledgements

First and foremost, I would like to thank Prof. Dr. Horst-Michael Prasser, Dr. Robert Adams, and Dr. Robert Zboray for their support throughout the project, for the ever fertile discussions we had together, and their inspiring insight. Their dedication and their knowledge truly guided me through the highs and lows of this study.

I could of course not omit my office colleagues, Heiko Kromer, who joined me very early in this adventure, and Alexander Wolfertz, who hopped in on the way. Thanks to their humor and friendliness, the long cold winters and hot summers of PSI felt like a breeze. Working together, we brought the neutron generator and the projects around it further than anyone before and it is rewarding to see that there is a next generation of curious minds ready to take them over. I wish them good luck and godspeed!

The LTH (and now LRT) thermohydraulic technical team provided me invaluable help, and I'm especially filled with gratitude towards Max Fehlmann, Wilhelm Bissel, Simon Suter, and Dr. Domenico Paladino. I have an immense respect for their knowledge and know-how, and above all for the simplicity with which they would show interest for my project and help me. I am also thankful to Dr. Gregory Perret for his help and his kindness and to Dr. Robert Eichler and his team from the Laboratory of Radiochemistry for their help in the preparation of the samples. The study with the high-resolution fast neutron spectrometer FNS-1 would not have been possible without the precious support of Dr. Chris Franklin and Graham Daniels - from the South African Nuclear Energy Corporation SOC Limited (NECSA) - for which I am very grateful. I am in general filled with gratitude towards both teams at ETHZ and PSI, and in particular towards their extraordinary secretaries - Nora Kerenyi, Martina Christoffel, Fiorella Meyer, Renate von Doesburg, and Andrea Mohr - who helped me navigating the endless sea of red tape.

Life would not be as fun without friends. I am very lucky to still count childhood friends - Flavien, Justine, Barbara, Thomas - as close friends. More than twenty years, and still going strong! I also met so kind and generous people in Switzerland: Aija, Corinne, Valentyn, Dionysios, Vera, Heiko, Abhishek, ... the list is too long! Thank you for the countless hikes, bike rides, ski sessions, Limmat boat trips, ... and the many more to come!

Finally, I am eternally grateful to my family. For a proper dedication, I will thereafter continue in French: les mots seront insuffisants pour retranscrire la profondeur de mes sentiments, mais je profite de cette occasion unique pour vous exprimer ma gratitude, à vous tous qui faites partie de la famille. J'ai une chance inouïe d'avoir un entourage si généreux et si aimant, qui m'a toujours soutenu et encouragé dans tous mes projets. Vous êtes extraordinaires! Mes jumelles préférées: Claire et Pauline. Mes grands-parents adorés: Beñat, Chantal, Mamie, Nany, Papy, Rémy. Mes oncles, tantes et cousins et petits-cousins favoris - Alain & Marie-Laure, Camille, Stéphanie et leurs bouts de chou qui ne cessent de grandir - Ernestine, Léon et Paul - Éric & Marie-Laure, Camille et Sophie. Je n'oublie pas les pièces rapportées bien sûr: Adrien, Cécile, Jean-Philippe et Valentin! Et finalement, mes parents chéris, Jacques et Véronique. Votre amour, votre générosité, votre bienveillance et votre rigueur morale sont des phares flamboyants qui guident mes pas chaque jour. Je vous dois tout et je porte avec fierté l'étendard des valeurs que vous m'avez transmises.

Abstract

This study presents an imaging technique with material decomposition ability using a compact deuterium-deuterium (DD) neutron generator. The method takes benefit from the variation of the neutron energy as a function of the emission angle. At the available deuteron energy of the in-house DD source of 80 keV, the deuteron energy varies from about 2.2 MeV in the backward direction in relation to the incoming deuteron to about 2.8 MeV in the forward direction. This feature is used to measure the neutron beam attenuation through a given sample at various energies. Since neutron cross-sections are characteristic for a given element and strongly depend on the neutron energy, a unique material-dependent contrast can be obtained at each energy. By combining the information obtained from multiple energies, a linear system of equations can be generated. The unknowns of this system of equations are the concentrations of the elements in the sample. The solution of this system of equations yields the composition of the sample. This elemental decomposition method can be combined with a tomographic imaging technique, which allows obtaining a spatial mapping of the elemental composition of an interrogated heterogeneous object.

The first part of this report focuses on the theoretical and experimental characterization of the neutron field around the generator. The developed arrangement allows performing measurements remotely and in an automated way. Its layout is presented, along with the angle-dependent neutron spectrum. Tests with selected representative material samples provided a proof of principle of the energy-selective element detection capability of this approach.

In the second chapter, a large number of material samples is investigated with regard to their neutron attenuation in the available energy range. The measurements are compared with an existing cross-section database. The agreement between the measurements and the attenuation calculated using the database can serve different purposes. For some elements, the tabulated data is sparse, and the measurements may contribute to an extension of the state of knowledge. Other already well-characterized elements confirm that the measurements are meaningful, although room for further improvement of the measuring setup and its signal acquisition technique was identified. An important factor affecting the accuracy of the overall measurement setup is the electrical perturbation originating from the radio frequency generator of the deuterium plasma source. Some of the observed discrepancies are reduced by careful calibration.

The third section deals with applying the elemental decomposition approach to tomographic imaging with two test cases. For this purpose, an extended neutron detection system in the form of an arc-shaped array of individual detectors is used. The individual detectors are made of plastic scintillators coupled to silicon photomultipliers. The results of tomographic 2D element mapping within a cross-sectional view of the selected heterogeneous test samples are presented and discussed. Elemental decomposition was successful for several of the materials interrogated.

Finally, the last chapter of the present report contains proposals for future improvement of the developed technique, which could result, for example, in a speeding up of the measurement, and an increase of the element-sensitivity by extending the energy range of the available neutrons.

Zusammenfassung

Die vorliegende Arbeit präsentiert eine elementsensitive Bildgebungstechnik auf Basis einer kompakten Deuterium-Deuterium (DD) Plasmafusionsneutronenquelle. Das Verfahren nutzt die Variation der Energie der generierten Neutronen in Abhängigkeit von deren Emissionswinkel. Die eingesetzte laboreigene DD Neutronenquelle liefert bei einer Deuteronenenergie von 80 keV in Gegenrichtung zu den ankommenden Deuteronen Neutronen von etwa 2.2 MeV, in Vorwärtsrichtung eine Neutronenenergie von etwa 2.8 MeV. Diese Eigenschaft der Quelle wird für die Messung der energieabhängigen Schwächung der Neutronenstrahlung genutzt. Da verschiedene Elemente charakteristische Wirkungsquerschnitte aufweisen, die in spezifischer Weise von der Neutronenenergie abhängen, kann bei jeder verwendeten Neutronenenergie ein eindeutiger materialspezifischer Kontrast erzielt werden. Wird die Messung bei unterschiedlichen Emissionswinkeln und somit bei Variation der Neutronenenergie wiederholt, kann ein lineares Gleichungssystem erhalten werden, dessen Unbekannte die Konzentrationen der in einer Probe enthaltenen Elemente darstellen. Die Lösung dieses Gleichungssystems ergibt die Zusammensetzung der Probe. Eine Kombination mit einer tomographischen Bildgebung erlaubt schliesslich eine räumliche Kartierung der Elementzusammensetzung eines untersuchten heterogenen Objekts.

Der erste Teil der Arbeit beschreibt die theoretische und messtechnische Charakterisierung des Neutronenfeldes in der Umgebung des Generators. Die entwickelte Versuchseinrichtung erlaubt die Durchführung von voll ferngesteuerten Messungen. Sie wird ausführlich beschrieben, zusammen mit den ermittelten winkelabhängigen Neutronenspektren. Erste Tests mit ausgewählten, repräsentativen Materialproben erlaubt es, die Machbarkeit der angestrebten energiselektiven Elementdetektion nachzuweisen.

Im zweiten Kapitel wird eine grössere Zahl unterschiedlicher Materialproben hinsichtlich der energieabhängigen Schwächung des Neutronenstrahls untersucht. Die Messergebnisse werden mit verfügbaren Wirkungsquerschnittsdatenbanken verglichen. Die Übereinstimmung zwischen der gemessenen und der mit Hilfe der Datenbank berechneten Schwächung ist unterschiedlich gut. Einige Elemente sind in dem untersuchten Energiebereich noch schlecht tabuliert und die Messungen können zur Erweiterung des Wissensstandes beitragen. Andere, gut bekannte Elemente liefern eine Bestätigung der Messergebnisse, wobei Verbesserungspotential besteht. Ein wichtiger Störfaktor ist die Hochfrequenzversorgung der Deuteriumplasmaquelle. Einige der beobachteten Diskrepanzen wurden durch eine sorgfältige Kalibrierung reduziert.

Der dritte Abschnitt beschäftigt sich mit der Kombination der Elementdetektion mit tomographischer Bildgebung. Zu diesem Zweck wurde das Neutronendetektionssystem zu einem bogenförmigen Detektorfeld ausgebaut. Die einzelnen Detektoren bestehen aus Plastiksintillatoren mit angekoppelten Siliciumphotonenvervielfachern. Die Ergebnisse einer zweidimensionalen Kartierung der Elementzusammensetzung von ausgewählten heterogenen Testobjekten wird vorgestellt und diskutiert. Die Elementdetektion war bei mehreren der abgefragten Materialien erfolgreich.

Abschliessend präsentiert die Arbeit Überlegungen für eine zukünftige weitere Verbesserung der entwickelten Bildgebungstechnik. Interessante Aspekte sind die Verringerung der Messzeiten, die Erhöhung der Elementsensitivität durch Erweiterung des überstrichenen Energiebereichs.

Résumé

Cette étude présente une technique d'imagerie avec capacité de décomposition des matériaux utilisant un générateur compact de neutrons au deutérium-deutérium (DD). La méthode tire parti de la variation de l'énergie des neutrons en fonction de leur angle d'émission. La source sur-mesure de neutrons DD utilisée fournit typiquement une accélération électrostatique de 80 kV, ce qui correspond à une gamme d'énergie des neutrons variant de 2.2 MeV dans la direction opposée au deuteron entrant, jusqu'à 2.8 MeV dans la direction alignée avec le deuteron entrant. Cette caractéristique unique de la source est utilisée pour mesurer l'atténuation du faisceau de neutrons à travers un échantillon donné à différentes énergies. Puisque les sections efficaces des neutrons sont propres à chaque élément et dépendent fortement de l'énergie des neutrons, un contraste unique dépendant du matériau peut être obtenu à chaque énergie. En combinant les informations obtenues à différentes énergies, un système linéaire d'équations peut être généré. Les inconnues de ce système d'équations sont les concentrations des éléments dans l'échantillon. La solution de ce système d'équations donne la composition de l'échantillon. Cette méthode de décomposition est ensuite associée à une technique d'imagerie tomographique, qui permet d'obtenir une cartographie spatiale de la composition élémentaire de l'objet hétérogène interrogé.

La première partie de ce rapport porte sur la caractérisation théorique et expérimentale du champ neutronique autour du générateur. Le dispositif mis au point a permis d'effectuer des mesures automatiques et télécommandées. Son agencement est présenté, ainsi que le spectre neutronique en fonction de l'angle d'émission. Des essais avec des échantillons de matériaux soigneusement sélectionnés fournissent une preuve de principe de la détection d'élément avec sélection en énergie du faisceau de neutrons.

Dans le deuxième chapitre, l'atténuation du faisceau neutronique dans la gamme d'énergie disponible est étudiée pour un grand nombre d'échantillons homogènes de matériaux. Les mesures sont comparées avec une base de données de sections efficaces existantes. La concordance entre les mesures et l'atténuation calculée à l'aide de la base de données peut servir à différentes fins. Pour certains éléments, les données tabulées sont peu nombreuses et les mesures peuvent contribuer à une extension de l'état des connaissances. D'autres éléments, déjà bien caractérisés, confirment que les mesures sont significatives, bien qu'une amélioration du dispositif de mesure et de la technique d'acquisition des signaux soit encore souhaitable. Un facteur important qui affecte l'exactitude des mesures est la perturbation électrique provenant du générateur de radiofréquences excitant le plasma de deutérium. Certains des écarts observés ont été réduits grâce à un étalonnage soigneux.

La troisième section traite de la combinaison de la décomposition élémentaire avec l'imagerie tomographique. A cette fin, le système de détection des neutrons a été amélioré pour former un réseau de détecteurs individuels en forme d'arc. Les détecteurs individuels sont constitués de scintillateurs en plastique couplés à des photomultiplicateurs en silicium. Les résultats d'une cartographie d'éléments 2D dans une vue en coupe d'échantillons hétérogènes sélectionnés sont présentés et discutés. La décomposition élémentaire a donné d'excellents résultats pour plusieurs des matériaux interrogés.

Enfin, le dernier chapitre du présent rapport contient des propositions pour une amélioration fu-

ture de la technique mise au point, qui pourrait se traduire, par exemple, par une réduction du temps de mesure, et par une augmentation de la sensibilité aux éléments en élargissant la gamme d'énergie des neutrons générés.

Contents

Acknowledgements	v
Abstract	vii
Zusammenfassung	ix
Résumé	xi
Table of contents	xv
List of abbreviations	xvii
List of symbols	xviii
List of Figures	xxi
List of Tables	xxii
1 Introduction	3
1.1 Imaging with ionizing radiation as a nondestructive testing technique	3
1.2 Fundamentals of uncharged particle interactions with matter	3
1.3 From Beer-Lambert to quantitative elemental analysis	4
1.4 Interactions of uncharged particles with matter	6
1.4.1 Interactions of photons with matter	6
1.4.2 Interactions of neutrons with matter	6
1.5 The need for monoenergetic fast neutron beams	7
1.6 Neutron sources	8
1.6.1 Polychromatic beams and energy selective methods	8
1.6.1.1 Fission reactors	8
1.6.1.2 Spallation sources	9
1.6.1.3 Photo-neutron sources	9
1.6.1.4 Radioisotope sources	10
1.6.1.5 How to select the energy from a polychromatic spectrum	10
1.6.2 Naturally monoenergetic sources: light ions and particle accelerators	11
1.7 The PSI compact DD neutron generator	12
1.7.1 Working principle of the generator	12
1.7.2 Kinetics of the DD fusion reaction	13
1.8 Detecting fast neutrons	15
1.8.1 Available reactions for fast neutron detection	15
1.8.2 Plastic scintillator: nature and coupling to electronics	17
1.8.3 From individual detectors to computed tomography	18
1.9 Summary	19

2	Model of the source and calibration measurements	23
2.1	Simulation of the real neutron spectrum of the source	23
2.1.1	Geometrical energy spread	23
2.1.2	Inherent energy spread	26
2.1.2.1	Physics of a solid target	26
2.1.2.2	Deuterium implantation	27
2.1.2.3	Deflection of the deuteron before fusion	31
2.1.2.4	Further assumptions on the fusion physics models	31
2.2	Experimental characterization of the PSI generator neutron spectrum	33
2.3	Proof of principle with selected samples	35
2.3.1	Measurement apparatus	35
2.3.2	Measurement method	37
2.3.3	Exposure time	39
2.3.4	Alignment of the setup	40
2.3.5	Results and discussion with selected samples	41
2.3.6	Limitations of reference cross-section data	43
2.4	Calibration with reference samples	46
2.4.1	Objectives of the calibration	46
2.4.2	Identifying the elements of interest	46
2.4.3	Sample preparation	46
2.5	Results and discussion of the calibration	49
2.5.1	Macroscopic cross-section	49
2.5.2	Microscopic cross-section	58
2.5.3	On the measurement reproducibility	64
2.6	Summary	64
3	From a one-pixel approach to full computed tomography	67
3.1	The fast neutron CT setup	67
3.2	CT measurement method	69
3.3	CT reconstruction steps	70
3.3.1	CT data normalization	70
3.3.2	CT reconstruction algorithm	72
3.4	CT results and discussion	74
3.4.1	Sample Set 1 - Images	74
3.4.2	Sample Set 1 - Material decomposition	76
3.4.3	Sample Set 2 - Images	76
3.4.4	Sample Set 2 - Material decomposition	78
3.5	CT with a photon source	78
3.6	Summary	80
4	Conclusion and outlook	83
4.1	Conceptual study of alternative sources	83
4.1.1	Increasing the deuteron acceleration	83
4.1.2	Reducing the neutron spread	84
4.1.3	Reducing the measurement time	86
4.2	Conclusion	87
	Bibliography	91
A	Updated polynomial fit of the thin target neutron spectra	97

B	Scattering and nuclear reaction	99
B.1	Physics of neutron elastic scattering	99
B.1.1	Projectile - scattered particle relation	100
B.1.2	Projectile - recoiling particle relation	101
B.2	Physics of nuclear reaction	102
C	Error propagation	105
D	Impurities in a reference sample	107
E	Sinograms of the CT data	109
E.1	Sinograms of Sample Set 1	109
E.2	Sinograms of Sample Set 2	110
E.3	Sinograms with the Co-60 source	110
	Curriculum vitae	111

List of abbreviations

0D	Zero-dimensional
2D	Two-dimensional
3D	Three-dimensional
8P8C	8 position 8 contact
alpha, α	He ₂ ⁴ nucleus
CAD	Computer-aided design
CT	Computed Tomography
DD	Deuterium-Deuterium
DT	Deuterium-Tritium
ENDF	Evaluated nuclear data file
ETHZ	Eidgenössische Technische Hochschule Zürich
ESF	Edge Spread Function
FBP	Filtered back projection
FWHM	Full width at half maximum
gamma	Energetic electromagnetic wave
LA	Large aluminium container
MCNP6	Monte Carlo N-Particle Transport Code version 6
NG	Neutron Generator
PMT	Photomultiplier
PSI	Paul Scherrer Institut
RC	Resistor-capacitor
RDX	Research Department Explosive
RF	Radio frequency
ROI	Region of interest
SART	Simultaneous algebraic reconstruction technique
SI	International System of Units
SiPM	Silicon photomultiplier
SMAPE	Symmetric mean absolute percentage error
SS	Stainless steel container
USB	Universal Serial Bus

List of symbols

E_i	Energy of the particle i	[MeV]
I_{BC}	Beam intensity behind blinding cone	[particles \cdot s $^{-1}$]
I_{emp}	Beam intensity without sample	[particles \cdot s $^{-1}$]
I_τ	Beam intensity behind sample	[particles \cdot s $^{-1}$]
M	Molar mass	[g \cdot mol $^{-1}$]
m_i	Mass of the particle i	[kg]
N_i	Atomic concentration of element i	[atoms \cdot cm $^{-3}$]
N_A	Avogadro's number	[mol $^{-1}$]
P	Number of CT projections	[-]
$\Phi(E)$	Neutron spectrum	[neutrons \cdot cm $^{-2} \cdot$ s $^{-1} \cdot$ MeV $^{-1}$]
Q_{DD}	Q-value of the DD reaction	[MeV]
R	Number of CT rays	[-]
ρ	Density	[g \cdot cm $^{-3}$]
Σ_t	Total macroscopic cross-section	[cm $^{-1}$]
τ	Sample thickness	[cm]
Θ_i	azimuthal angle of the particle i	[rad]
θ_i	Emission angle of the particle i in the basis plane	[rad]
v_i	Velocity of the particle i	[m \cdot s $^{-1}$]
Y	Yield	[neutrons \cdot cm $^{-2} \cdot$ s $^{-1}$]
Z	Atomic number	[-]
ζ	Macroscopic cross-section correction	[cm $^{-1}$]

List of Figures

1.1	Scheme of a typical 0D attenuation measurement setup.	4
1.2	Macroscopic cross-section of pure iron, water, and polyethylene for photons and neutrons over energy ranges of interest, including commonly available radioisotopes. The attenuation is directly linked to the macroscopic cross-section, as described in Section 1.3.	7
1.3	Photograph of the Budapest Research Reactor and its measurement hall.	9
1.4	Photograph of the spallation source SINQ at PSI, from [1].	10
1.5	Chronology of the Time-of-Flight measurement with a pulsed polychromatic source. The particle bunch broadens as it flies since the fastest particles (high-energy) get ahead of the slowest ones (low-energy). The X-rays that are sometimes produced during neutron-generating reactions can be used as a start signal; they travel at the speed of light, faster than any neutron.	11
1.6	Total cross-section for the DD and the DT fusion reactions.	12
1.7	The PSI compact fast neutron generator, adapted from [2]. The plasma radiates a bright pink color, combination of photons of different wavelengths, coming from different energy transitions of the hydrogen electron.	13
1.8	Schematic geometrical view of the generator. The 0° neutron emission direction is aligned with the deuteron beam impinging on the titanium target.	14
1.9	Theoretical neutron energy depending on its angle of emission for an incoming deuteron acceleration of 50, 100, 150, and 200 kV.	15
1.10	Differential cross-section of the DD fusion reaction [3] for an incoming deuteron acceleration of 50, 100, 150, and 200 kV. The higher cross-section in forward (0°) and backward (180°) directions imply higher beam intensities, with respect to the 90° position.	16
1.11	Scheme of the computed tomography arrangement. Adapted from [4].	18
1.12	Simulated sinogram and image obtained during a CT reconstruction process. . . .	19
2.1	Schematic views of the geometrical situation around the generator.	24
2.2	Sensitivity study on the neutron energy spread due to the dimensions of the detector.	25
2.3	Schematic illustrating the different depths at which fusion events happen. Since the deuterons lose energy while progressing in the target, they undergo fusion at various energies and the resulting neutrons also have a different energy.	26
2.4	The “uniform” and “round-peak” deuterium distributions and their effect on the neutron yield.	29
2.5	Resulting full width at half maximum for the two “thick-target” neutron spectra models for a 80 keV deuteron beam.	29
2.6	Simulated energy spectra at different emission angles, for an incoming deuteron beam of 80 keV and different models of deuterium implantation in the target. . . .	30
2.7	Effect of a realistic deuteron impact vector on the final neutron spectrum.	32
2.8	Equivalence between the spectrum-averaged neutron energy and the neutron emission direction.	33

2.9	Comparison of the experimental neutron spectra obtained with the Helium-3 spectrometer and the result of the convolution of the simulated spectra with the impulse response of the detector.	35
2.10	CAD model of the measurement setup.	36
2.11	Photograph of the measurement setup.	37
2.12	Information routing overview of the measurement setup.	38
2.13	Simplified CAD model of the first manual centering of the track with respect to the vacuum chamber. The golden piece is the adapter of the lasers to the vacuum chamber, which is the cylinder is the center. The dashed lines represent the laser light paths. The white flat pieces are light stops.	40
2.14	Fine alignment method of the track with respect to the neutron generator.	41
2.15	Macroscopic cross-section of alumina, magnesia, and deionized liquid water for a deuteron beam of 80 keV, compared to models without and with realistic deuteron angle distribution.	42
2.16	SMAPE comparison of the experimental macroscopic cross-section and five different physical models.	43
2.17	Comparison of datasets for the microscopic cross-section of natural carbon. The scatter plots correspond to the experimental sets, while the continuous plot is an evaluated one [5].	44
2.18	Comparison of datasets for the microscopic cross-section of Arsenic-75. The scatter plots correspond to the experimental sets, while the continuous plot is an evaluated one [5].	45
2.19	Photograph of the sealed stainless steel container used during the calibration. . . .	47
2.20	Theoretical spectrum-averaged macroscopic cross-sections of all the samples studied, according to the “uniform” model, coupled to a realistic deuteron impact vector. . .	49
2.21	Macroscopic cross-section of Al, Al ₂ O ₃ , AlN, BeO, C, and C ₂ F ₄ . Deuteron beam of 80 keV.	51
2.22	Macroscopic cross-section of C ₂ H ₄ , H ₂ O, As, B, BN, and C ₆ Br ₆ . Deuteron beam of 80 keV.	52
2.23	Macroscopic cross-section of Ca, CCl ₄ , LiCl, Mg, MgO, and NaCl. Deuteron beam of 80 keV.	53
2.24	Macroscopic cross-section of P, S, Si, and Steel 316L. Deuteron beam of 80 keV. . .	54
2.25	Two Aluminum Nitride - AlN samples with different qualities. Deuteron beam of 80 keV.	54
2.26	SMAPE at given trolley positions, across all available samples.	55
2.27	Computer model of the measurement setup around the generator. Several emission angles are shown to highlight the growing proximity of the strong RF source beyond 90°.	55
2.28	SMAPE of the reference models, across samples and trolley positions. The first group “All samples” takes into account all twenty-two available samples. The group “Three samples” refer to the three samples (water, magnesia, and alumina) used for the proof of principle in Section 2.3.	57
2.29	Microscopic cross-sections of all the nuclides of interest studied, according to the “uniform” model, coupled to a realistic deuteron impact vector. Steel 316L is treated here as a pseudo-element because the material itself is of interest, as a commonly used structural material.	58
2.30	Microscopic cross-section of Al, As, O, B, and Br. Deuteron beam of 80 keV. . . .	59
2.31	Microscopic cross-section of Be, Ca, Cl, F, and H. Deuteron beam of 80 keV. . . .	60
2.32	Microscopic cross-section of Li, Mg, N, Na, and steel 316L. Deuteron beam of 80 keV. .	61
2.33	Microscopic cross-section of Si, S, P, and C. Deuteron beam of 80 keV.	62
2.34	Repeated measurement of the alumina macroscopic cross-section. The model corresponds to the “uniform” deuterium implantation, coupled to a realistic deuteron impact vector.	64

3.1	Information routing overview of the CT measurement setup.	68
3.2	CAD model of the CT measurement setup.	68
3.3	Photograph of the CT measurement setup.	69
3.4	The two sample sets used for CT imaging. The dimensions are given in millimeters.	70
3.5	Macroscopic cross-sections structures in the samples of interest, according to the model featuring an “uniform” deuterium distribution, and a realistic deuteron impact vector distribution.	71
3.6	Structure of the CT sinogram. A line, highlighted in yellow, corresponds to a given detector across all the Ct projections. A column, in green, represents a given CT projection across all the detectors.	72
3.7	Effect of the centering correction on the CT projection at 0 and 180°. The logarithm of the attenuation is plotted, according to Equation 3.2.	73
3.8	Sensitivity study on the scattering component factor. The least squares study was computed over all the available trolley positions.	73
3.9	Reconstruction of the CT of Sample Set 1 at 0, 40, 60, 90 and 115° with the FBP reconstruction algorithm.	75
3.10	Comparison for Sample Set 1 of the ROIs median grayscale value and the macroscopic cross-section from the calibration of Section 2.5.1.	75
3.11	Atomic concentrations of carbon, hydrogen, and oxygen for the three regions of interest of Sample Set 1, according to the theory and from the solution of the material decomposition linear systems.	76
3.12	Reconstruction of the CT of Sample Set 2 at 0, 40, 60, 90 and 115° with the FBP reconstruction algorithm.	77
3.13	Comparison for Sample Set 2 of the ROIs median grayscale value and the macroscopic cross-section from the calibration of Section 2.5.1.	77
3.14	Atomic concentrations of carbon, hydrogen, and oxygen for the three regions of interest of Sample Set 2, according to the theory and from the solution of the material decomposition linear systems.	78
3.15	Photograph of the CT measurement setup, adapted to the measurement with the Co-60 source.	79
3.16	Reconstruction of the CT of Sample Set 1 and 2 around a Co-60 source, with the FBP reconstruction algorithm.	79
4.1	Evolution of the spectrum-averaged microscopic cross-section of hydrogen, carbon, nitrogen, and oxygen, depending on the initial deuteron energy.	85
4.2	Macroscopic cross-section variations for selected samples in the forward direction (0°) when the deuteron acceleration is modified.	86
A.1	Comparison of the neutron spectrum before and after correction of the Legendre polynomials at 100 and 300 keV.	97
B.1	Scheme of an elastic scattering event. The least opaque disks indicate the position of the particles before impact, and the most opaque ones after impact.	99
B.2	Scheme of a general nuclear reaction. The least opaque disks indicate the position of the particles before reaction, and the most opaque ones after.	102
E.1	Sinograms of Sample Set 1 at 0, 40, 60, 90 and 115°.	109
E.2	Sinograms of Sample Set 2 at 0, 40, 60, 90 and 115°.	110
E.3	Sample Set 2, with the Co-60 source, sinogram.	110

List of Tables

2.1	Location of the corners defining the upper half of the neutron detector in Cartesian coordinates.	25
2.2	Counts registered for a 219 seconds exposure in the case of a 4π -output of about $2.2 \cdot 10^7$ n·s ⁻¹	40
2.3	List of the investigated samples for the calibration.	48
2.4	SMAPE of the macroscopic cross-section data of the investigated samples.	56
2.5	List of the nuclides of interest, with their SMAPE	63
3.1	Centering correction applied to each sinogram.	72
3.2	Sample Set 1 - Median grayscale values (cm ⁻¹).	74
3.3	Sample Set 2 - Median grayscale values.	76
3.4	Contrast obtained with the Co-60 photon source	80
A.1	New Legendre polynomial fit for neutron spectrum with the thin target assumption.	97

Atoms for Peace
Dwight D. Eisenhower

Chapter 1

Introduction

1.1 Imaging with ionizing radiation as a nondestructive testing technique

Nondestructive inspection methods have always been of interest in cases where the integrity of the subject analyzed cannot or should not be compromised. These cases span a variety of domains such as medicine (e.g., bone radiography), industry (e.g., inspection of castings or welds), science (e.g., characterization of materials or live process monitoring), archaeology (e.g., cultural heritage analysis) or homeland security (e.g., detection of hazardous materials). Compared to other techniques, methods utilizing ionizing radiation have received considerable attention [6, 7, 8] due to their unique properties, which will be detailed in the following sections.

Ionizing particles can be divided in two main families: the “charged” particles, such as electrons and all the atoms stripped of or carrying an excess of electrons, and the “uncharged” ones, including photons and neutrons. In the case of charged particles, the Coulomb interactions are so strong that a few centimeters of solid matter are enough to completely absorb almost any typical particle beam [9]. On the other hand, uncharged particles are not subject to the Coulomb forces since they have no electrical charge. They can therefore, depending on the particle and energy, have a significant chance of penetrating relatively thick pieces of material without interaction. Since thick samples are of great interest and the focus of this work, only the uncharged particles will be described in further detail.

1.2 Fundamentals of uncharged particle interactions with matter

This report will focus exclusively on beam transmission analysis, i.e. the study of the progressive attenuation - or intensity loss in terms of quantity of particles - of an ionizing radiation beam going through a given sample. The matter contained in the sample constitutes a barrier for the radiation beam and it is assumed at first that any particle interacting with the sample will be lost and not later detected. By carefully analyzing the way the attenuation behaves, one can extract meaningful information about the sample. In order to explain these proprieties, several fundamental notions shall be presented in this section.

It will start with what is referred to in this work as a 0D approach: the neutron detector is a unique pixel, whose field of view is completely covered by the radiation field, and this radiation field is uniformly attenuated by a homogeneous sample when the latter is present. Figure 1.1 presents an overview of the situation.

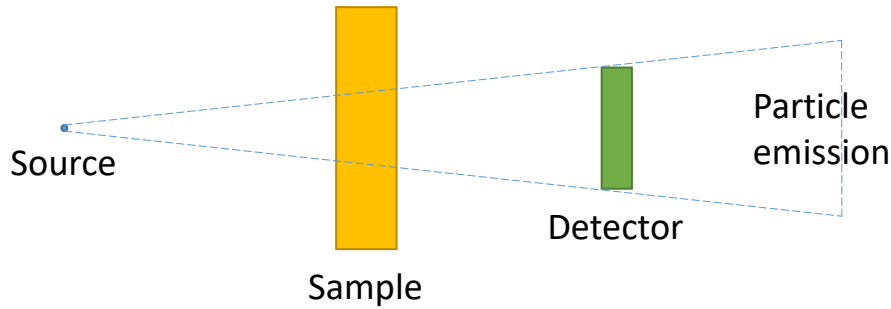


Figure 1.1 – Scheme of a typical 0D attenuation measurement setup.

For an uncharged particle of a given energy passing through a uniform medium, the probability of interaction with matter is constant per unit path length [9]. If the medium is composed of one element, the probability of passing through the material without interacting can be described as $[e^{-\tau \cdot N \cdot \sigma_i}]$, with the thickness of matter τ , the atomic density within the sample N , and the corresponding total microscopic cross-section of that element σ_t , which has the dimension of an area. The square meter is therefore the SI unit of the microscopic cross-section, although in practice the *barn* ($1 \text{ b} = 10^{-28} \text{ m}^2$) is often used. The product of the atomic density and the microscopic cross-section is called the macroscopic cross-section - with a dimension which is the inverse of a length - and is denoted by Σ . Since all the particles that interacted with matter are considered lost, only the total cross-section - which includes all possible kinds of interaction¹ - will be considered for now and the t indicating total will be subsequently omitted. Directly based on the aforementioned probability of non-interaction, the intensity remaining I_τ after a monoatomic sample i of thickness τ is given by Equation 1.1, also called the Beer-Lambert law, in a first approximation in which the attenuation coefficient is considered constant throughout the sample, and the neutron beam collimated and monoenergetic. I_{emp} (as in empty) is the beam intensity when the sample is absent from the field of view of the neutron detectors. Discrete microscopic cross-section data σ_i are available from several international databases [10].

$$I_\tau = I_{\text{emp}} \cdot e^{-\sigma_i \cdot N_i \cdot \tau} \equiv I_{\text{emp}} \cdot e^{-\Sigma_i \cdot \tau} \quad (1.1)$$

1.3 From Beer-Lambert to quantitative elemental analysis

From Equation 1.1, the concentration N_i can be easily computed with Equation 1.2, provided that the intensity of the beam is measured without (I_{emp}) and with (I_τ) the sample obstructing the detector field of view, along with the sample thickness τ , and the microscopic cross-section σ_i , which is available from tables.

$$N_i = \frac{1}{\sigma_i \cdot \tau} \cdot \ln \left(\frac{I_{\text{emp}}}{I_\tau} \right) \quad (1.2)$$

In this very simple case, only two intensity measurements (I_{emp} and I_τ) are necessary to get quantitative elemental information about the sample. With a more realistic sample that does not contain only one element, but instead n different elements, the Beer-Lambert law remains valid for a collimated monoenergetic beam, with the macroscopic cross-section being written as:

$$\Sigma \equiv \sigma_1 \cdot N_1 + \sigma_2 \cdot N_2 + \dots + \sigma_n \cdot N_n \quad (1.3)$$

¹That includes scattering as well. For small-scattering angles, the neutron might in reality still reach the detector. Dedicated correction will be implemented to compensate for this approximation. See Section 2.3.2 for more details.

In that case, the two single measurements, I_{emp} and I_τ are not sufficient to solve the equation of the n unknowns N_i because the system is mathematically under-determined: there are more unknowns than equations, so there is in general an infinite number of possible solutions to the problem. A necessary condition to the existence of a unique solution is to at least have a determined system, i.e. as many linearly independent equations m (resulting from m measurements) as unknowns such as in Equation set 1.4 [11]. The nomenclature becomes then $\sigma_{i,j}$ for the microscopic cross-section of the element i and the measurement number j .

$$\begin{cases} -\frac{1}{\tau} \ln \left(\frac{I_1}{I_{\text{emp},1}} \right) = \sigma_{1,1} \cdot N_1 + \dots + \sigma_{i,1} \cdot N_i + \dots + \sigma_{n,1} \cdot N_n \\ \dots \\ -\frac{1}{\tau} \ln \left(\frac{I_j}{I_{\text{emp},j}} \right) = \sigma_{1,j} \cdot N_1 + \dots + \sigma_{i,j} \cdot N_i + \dots + \sigma_{n,j} \cdot N_n \\ \dots \\ -\frac{1}{\tau} \ln \left(\frac{I_m}{I_{\text{emp},m}} \right) = \sigma_{1,m} \cdot N_1 + \dots + \sigma_{i,m} \cdot N_i + \dots + \sigma_{n,m} \cdot N_n \end{cases} \quad (1.4)$$

The measured macroscopic cross-section in the case j is $\Sigma_{\text{meas},j} = -\frac{1}{\tau} \ln \left(\frac{I_j}{I_{\text{emp},j}} \right)$. The Equation set 1.4 can be re-written under the compact matrix form of Equation 1.5.

$$\overline{\Sigma_{\text{meas}}} = \overline{\sigma} \overline{N} \quad (1.5)$$

A linear system of equations such as Equation 1.5 can be approached with classical solving methods. Provided that \overline{N} is the unknown, it can be solved analytically given some assumptions: the macroscopic cross-section data and the coefficients of matrix $\overline{\sigma}$ are always strictly positive; also, the determinant of the same matrix is non-zero since the energies at which the measurements were performed were selected with caution so that each measurement is not a linear combination of the others. Hence the square matrix $\overline{\sigma}^T \overline{\sigma}$ is also invertible. If it is multiplied with $\overline{\sigma}^T$ on each side, Equation 1.5 becomes Equation 1.6.

$$\overline{\sigma}^T \overline{\Sigma_{\text{meas}}} = \overline{\sigma}^T \overline{\sigma} \overline{N} \quad (1.6)$$

If it is then multiplied with $\left(\overline{\sigma}^T \overline{\sigma} \right)^{-1}$ on each side, Equation 1.6 becomes Equation 1.7.

$$\left(\overline{\sigma}^T \overline{\sigma} \right)^{-1} \overline{\sigma}^T \overline{\Sigma_{\text{meas}}} = \left(\overline{\sigma}^T \overline{\sigma} \right)^{-1} \overline{\sigma}^T \overline{\sigma} \overline{N} \quad (1.7)$$

Since the product of a matrix with its inverse is the identity matrix, Equation 1.7 can finally be simplified. The analytical least-squares solution for the vector of elemental concentrations \overline{N} is then given by Equation 1.8.

$$\overline{N} = \left(\overline{\sigma}^T \overline{\sigma} \right)^{-1} \overline{\sigma}^T \overline{\Sigma_{\text{meas}}} \quad (1.8)$$

The problem could very well be approached the other way around. Instead of an unknown object, it is possible to use a well-characterized mono-atomic sample with a known atomic concentration. The vector \overline{N} is now an input variable along with $\overline{\Sigma_{\text{meas}}}$, while the unknown is the matrix $\overline{\sigma}$. Since there is only one kind of nuclide within the sample, the problem is simplified. The vector \overline{N} is reduced to a scalar. The matrix $\overline{\sigma}$ can be reduced to a vector containing the cross-section of the nuclide at different energies. This case could be very useful if the cross-section data prove to be unreliable or non-existent, as will be shown in later sections.

The previous paragraphs assumed that m linearly independent equations could easily be found. One way to obtain those is to find a parameter which, when tuned from one measurement to the other, would make the coefficients $\sigma_{i,j}$ in front of the unknowns N_i vary in a non-linear and element-specific fashion. In the frame of this work, the **energy of the ionizing radiation beam** will be this varying parameter. The rationale behind this choice is rooted in the interaction properties of uncharged particles with matter. The following sections describe these properties and demonstrate that fast neutrons are the best fit among uncharged particles for this application.

1.4 Interactions of uncharged particles with matter

1.4.1 Interactions of photons with matter

Photons in the energy range of interest interact with matter through three main channels: the photoelectric effect, Compton scattering, and pair production. While undergoing a photoelectric event, the incoming light quanta is completely absorbed and a photo-electron is ejected from the target atom shell, carrying the photon energy minus the binding energy of the electron. During a Compton scattering event, only part of the photon energy is transmitted to one of the atom electrons: the photon is not completely absorbed and both particles leave the event location. When a pair production happens, the photon disappears to create an electron-positron pair. The relative likelihood of each of these events is energy-dependent [9].

Overall, the photon beam attenuation strongly depends on, among other things, the atomic number (Z) of the target materials, as depicted on Figure 1.2. The contrast is poor between materials with a small change in Z and comparable densities, such as water and polyethylene. Additionally, the radiation is strongly absorbed by high- Z materials, like iron. Imaging mixed- Z samples therefore proves to be difficult, as the attenuation will be dominated by the high- Z regions and the low- Z will be less detectable. The attenuation coefficients of photons also generally varies smoothly with the energy of the particle for all nuclides in an almost identical fashion over a wide range of energies², which means that making a measurement at different energies will not give additional information: all the attenuation coefficients will be multiplied by the same constant, the equations will remain linearly dependent and a system of equations such as Equation set 1.4 stays under-determined.

1.4.2 Interactions of neutrons with matter

Neutrons interact with matter in a different way [12], directly with the nucleus of the target. There are two main channels of interaction which are of interest. First, there is the scattering event during which the direction of the neutron changes and the target nucleus receives kinetic energy but does not gain or lose nucleons. If the kinetic energy of the neutron is conserved in the center of mass frame, it is called elastic scattering. If some kinetic energy is lost and emitted in the form of a secondary particle, like a gamma, it is an inelastic scattering event. Beyond scattering, there are all the absorption reactions during which the target nucleus is modified by the absorption of the incoming neutron and might lead to the creation of new subsequent reaction products. This type of reactions encompasses, for example, fission, radiative capture, and many others. The physics and energy transfer of both scattering and general nuclear reactions for many nuclei are described in detail in Appendix B of this thesis.

In the frame of this work, it is relevant to further separate neutrons into two families: thermal neutrons (with an energy typically around 0.025 eV) and fast neutrons (roughly above 1 MeV). Thermal neutrons are quite readily available at high fluxes from the many research fission reactors or the relatively few spallation sources existing worldwide. Since their energy is small and the corresponding cross-section typically relatively high, thermal neutrons are not able to penetrate

²This is not true at low photon energies, below few tens of keV. However, with such low energies, the photon beam has a very limited probing range, and is not useful for thick sample probing.

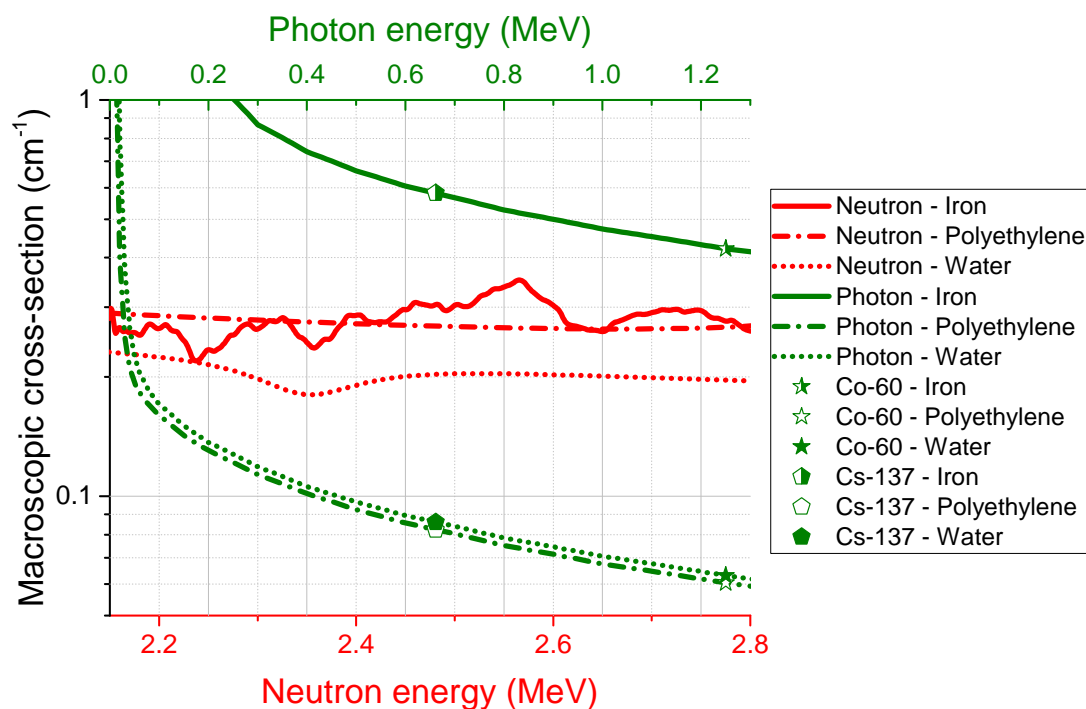


Figure 1.2 – Macroscopic cross-section of pure iron, water, and polyethylene for photons and neutrons over energy ranges of interest, including commonly available radioisotopes. The attenuation is directly linked to the macroscopic cross-section, as described in Section 1.3.

very thick objects (e.g., several to tens of cm). On the other hand, fast neutrons have a higher initial energy and generally most nuclides have a relatively low interaction cross-section in that energy range; hence thick objects can be imaged.

Unlike photons, fast neutrons do not show a particularly strong attenuation for high-Z materials, and materials with nearly identical Z-values can have very different attenuation behavior, as shown in Figure 1.2. Even isotopes of the same element can exhibit noticeable differences. Hence, fast neutrons can give an excellent contrast for mixed-Z samples. On the same figure, it is clear that the attenuation coefficients also vary strongly with the particle energy in a unique and non-linear fashion for each sample, which means that measurements at different energies will finally give the sought-after independent equations forming a fully determined equation system. The rest of this study is consequently focused solely on the application of **fast neutrons to element-sensitive analysis and imaging techniques**.

1.5 The need for monoenergetic fast neutron beams

From the previous sections, it has been demonstrated that fast neutrons are the most suitable particles to obtain a quantitative elemental analysis of a thick sample. However, all the previous investigation work assumed that a monoenergetic beam of fast neutron was readily available.

If the neutron beam used for the measurements is not monoenergetic, then the tabulated microscopic cross-section data cannot be directly used in the system of Equations 1.4. Instead, the

averaged microscopic cross-section $\bar{\sigma}_i$ should be used and can be computed through Equation 1.9.

$$\bar{\sigma}_i = \frac{\int_{E_{\min}}^{E_{\max}} \Phi(E) \cdot \sigma_i(E) dE}{\int_{E_{\min}}^{E_{\max}} \Phi(E) dE} \quad (1.9)$$

With $\Phi(E)$ the neutron spectrum, i.e. its energy distribution, E_{\min} and E_{\max} its upper and lower energy boundaries, and σ_i the tabulated microscopic cross-section.

An accurate knowledge of the incoming neutron spectrum is thus needed. This integral calculation also shows that neutron beams containing a wide range of neutron energies are detrimental to the problem solution. Indeed, the averaging process tends to smooth and blend all the microscopic cross-section structures that usually make each nuclide signature unique. It becomes then difficult to obtain enough linearly independent images of the sample and the linear system might remain under-defined.

For these reasons, it is critical to obtain as **monoenergetic as reasonably achievable neutron spectra**. The next section will describe in detail the different solutions available and the reasons behind the selection of a particular kind of source in the frame of this study.

1.6 Neutron sources

Free neutrons are unstable particles and their population follows an exponential decay law with a half life of about ten minutes [13]; they are therefore difficult to store. Since they do not carry any charge, they cannot be directly accelerated by conventional electromagnetic fields to reach a certain energy like it is done with charged particles in the many different types of particle accelerators. This section will present the main alternatives that were found to produce energetic neutrons. These sources produce either directly monoenergetic neutrons or a polychromatic beam, the latter in some cases can be monochromatized by certain techniques.

1.6.1 Polychromatic beams and energy selective methods

1.6.1.1 Fission reactors

A robust first neutron source to consider is based on nuclear fission reactors. Research reactors use nuclear fission, like the fleet of fission reactors aimed at power production developed since the 1940s, but are designed and optimized for other applications. They operate most often in the Watt to tens of Megawatt range of power. During a typical fission event, a neutron is absorbed by a heavy nucleus such as Uranium-235 forming an excited Uranium-236 nucleus. This unstable nucleus will subsequently split into some combination of particles including fission fragments, free neutrons, and prompt gammas. All these reaction products carry roughly 200 MeV of kinetic energy; each neutron energy is usually in the MeV range. Some of the neutrons produced can be used to maintain the chain reaction in the reactor and to keep it running; another portion can be used for other purposes, such as imaging.

To get the nuclear reactor to criticality with an economically reasonable fuel enrichment, moderating material - such as light water - is used within the reactor to slow down the neutrons to the thermal range (around 0.025 eV) through scattering. The probability of fission dramatically increases in that region, meaning the chain reaction is then much easier to maintain. The fission neutron spectrum is naturally broad but moderation enhances this spread by shifting the spectrum even more towards thermal energies. When needed, the moderator can also serve as a coolant to evacuate excess thermal energy produced by the chain reaction. So-called fast research reactors, which operate without moderator, also exist but represent only a very small portion of the overall



Figure 1.3 – Photograph of the Budapest Research Reactor and its measurement hall.

fleet.

Nuclear reactors are large scale facilities requiring a complicated licensing. Residual heat from all the reaction products means that a reactor cannot typically be turned off without constant cooling. Radioactive reaction products and activated materials are hazardous and massive shielding is needed to protect the outside world from them. Spent fuel storage and decommissioning in general of such installations are still debated topics. Facilities like the Budapest Research Reactor (10 MW), for example - shown in Figure 1.3 - can deliver flux in the range of $2.1 \cdot 10^{14} \text{ n}\cdot\text{s}^{-1}\cdot\text{cm}^{-2}$ [14].

1.6.1.2 Spallation sources

Spallation sources are another way to produce energetic neutrons. They are accelerator based: a proton beam of several hundreds of MeV is generated and shot at a high-Z target such as lead. In two successive processes - the intra-nuclear cascade and the evaporation - neutrons, among others, are released [15]. Per event, the spallation produced many more neutrons than the fission but the resulting spectrum is also rather wide and can extend as high as the initial proton energy.

The spallation process is not a chain reaction like fission reactors, it will stop as soon as the proton beam is interrupted. Decay energy is still generated and the heat produced should be dissipated. Nuclear waste requiring proper disposal is also produced as in a reactor, although in smaller quantities. A coolant is needed - such as heavy water - but it will typically tend to moderate the neutron spectrum down to thermal energies. The total spectrum remains broad like in the case of nuclear reactors. This is usually not seen as a major issue because many experiments other than fast neutron analysis require thermal or even colder spectra. Since the neutron energy can be very high, the shielding requirements around the target are massive. SINQ is the spallation source of the Paul Scherrer Institut (PSI) [16], shown in Figure 1.4 and operating with a 590 MeV proton beam of an intensity up to 2.3 mA coming from the cyclotron HIPA and working in a continuous mode. It delivers a neutron flux of about $1.5 \cdot 10^{14} \text{ n}\cdot\text{s}^{-1}\cdot\text{cm}^{-2}$ in thermal flux close to the target.

1.6.1.3 Photo-neutron sources

Another neutron production method consists of first accelerating electrons to very high energies, up to several hundreds of MeV. At these energies, an intense Bremsstrahlung radiation is produced when the electrons are deflected by a high-Z target such as uranium or lead. The photons produced

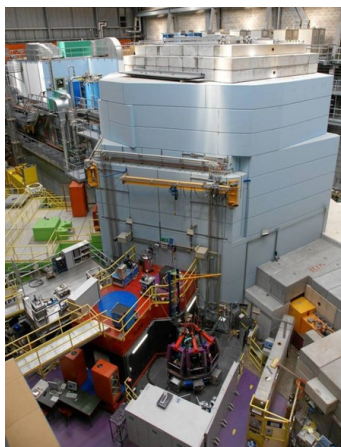


Figure 1.4 – Photograph of the spallation source SINQ at PSI, from [1].

at this occasion are so energetic that they can undergo a photo-nuclear reaction with the target: the target atom is raised to an excited state and decays immediately by releasing a particle such as a neutron. If the target contains fissile material, such as Uranium-235, the neutrons produced can also undergo a fission with the target, producing more neutrons with a broad spectrum. The target also needs cooling to dissipate the energy produced and shielding to protect the people working around. The GELINA facility in Geel, Belgium, produces neutrons in such a way, at an average production rate of $3.4 \cdot 10^{13} \text{ n}\cdot\text{s}^{-1}$ [17].

1.6.1.4 Radioisotope sources

A much more compact way of generating wide spectrum neutron beams is to use radioisotope sources which are based on the natural decay of a radionuclide. The first sub-category is based on (α, n) reactions, where an alpha emitter, e.g. Americium-241, is closely mixed with a selected nuclide, such as Beryllium-9; the reaction obtained is then: $He_2^4 + B_4^9 \rightarrow n_0^1 + C_6^{12}$. In the second sub-category, the radionuclide is unstable enough to spontaneously undergo fission, like Californium-252 (Cf-252). The spectrum of spontaneous fission is close to the one of thermal fission. The (α, n) type shows more structures due to the physics of the reaction, but is still spread over several MeV.

These sources are by themselves of a mm to cm in size only, but should be handled with care as they can never be turned off. They also tend to age and lose their potency as they decay, such as Cf-252 which has a half-life of only about 2.6 years. They are in general orders of magnitude weaker than the reactor- or accelerator-based sources.

1.6.1.5 How to select the energy from a polychromatic spectrum

If the neutron beam contains initially a wide spectrum neutron energies, it is sometimes feasible and useful to filter it to get as close as possible to a monoenergetic beam. It should be noted that the stricter the filtering is done, the more beam intensity is lost. A low brightness means longer image acquisition times to get acceptable statistics and therefore accurate results. A balance between those two parameters should be found.

In the case of thermal neutrons, it is possible to use advanced techniques such as Bragg scattering in a double-crystal monochromator setup [8], since the neutron wavelength is similar to the crystal lattice spacing. A neutron of a given wavelength - i.e. of a given energy - will be scattered in a specific direction. Setting up the sample and the detector aligned with this direction will allow a measurement at said neutron energy. There is no direct equivalent in the fast neutron range

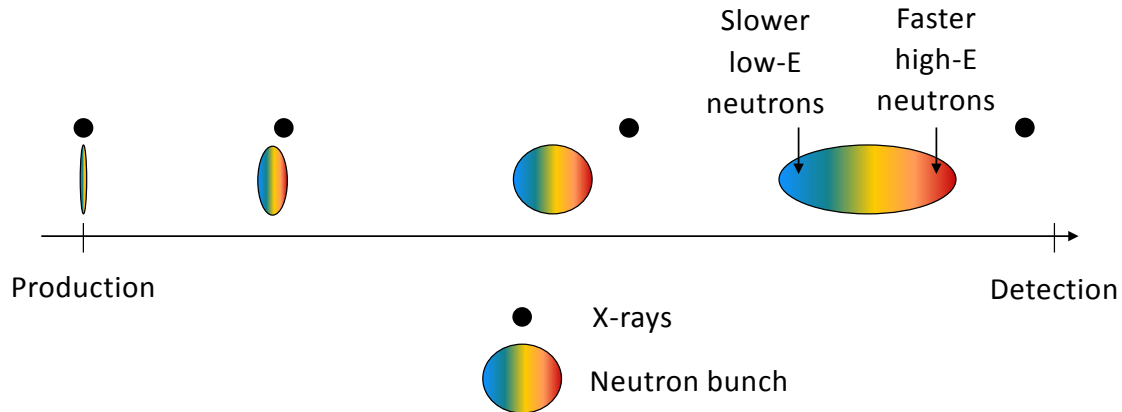


Figure 1.5 – Chronology of the Time-of-Flight measurement with a pulsed polychromatic source. The particle bunch broadens as it flies since the fastest particles (high-energy) get ahead of the slowest ones (low-energy). The X-rays that are sometimes produced during neutron-generating reactions can be used as a start signal; they travel at the speed of light, faster than any neutron.

because the wavelength does not match the lattice spacing any more.

Neutron energies can however be very accurately selected by Time-of-Flight (ToF) techniques, which only work with pulsed sources and precisely timed detector readout. After a neutron bunch is emitted, it flies through long straight flight tubes until it reaches a detector. Since the neutrons within the bunch have different energies while flying, the fastest component will progressively get ahead of the slowest one, as illustrated on Figure 1.5. With tubes of tens of meters and nanosecond-capable electronics, the time difference between both can be measured and the detectors can be calibrated so there are sensitive to only a certain time window, i.e. only a certain portion of the energy spectrum [18].

1.6.2 Naturally monoenergetic sources: light ions and particle accelerators

Several energetic light ions bombarding selected nuclides can also give birth to neutrons [19], but with a spectrum which is naturally monoenergetic or quasi-monoenergetic³. Because of their suitable properties, four reactions emerged among others:

- $H_1^2 + H_1^2 \rightarrow n_0^1 + He_2^3$, or deuterium-deuterium fusion (DD), with a Q-value of 3.27 MeV.
- $H_1^3 + H_1^2 \rightarrow n_0^1 + He_2^4$, or deuterium-tritium fusion (DT), with a Q-value of 17.6 MeV.
- $H_1^3 + H_1^1 \rightarrow n_0^1 + He_2^3$, an endothermic transfer reaction, with a Q-value of -0.734 MeV.
- $Li_3^7 + H_1^1 \rightarrow n_0^1 + Be_4^7$, another endothermic transfer reaction, with a Q-value of -1.64 MeV.

Both endothermic transfer reactions have an energy threshold of 1 and 1.9 MeV, respectively. Such acceleration requirements mean that the machines using these reactions can be only semi-compact. They are not suitable for applications oriented towards portability. On the other hand, both fusion reactions have rather low incoming particle energy requirements, in the hundreds of keV range, as shown in Figure 1.6. Thus, the needs for the input particle accelerator are much reduced with respect to large-scale facilities. However, this comes at the cost of lower total neutron output.

³Upon comparison of the original data from [3], an error was detected in the polynomial fit of the differential fusion cross-section in [19]. A correction is proposed in Appendix A.

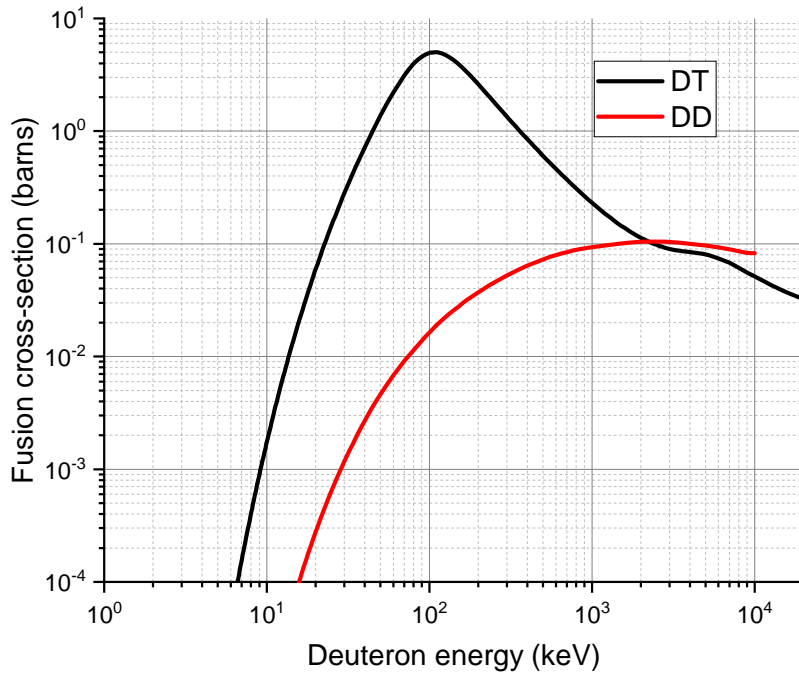


Figure 1.6 – Total cross-section for the DD and the DT fusion reactions.

Total neutron production rates are typically up to the order of $10^{10} \text{ n} \cdot \text{s}^{-1}$ for DD and $10^{12} \text{ n} \cdot \text{s}^{-1}$ for DT - i.e., integrated over the whole 4π range of solid angle. In comparison, as previously mentioned, at a large scale facility such as SINQ [16] the polychromatic flux close to the target is of the order of $10^{14} \text{ n} \cdot \text{s}^{-1} \cdot \text{cm}^{-2}$. Yet, the production of radioactive waste by activation or as reaction products is negligible and no decay heat needs to be removed. The devices are usually tabletop-sized, only proper shielding is needed around the experimental area to protect individuals from the produced fast neutrons. This is an intermediate solution between large scale facilities and small radioisotope sources in terms of cost, size, and yield. For that reason, it was adopted for this study. The DD reaction was preferred over DT. Its main advantage is practical: it does not require the use of radioactive tritium, unlike DT. The licensing and handling of such a source is hence dramatically simplified. Its main drawback is its cross-section, which can be up to more than two orders of magnitude smaller than the one of the DT reaction, as shown in Figure 1.6. The next section details the characteristics of the **DD-based neutron generator built at PSI** for investigation purposes.

1.7 The PSI compact DD neutron generator

1.7.1 Working principle of the generator

The DD neutron generator used in this study is based on a design developed in the frame of a previous doctoral work [4]. An overall view of the generator is given in Figure 1.7.

Everything starts with the introduction of gaseous deuterium in a plasma chamber. The gas is brought to a plasma state by ionization through a radio frequency (RF) power source. Positive deuterium ions are then extracted from the plasma and accelerated towards a titanium target rod by a strong negative electrical potential field of typically up to -100 kV. The target is kept in a vacuum chamber to avoid electrostatic discharges that would likely happen at such high electric

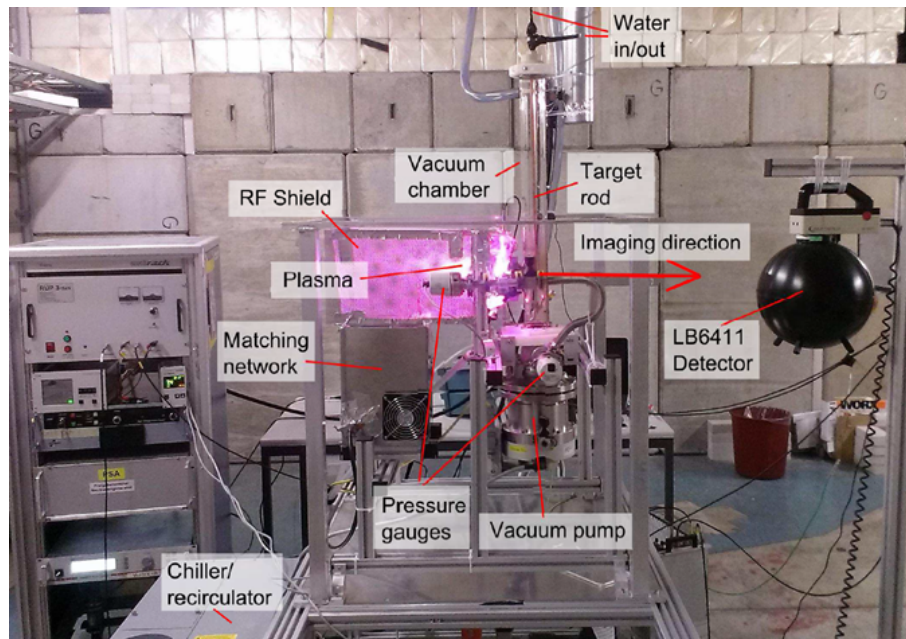


Figure 1.7 – The PSI compact fast neutron generator, adapted from [2]. The plasma radiates a bright pink color, combination of photons of different wavelengths, coming from different energy transitions of the hydrogen electron.

field strengths in air when they are maintained over short distances. The vacuum is maintained by a turbomolecular pump coupled to a pre-vacuum oil pump. The target is a *drive-in* one, i.e. the beam is simultaneously loading the target with deuterium - forming a metal hydride - and bringing new deuterium particles that will have a chance to undergo fusion with the deuterium already implanted. About half of the time, the DD fusion will produce a Helium-3 particle and a neutron. Both particles are emitted in almost opposite directions after the event. There is also a nearly fifty percent chance that a competing reaction happens, producing a tritium nucleus and a proton. As heavy charged particles, these reactions products will undergo strong Coulomb interactions with the structural materials and have almost no chance to ever leave the vacuum chamber and reach outside detectors. They will therefore not be further considered in this report.

Since deuterium tends to outgas from the titanium target at high temperatures [20], a decreasing implanted deuterium concentration fatally means a decreasing fusion rate and neutron production. An advanced cooling of the target is therefore needed and was installed in a parallel project [21]. In essence, instead of a pure titanium target, a thick copper backing was used since the thermal conductivity of this metal is much higher than that of titanium. Only a thin layer of titanium was deposited on top for the hydride formation. The diameter of the target was increased and the whole assembly was rotating during operation in order to increase the surface on which the beam heat is deposited and thus reduce the maximum local temperature. Internal forced air or water cooling was used to further improve the heat dissipation. Overall, the neutron output was measured to be of the order of $10^7 \text{ n}\cdot\text{s}^{-1}$ [21].

1.7.2 Kinetics of the DD fusion reaction

As presented in Section 1.5, knowing the exact neutron spectrum of the source is critical. This section is devoted to the description of the phenomena affecting it.

For the sake of simplicity, the description of the kinetics of this section will be done in the basis plane, orthogonal to the (vertical) direction defined by the titanium target rod and intersecting it

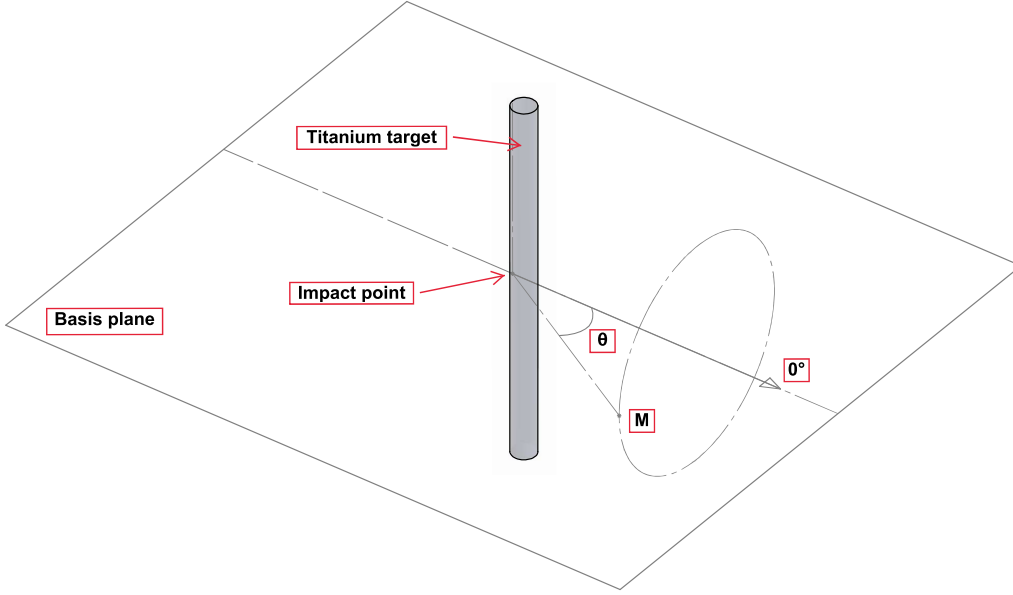


Figure 1.8 – Schematic geometrical view of the generator. The 0° neutron emission direction is aligned with the deuteron beam impinging on the titanium target.

at the impact point of the deuteron beam. The situation is described in Figure 1.8. In this figure, the vertical cylinder is the target rod. The dashed line is the incoming deuteron direction, from left to right. M is the current position of the detector and the dashed line leading to it is the flight path of the neutron from emission to detection, with a given azimuthal angle Θ which is described by the dashed circle.

Because energy and momentum are conserved during this event, the share of energy of the outgoing particles depends on the direction of observation, as illustrated in Figure 1.9. The complete demonstration of the neutron energy dependencies is given in Appendix B.2 and its formulation is reproduced here in Equation 1.10, where E_n is the outgoing neutron energy, E_d the incoming deuteron energy, m_d the deuteron mass, m_H the Helium-m mass, m_n the neutron mass, and θ_n the neutron emission angle with respect to the path direction of the incoming deuteron. θ_n is the equivalent in the basis plane of the 3D azimuthal angle Θ . For a given incoming deuteron energy, all the other variables being constant, only the emission angle impacts the outgoing neutron energy. Thanks to the symmetry of the problem, a two-dimensional study in the basis plane limited to the 0 to 180° angular range is enough to characterize the whole generator.

$$\sqrt{E_n} = \frac{\sqrt{m_d m_n E_d}}{m_n + m_H} \cos(\theta_n) + \frac{\sqrt{m_d m_n E_d \cos^2(\theta_n) + (m_n + m_H)[m_H Q_{DD} + E_d(m_H - m_d)]}}{m_n + m_H} \quad (1.10)$$

The higher the incoming deuteron energy is, the wider the energy spread of the neutron will be. For a 80 keV incoming deuteron energy, the neutron energies will span from about 2.2 MeV to 2.8 MeV, corresponding respectively to the angular boundaries of 180° and 0° . There is consequently no need to further monochromatize the output of the generator, since it offers at each emission angle a **different monoenergetic fast neutron beam**. To use this naturally tuned source, the measurement setup needs only to rotate around the fusion event location, capturing the angles encompassing 0 to 180° . Such a setup is presented in detail in Section 2.3.1.

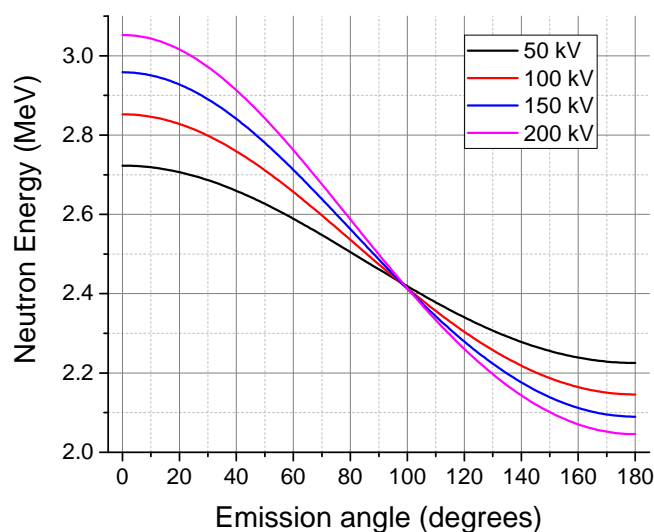


Figure 1.9 – Theoretical neutron energy depending on its angle of emission for an incoming deuteron acceleration of 50, 100, 150, and 200 kV.

As mentioned in Section 1.7.1, the reaction products - neutrons and Helium-3 nuclei - are emitted almost back to back in all the directions of space, although not in an isotropic fashion since the likelihood distribution of the outgoing angle is biased in the forward and backward directions, as illustrated on Figure 1.10.

The above description of the kinetics of the fusion reaction leading to a purely monoenergetic neutron spectrum is valid in an ideal case where all the fusion events happen when the deuterons still has its maximum initial energy - due to the electrostatic acceleration. As it will be detailed in Chapter 2, the spectrum is in reality only quasi-monoenergetic.

1.8 Detecting fast neutrons

A solution for a tunable monoenergetic neutron beam was previously described. The focus will now move to the other end of the experiment, namely the detection of neutrons. Because it is an uncharged particle weakly interacting with matter, it should be first converted into more readily detectable secondary particles. This should be accomplished with reasonable detection efficiency while maintaining a good spatial resolution and/or a small detector size. In the following sections, the most relevant detector options will be presented and the final choice justified.

1.8.1 Available reactions for fast neutron detection

As mentioned in Section 1.4.2, there are two main channels for neutron interaction with matter: **absorption nuclear reactions and scattering events.**

In the case of a nuclear reaction, the neutron could be first moderated in order to enjoy the much larger cross-sections typically available in the thermal range. However, thorough moderation from the MeV range down to the thermal one requires tens of cm of material, even for the most energy-reducing nuclide which is hydrogen. If imaging applications are kept in mind, moderation-based

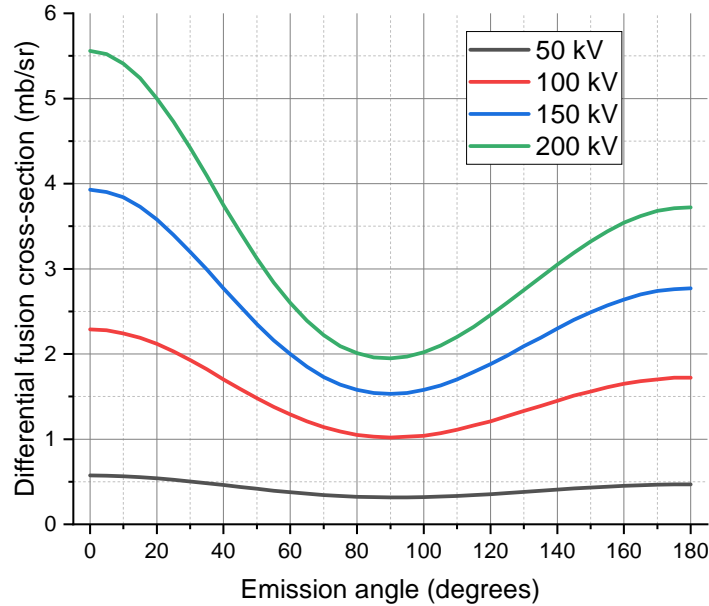


Figure 1.10 – Differential cross-section of the DD fusion reaction [3] for an incoming deuteron acceleration of 50, 100, 150, and 200 kV. The higher cross-section in forward (0°) and backward (180°) directions imply higher beam intensities, with respect to the 90° position.

techniques would not be suitable because the random motion of the slowing down process - due to multiple scattering events - would mean that any origin position needed for imaging information is irretrievably lost. This option will therefore not be investigated further in the frame of this study.

Focusing on nuclear reactions still relevant in the fast range, two nuclides are worth mentioning [9]. First, Lithium-6 with the reaction $Li_3^6 + n_0^1 \rightarrow H_1^3 + He_2^4$. It is burdened by a parasitic reaction dominating above 2.5 MeV, which is detrimental to spectroscopic applications because it creates a continuous distribution of pulses on top of the peaked distribution of the first reaction. It can increase the dead time of the detector and favor pulse pile-up. The capture cross-section is also small in the fast neutron range, compared to scattering. Although it can be partially compensated by the fact that Lithium can be used under solid form, hence with a high density leading to greater efficiency. Large pieces might be needed to get acceptable efficiencies making it difficult to manufacture a high-resolution setup made of small individual pixels. The second nuclide, Helium-3, can undergo $He_2^3 + n_0^1 \rightarrow H_1^1 + H_1^3$. The scattering probability with Helium-3 is however quite strong in that range and creates a continuous distribution of pulses that can overlap with the first peaked distribution, with the same consequences as in the case with Lithium-6. The very high thermal cross-section of the reaction might induce high dead times if a thermal shield is not properly installed around the detector. Helium-3 is usually only available under gaseous form, which means that the detection efficiency is negatively affected. Higher pressures in the detector chamber might partially compensate for this. However bulky pressure-resistant chambers also mean that manufacturing small individual elements for a high-resolution neutron imaging setup is a complex task. On top of that, Helium-3 is a rare and costly isotope⁴. Both main reactions with Lithium-6 and Helium-3 feature a Q-value of respectively 4.78 and 0.764 MeV. A high Q-value means that the discrimination between the reaction products of interest and parasitic particles such as gammas

⁴Fortunately, it was still possible to test an high-resolution He-3 spectrometer in the frame of this work, see Section 2.2 for more details.

is eased: the total energy deposited by the reaction products is equal to the Q-value plus the initial neutron energy, the detection peak is therefore shifted to higher energy ranges, far from the low-energy background.

Beyond absorption nuclear reactions, a neutron can scatter with a nucleus. At high energies, elastic scattering is very much the dominant process for a neutron to interact. For scattering with a light element, the energy transmission to the recoil particle is greater than for a heavy one - as shown in the Appendix B.1 - making the subsequent detection of the recoil easier. Hydrogen is logically the favorite since it is the lightest element and present in large quantities in many standard materials. However, since scattering has a Q-value of zero, the signals are consequently partly mixed with the low-energy background. Another drawback is the partial loss of information about the initial energy of the incoming neutron. Since it scatters with an arbitrary angle, the loss of energy to hydrogen ranges from zero to the initial energy.

Overall, scattering-based technologies offered better opportunities. At PSI extensive work has already been done [4] with **plastic scintillators**, which are based on scattering with hydrogenous scintillating material. Providing good results, the existing practical implementation was adapted for the current work and will be detailed in the next section.

1.8.2 Plastic scintillator: nature and coupling to electronics

The plastic scintillators used in this work are of the type BC400 from the manufacturer Saint-Gobain Crystals [22]. They consist primarily of polyvinyltoluene, a hydrocarbon with a hydrogen to carbon ratio $H/C = 1.103$. Both hydrogen and carbon can be scattered with by an incoming neutron, but the recoiling carbon nuclei receive far less energy on average and also produce far less scintillation light per unit energy, making them essentially negligible [23], and will therefore not be considered further. The recoiling protons which excite the scintillator material are the primary interest of the detector. After excitation, to return to a lower energy state the scintillator material emits light. This light can be then collected by a photosensitive detector and further processed. A higher energy neutron will on average produce higher energy protons, which in turn are likely to excite more the scintillator and therefore produce more light.

BC400 offers good light output (65% of that of Anthracene, a reference in the domain), rather fast response (2.4 ns decay time), is inexpensive, and can be easily manufactured in various shapes and sizes. To insure a good detection efficiency, the scintillator needs to be quite thick due to the long mean free path of fast neutrons within the material. The typical dimensions for this study of an individual detector are 80 mm in depth, 8 mm in height, and 5 mm in width.

To collect the light emitted by the scintillator, a recent generation of compact solid-state photodetectors was used, namely silicon photomultipliers (SiPM) [24]. An SiPM is an array of reverse-biased photodiodes read out in parallel. The diodes are very small: typically hundreds of them can be fit per mm^2 . Each of these diodes, occupying a microcell, are operated in Geiger mode: an interacting photon will trigger a self-sustaining ionization cascade and a small current flow can be measured at its anode. A resistor-based quenching of the signal is used to stop the avalanche and make the diode available again for the next photon detection. Whether one or more photons interact with one of the diodes, the avalanche signal does not allow a quantitative distinction: a unique diode cannot give information about the instantaneous photon flux. However, the high spatial concentration of the array means that a higher burst of incoming photons is more likely to set off more of these individual cells individually. The sum of individual currents coming from the different diodes will then be larger. Overall, this arrangement thus provides a certain proportional information concerning the recoil proton energy. Indeed, a higher neutron energy means higher proton energies on average, which excite the scintillator more and the latter produces then more light. A higher photon flux sets off more photodiodes and a larger electrical pulse can then be recorded. This is useful as the PSI DD neutron generator produces, in addition to neutrons, a significant

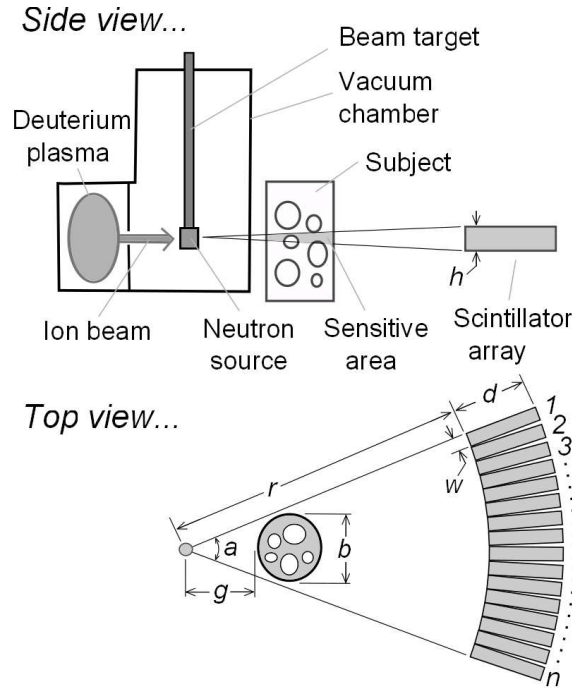


Figure 1.11 – Scheme of the computed tomography arrangement. Adapted from [4].

quantity of parasitic Bremsstrahlung X-rays [25]. To avoid measuring them, it is possible to set a pulse height cut-off. Below a certain threshold - corresponding to the maximum Bremsstrahlung photon energy - the pulse will be discarded as it is considered to be potentially parasitic. It means that some valid neutron pulses will also be lost, but it was deemed acceptable, as it corresponds to a 0.7 MeV threshold for neutrons, or a 25 to 32% loss for neutrons in the 2.2 to 2.8 MeV range [23].

The model ASD-RGB3S-P of SiPM manufactured by AdvanSiD was selected [26]. It has an active area of $3 \times 3 \text{ mm}^2$; two of them were set up behind each scintillator, operating in parallel, coupled with optical grease to the scintillator. Its photo detection efficiency matches relatively well the emission spectrum of the BC400 scintillator. SiPMs are a good alternative to standard photomultiplier tubes (PMTs) as they are very compact in size, low cost, robust, and require much lower operating voltages - around 30 V for this SiPM, compared to the up to several kV range for the standard photomultiplier tubes. Like PMTs, SiPMs also benefit from high internal gain, good quantum efficiency, and good timing characteristics. Unlike PMTs, SiPMs are also immune to stray magnetic fields up to 15 Teslas [27].

1.8.3 From individual detectors to computed tomography

Thanks to the relatively small footprint of the plastic scintillators coupled to SiPMs, it is possible to arrange them in an array with a pitch of few millimeters, and build an imaging arc suitable for computed tomography (CT). Such a setup was designed and optimized in a previous doctoral work at ETH Zürich [4], with nearly one hundred of these individual detectors in a planar fan-beam arrangement, as depicted on Figure 1.11. The best tomographic reconstruction resolution was demonstrated to be at the time about 2-3 mm.

By rotation of the sample around an axis normal to array plane, such that the sample always remains entirely in the field of view of the detector array, it is possible to acquire a viable sinogram. This sinogram is nothing else than the stack of attenuation patterns at different projection angles. From these projection data, it is possible to reconstruct the cross-sectional image of the sample.

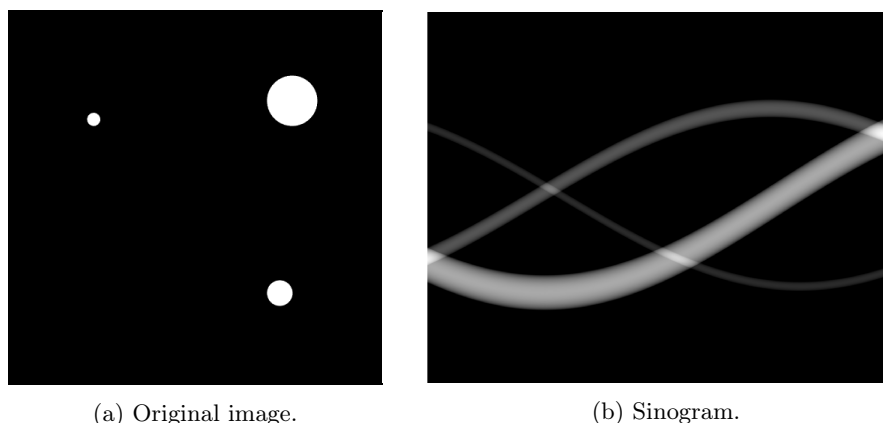


Figure 1.12 – Simulated sinogram and image obtained during a CT reconstruction process.

An example is given in Figures 1.12b and 1.12a. A complete mathematical theory behind this reconstruction process was developed in the last decades and details can be found in specialized literature such as [28, 29].

It should be noted that the whole material decomposition approach developed for 1-pixel setup in Section 1.2 can without effort be extended to the CT apparatus. The reconstructed image is a cross-sectional image of an object; the pixel in the 2D picture contains local values of the attenuation. It means that each pixel can be analyzed independently. For each of them, a system of equations is established and solved. Maps of the different atomic concentrations can be produced as the final output. Chapter 3 will be dedicated to the adaptation of the inherited hardware to make it capable of this energy-selective approach, and to the results subsequently obtained.

1.9 Summary

Starting from the specific properties of fast neutrons in regard to their reactions with matter, it was shown in this chapter that they are indeed suitable for material decomposition of unknown samples, provided that a tunable monoenergetic fast neutron source is available. A compact generator based on the DD reaction was deemed to be a good candidate since it naturally offers an energy range spanning roughly 2 MeV to 3 MeV. Plastic scintillators coupled to silicon photomultipliers were then picked to detect the neutrons.

This elegant solution does not require complex timing electronics and long flight tubes since the spectrum is directly monoenergetic. The generator is compact, the high-voltage requirements are reasonable. The licensing is simple since the amount of activated material and radioactive products is essentially negligible. In terms of safety, there is no decay heat and the neutron output can be turned off at any time.

The next chapter will focus on theoretical and experimental characterization of the neutron spectrum followed by a calibration of the material decomposition technique against reference samples.

Mehr Licht
Johann Wolfgang von Goethe

Chapter 2

Model of the source and calibration measurements

In Chapter 1, the DD neutron source around which the experiment was built was presented in the ideal case, when it outputs a perfectly monoenergetic neutron beam at each emission angle. In reality, **at each angle a range of different neutron energies is emitted**. This chapter will focus on describing and modelling the complex and intricate phenomena influencing the real neutron spectra. Given that some uncertainties remained about these models, a proof of principle followed by a series of calibration measurements based on reference samples will be presented, so that the robustness of the elemental-sensitive technique is demonstrated.

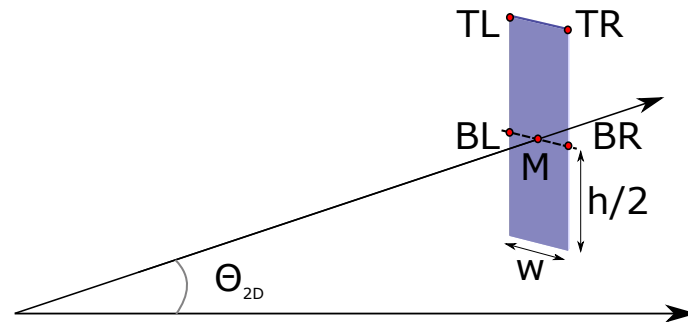
2.1 Simulation of the real neutron spectrum of the source

2.1.1 Geometrical energy spread

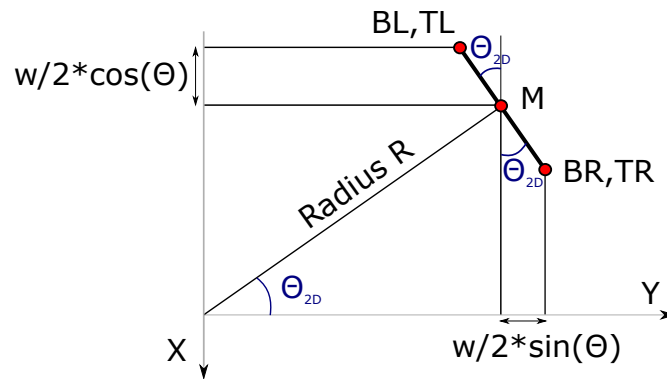
The neutron detector has necessarily a finite non-zero height and width, and therefore subtends a certain angular range. As indicated in Section 1.7.2, the spatial dependency of the neutron energy is related uniquely to the azimuthal angle. Figure 2.1c should be considered as it shows clearly how the azimuthal angle depends on the coordinates of a given point M of the 3D-space with coordinates (x, y, z) in the Cartesian frame. The solution lies in the triangle highlighted in gold in this figure. The segments lengths can be computed through: $AB = y$, $AM = \sqrt{x^2 + y^2 + z^2}$, and $BM = \sqrt{x^2 + z^2}$. Hence the azimuthal angle Θ can be calculated through Equation 2.1.

$$\Theta = \text{acos} \left(\frac{AB}{AM} \right) = \text{acos} \left(\frac{\sqrt{y^2}}{\sqrt{x^2 + y^2 + z^2}} \right) \quad (2.1)$$

To evaluate the magnitude of this effect, a detector presenting a rectangular face to the source is modelled. The detector rotates around the Z axis - corresponding to the target alignment - at a distance R from the origin. The angular position of the center M of the detector is described by the polar θ_{2D} , two-dimensional projection of the azimuthal angle in the basis plane of Figure 1.8; BR, BL, TR, and TL respectively stand for “bottom right”, “bottom left”, “top right” and “top left” corners. Since all the results presented thereafter are computed in the frame of the basis plane, the 2D subscript will be subsequently omitted. Due to the symmetry of the problem, describing the upper half of the detector is sufficient: the energy range covered in both halves is the same. The ensemble is shown from the side in Figure 2.1a and from the top on Figure 2.1b.



(a) Schematic geometrical side view of the generator.



(b) Schematic geometrical top view of the generator.

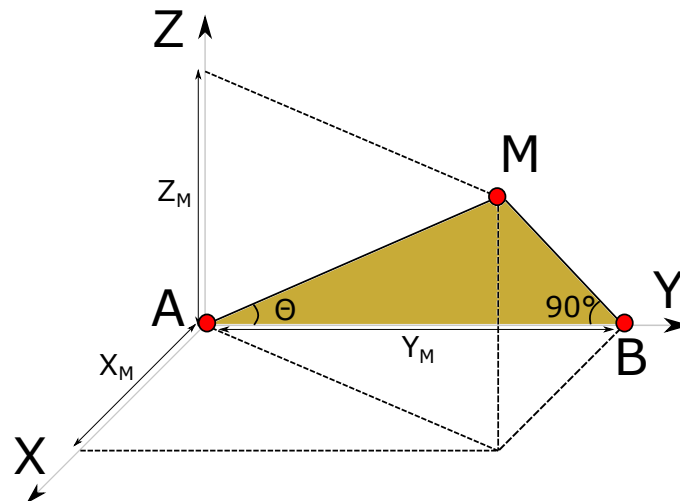
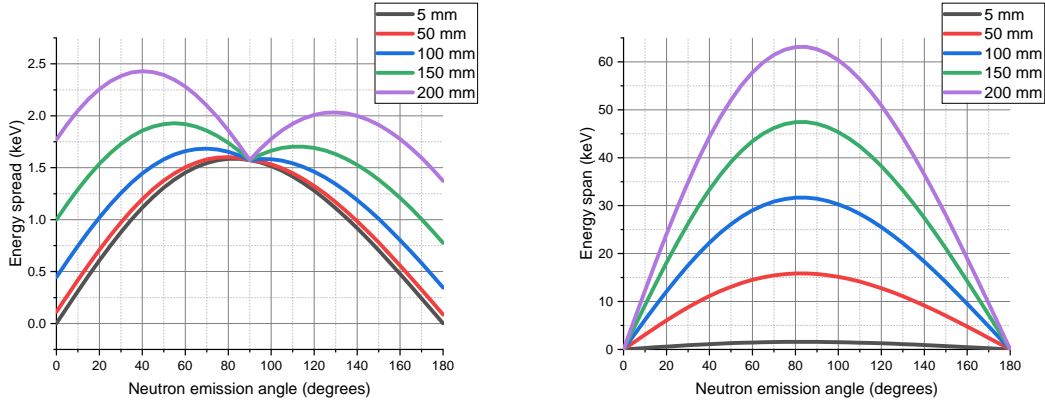
(c) Azimuth angle of given point M of space.

Figure 2.1 – Schematic views of the geometrical situation around the generator.



(a) Varying detector height. Fixed width of 5 mm. (b) Varying detector width. Fixed height of 5 mm.

Figure 2.2 – Sensitivity study on the neutron energy spread due to the dimensions of the detector.

Simple geometrical considerations allow to write the coordinates of each of the corners in a the Cartesian frame defined by Y , the incoming deuteron direction, and Z , the axis of the titanium target. These coordinates are summarized in Table 2.1. Having the complete formulation of the azimuthal angle for any points of space, the energy spread due to the size of the detector can be computed with Equation 2.2 since the corners represent the possible extremes in terms of azimuthal angle. As a conservative approach, the spectrum is considered to be flat in that range, although the geometry would typically favor only some energies due to the prevalence of some of azimuthal angles.

Table 2.1 – Location of the corners defining the upper half of the neutron detector in Cartesian coordinates.

Corner	x	y	z
BR	$-R \cdot \sin(\theta) + \frac{w}{2} \cdot \cos(\theta)$	$R \cdot \sin(\theta) + \frac{w}{2} \cdot \cos(\theta)$	0
BL	$-R \cdot \sin(\theta) - \frac{w}{2} \cdot \cos(\theta)$	$-R \cdot \sin(\theta) - \frac{w}{2} \cdot \cos(\theta)$	0
TR	$-R \cdot \sin(\theta) + \frac{w}{2} \cdot \cos(\theta)$	$R \cdot \sin(\theta) + \frac{w}{2} \cdot \cos(\theta)$	$\frac{h}{2}$
TL	$-R \cdot \sin(\theta) - \frac{w}{2} \cdot \cos(\theta)$	$-R \cdot \sin(\theta) - \frac{w}{2} \cdot \cos(\theta)$	$\frac{h}{2}$

$$E_{\text{span}} = \left[\max_{i=BR,BL,TR,TL} (E_i) \right] - \left[\min_{i=BR,BL,TR,TL} (E_i) \right] \quad (2.2)$$

To quantify the magnitude of this geometric effect, a sensitivity study was carried out with different detector configurations. The height and the width were varied independently from 5 to 200 mm. The detector was simulated to be at one meter from the source. The results are summarized in Figure 2.2a and 2.2b. The height proved to have a very reduced effect, explained by the fact that the azimuthal angle changes very slowly with respect to the height. On the other other hand, the effect is much stronger when it comes to the width. Overall, the total effect remains somewhat negligible: the typical detector has surface facing the source of 5×8 mm, which means that both dimensions bring a spread of few keV at most, or below 0.1% compared to the main neutron energy. Larger detector configurations are used later in this study, but the geometrical spread was found to always be a secondary effect.

2.1.2 Inherent energy spread

2.1.2.1 Physics of a solid target

A more significant contribution to the energy spread comes from the solid implantation type target design. In an ideal case, all the fusion events happen at the surface of the target when the incoming deuteron still has its original energy. In reality, in the case of a solid titanium target, it is likely that the deuteron will first travel a little distance within the target, gradually losing energy through Coulomb interactions with the host material. After slowing down, the deuteron will finally undergo fusion at a reduced energy, which in turn means a different resulting neutron energy. The case of an outgoing angle of about 60° is depicted in Figure 2.3. At this position, a reduced deuteron energy leads to a decrease of the generated neutron energy. Since the DD fusion cross-section at lower deuteron energies is also lower, as shown previously in Figure 1.6, the contribution of these lower energy neutrons to the overall spectrum diminishes as well.

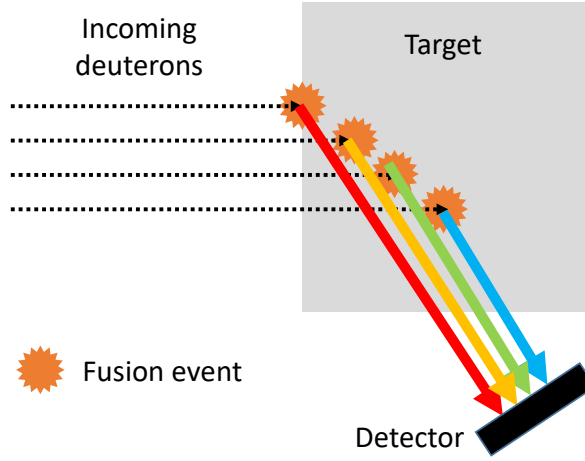


Figure 2.3 – Schematic illustrating the different depths at which fusion events happen. Since the deuterons lose energy while progressing in the target, they undergo fusion at various energies and the resulting neutrons also have a different energy.

In order to study the influence of this phenomenon, the incoming deuteron beam was modelled from its initial energy until its complete absorption by the target. At each depth within the target, all the relevant parameters are computed so that the fusion rate can be finally calculated. Equation 2.3 is used to describe the differential fusion rate at a given location. The flux of deuterons ϕ - with an energy E_d , going through a target with a concentration N of deuterons and a corresponding fusion cross-section $\sigma(E_d)$ - yields a number of neutrons per unit area and time $dY(E_d)$ in a layer of thickness dx .

$$dY(E_d) = \phi \cdot \sigma(E_d) \cdot N \cdot dx \quad (2.3)$$

Equation 2.3 can be re-written to make the differential yield per unit deuteron energy appear, it becomes then Equation 2.4.

$$\frac{dY(E_d)}{dE_d} = \phi \cdot \sigma(E_d) \cdot N \cdot \left(\frac{dE_d}{dx}(E_d) \right)^{-1} \quad (2.4)$$

Some phenomena might lead to some absorption of deuterons, but the effect becomes stronger only at high depths, when the deuteron energy is already low. Since the fusion cross-section is already critically low in that low-energy range, as shown in Figure 1.6, this part of the spectrum will barely be measurable. As a conservative approach to determine the maximum energy spread, the flux of deuterons was considered constant throughout the target.

Theoretically, the deuteron energy spectrum throughout the target is continuous from its maximum energy - equal to the energy of the ion beam when it reaches the surface of titanium - to zero - when it has transferred all its to the host material. To numerically solve the problem, the deuteron spectrum is finely discretized into energy bins (and corresponding depths) over which the energy of the deuteron and thus the cross-section and the stopping power, and the implanted deuteron concentration, are considered approximately constant. Since the energy binning is fine¹, these “constant” physical variables were considered to be a valid approximation. Each bin is considered independently and, for each of them, the resulting neutron energy in all direction of space is computed. At the end of all the independent processes, the separated neutron spectra from each energy bins are summed back together to obtain the final neutron spectrum.

Each of the aforementioned input parameters carry assumptions with varying degrees of uncertainty. The DD fusion cross-section $\sigma(E_d)$ has been reasonably well reported in international databases such as [30]. The stopping power $\frac{dE_d}{dx}(E_d)$ can be reliably obtained from [31]. One of the main uncertainties lies in the actual deuterium implantation within the target: the actual ratio deuterium/titanium x in the hydride TiD_x can be as high as 2 [21], but it can be lower as well; the concentration profile is also very likely not constant throughout the target, it might be depleted at the surface because of thermal effects leading to titanium hydride instability and outgassing of the deuterium [21]. In general, the deuterium implantation within the target remains unknown both in amplitude and in shape. Finally, how the impact vector of the deuteron changes before fusion occurs plays a non-negligible role. Until now, simplified models of the situation - such as in Figure 2.3 - described it as aligned with the forward 0° direction. But since it interacts stochastically with the target before undergoing fusion, it is unlikely to always remain aligned with this direction.

Because both the deuterium implantation and the deuteron impact vector are instrumental in shaping the neutron spectrum, they are detailed further in the two following sections 2.1.2.2 and 2.1.2.3.

2.1.2.2 Deuterium implantation

Some complex experimental techniques such as associated particle measurements using the non-neutron particle produced during the fusion - an Helium-3 nucleus - would allow the online monitoring of the deuterium implantation. The online aspect is critical as the target behavior might show dramatic changes during operation because of evolving thermal and chemical conditions. This coincidence measurement allows tagging the neutron with the alpha particle. It is known that both particles are emitted in almost opposite directions. It is possible to select a given direction of emission with angle-selecting detectors such as in [32]. Using a surface barrier detector, the energy of the He-3 particle can be estimated. From the direction and energy information their starting point - i.e. the fusion location within the target - can be reconstructed. From the aggregated data coming from different scanned directions of emission, the detection rate being directly proportional to the fusion rate, it is possible to compute back from Equation 2.4 the deuterium implantation profile. However, this experiment was technically too difficult and not feasible to implement in the case of the PSI generator.

Instead, a two-fold approach combining experimental data from a high-resolution Helium-3 neutron spectrometer and computer models was adopted. The experimental characterization will be

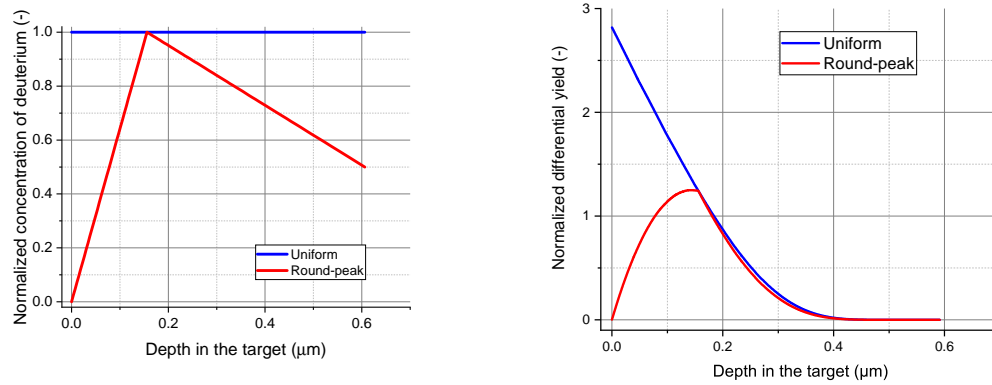
¹Typically smaller than 0.1% of the initial deuteron energy, e.g. 80 eV bins for a 80 keV deuteron beam.

presented in detail in Section 2.2. The modelling will be discussed in the next paragraph.

Three different models were studied: two extreme cases with the least and the most deuterium-saturated target models, and a third model somewhat in between. The “Dirac” model describes the ideal situation when the target only has deuterium at its surface and therefore when fusion events happen only at the surface, with a resulting purely monoenergetic neutron spectrum at each angle. A fully deuterium-saturated target model, named “uniform”, assumes a constant deuterium concentration throughout the target, allowing fusion at all possible deuteron energies. It offers subsequently the widest possible range of neutron energies. Finally, the “round peak” model was developed based on observations published in [33]. It assumes a rising concentration of deuterium from 0 to the maximum at one fourth of the range, then slowly decreasing from the maximum to half of the maximum value at the end of the deuteron range. Physically, it assumes complete depletion at the surface - due to outgassing for example - and a partial one at the end of the range - which could represent phenomena such as diffusion. All the three profiles were normalized so that the maximum deuterium concentration would correspond to $x = 2$ in TiD_x . The “Dirac” profile was not displayed as it would be reduced to a Dirac distribution centered on a depth of zero. The two “thick-target” profiles - “uniform” and “round-peak” - are illustrated on Figure 2.4a. To understand the effect of the deuterium depletion at the surface and the end of the range of the deuteron, the normalized neutron yield is plotted versus the target depth in Figure 2.4b. It represents how many neutrons are produced per deuteron path length. The main effect on the yield is clearly the depletion at the surface. It was expected because the fusion cross-section is much higher at high deuteron energies, i.e. near the surface. The end-of-the-range effect is secondary as it is the reverse case: the deuteron energies are nearing zero, and so is the fusion cross-section. Overall, for the same deuteron input parameters, the “round-peak” model gives a total $4\text{-}\pi$ output which is only 53.6% of the “uniform” one.

An extract of the resulting neutron spectra is shown on Figures Figure 2.6a, 2.6b, and 2.6c respectively for an incoming deuteron with an energy of 80 keV. The maximum of the distribution at each angle was normalized to one for better clarity. The modelled 1-pixel neutron detector stands at 0.915 m from the source and has the following dimensions: 45 mm width, 80 mm height, and 16 mm depth. It represent a stack of twelve of the smaller scintillators that were mentioned in Section 1.8.2, standing in two rows of six. For these dimensions, the geometrical energy spread mentioned in Section 2.1.1 was found to be still negligible compared to the inherent energy spread. The full width at half maximum (FWHM) - an attempt to characterize the energy spread at each angle - is plotted in Figure 2.5. The “Dirac” case was once more not plotted here because the corresponding FWHM is necessarily always equal to zero.

Generally speaking, the inherent energy spreading is largely dominating the much smaller spread due to the size of the detector, with values between 10 keV and 100 keV for the FWHM. Since the “round-peak” distribution tends to cut the high- and low-energy part of the neutron spectrum, the latter tends to become flatter and the FWHM to increase compared to the “uniform” distribution. Looking at each angle, it is clear that the energy range itself did not increase: minimum and maximum energies remain identical. As expected from the angular dependence of the neutron energy detailed in Section 1.7.2, the spectra are wider at the extremes of 0 and 180°, while it is almost monoenergetic close to 90°.



(a) Spatial deuterium distribution in the titanium target for the “uniform” and “round-peak” models.

(b) Normalized yield for the “uniform” and “round-peak” models.

Figure 2.4 – The “uniform” and “round-peak” deuterium distributions and their effect on the neutron yield.

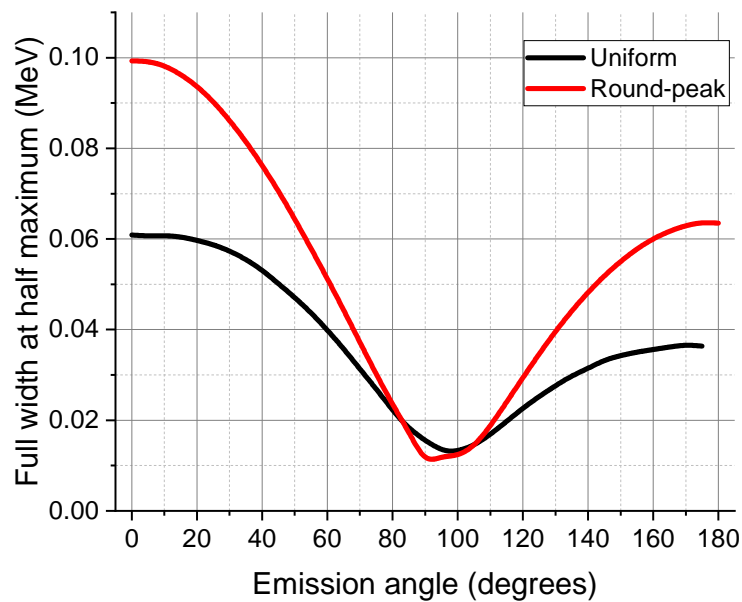
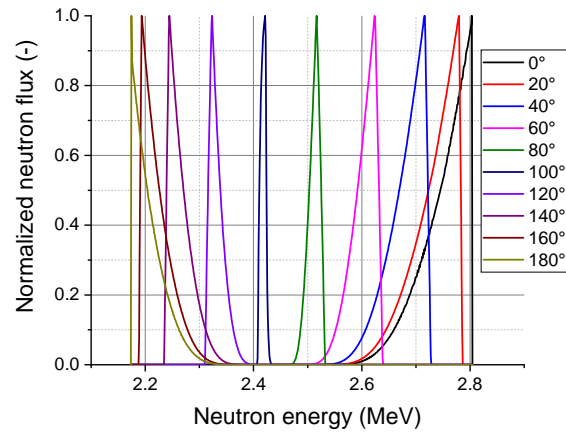
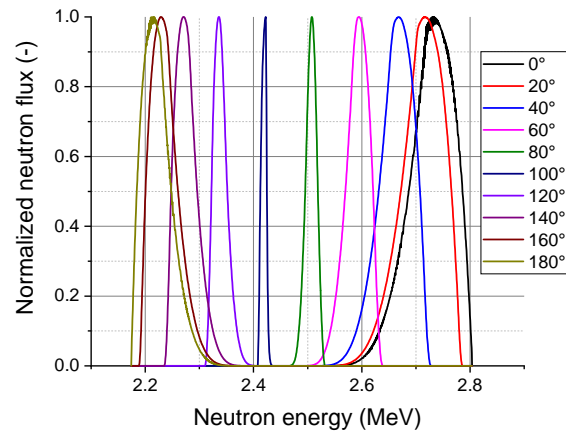


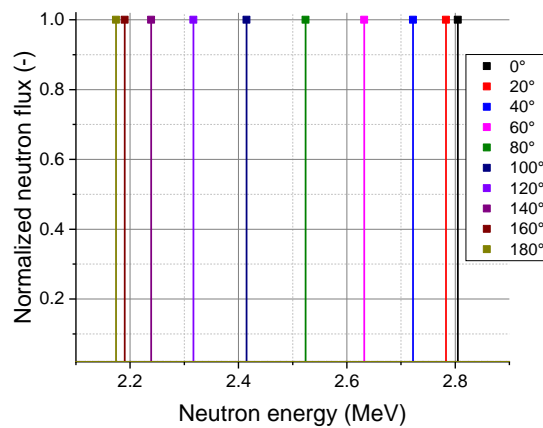
Figure 2.5 – Resulting full width at half maximum for the two “thick-target” neutron spectra models for a 80 keV deuteron beam.



(a) Uniform deuterium profile.



(b) Round peak deuterium profile.



(c) Dirac deuterium profile.

Figure 2.6 – Simulated energy spectra at different emission angles, for an incoming deuteron beam of 80 keV and different models of deuterium implantation in the target.

2.1.2.3 Deflection of the deuteron before fusion

The deuterons slowing down in the target interact with matter and are deflected from their initial straight path. It means that they can undergo fusion with an impact vector which is not aligned with the initial forward direction. Necessarily, the neutrons born from these angle-shifted fusion events will be emitted in shifted directions as well. As an illustration, Figure 2.7a shows a simplified version of the situation: only three incoming deuterons are shown. Deuteron 1 has an impact vector aligned with the 0° forward direction. The impact vector of Deuteron 2 is shifted by $+5^\circ$, and the one of Deuteron 3 by -10° . A detector standing in a fixed position at 90° will see a “ 90° ” neutron from Deuteron 1, but also a “ $90^\circ - 5^\circ = 85^\circ$ ” neutron from Deuteron 2, and a “ $90^\circ + 10^\circ = 100^\circ$ ” neutron from Deuteron 3.

To quantify this effect, it was first necessary to estimate the angular distribution of the impact vector. Adequate stochastic simulations were carried out with SRIM [31]. It is possible to get from this code the full travelling history of a deuteron within the TiD_2 target. Before each interaction, its 3D location is recorded. At each position, the impact vector was considered to be aligned with the segment linking the $(n - 1)^{\text{th}}$ to the n^{th} position. The azimuth angle could then be computed according to Equation 2.1. Many ions were simulated and the probability density function (PDF) of the impact vector azimuth is shown in Figure 2.7b. It is rather clear that the small-angle impact vectors are dominating.

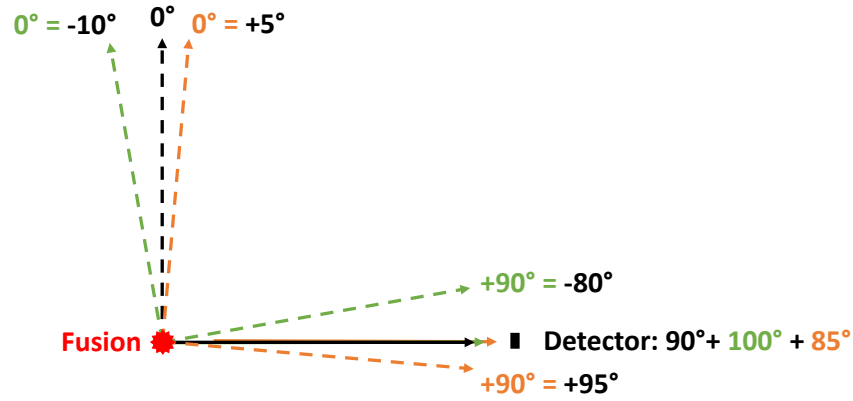
Although the PDF is defined in the range between 0 and 180° , it was not forgotten that this is only because of the definition domain of the function acos . In the end, deuterons with an impact vector shifted by 0° to 360° were simulated. This range was discretized in bins of one degree. For each bin, the resulting neutron spectrum around the source - available with different deuterium implantation models from Section 2.1.2.2 - was then accordingly weighted with the aforementioned PDF.

Figure 2.7c summarizes the results by comparing the neutron spectra at 0° , 90° , and 180° with and without the deuteron angle effect. For the sake of clarity, only the results based on the “uniform” deuterium implantation are presented at three different angles. The effect on the other deuterium implantation models and the other emission angles are very similar. A more comprehensive comparison of the different models - 3 implantation models times 2 impact vector models - with experimental data will be shown along with the proof principle of the energy-selective measurements in Section 2.3.

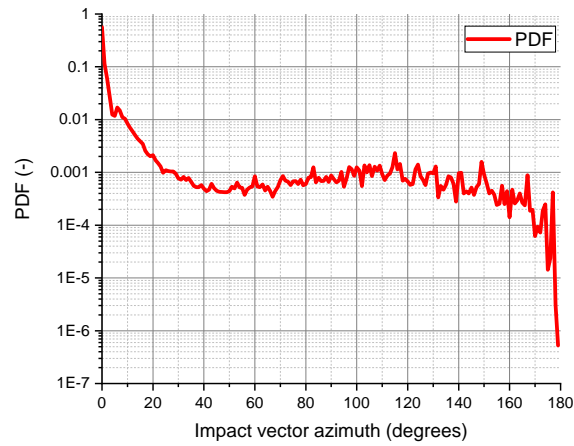
All the experimental results presented thereafter will feature the emission direction as the plots abscissa. Figure 2.8 is given to the reader in order to give a better sense of the equivalence between emission direction and spectrum-averaged neutron energy for the five different neutron source models introduced until now.

2.1.2.4 Further assumptions on the fusion physics models

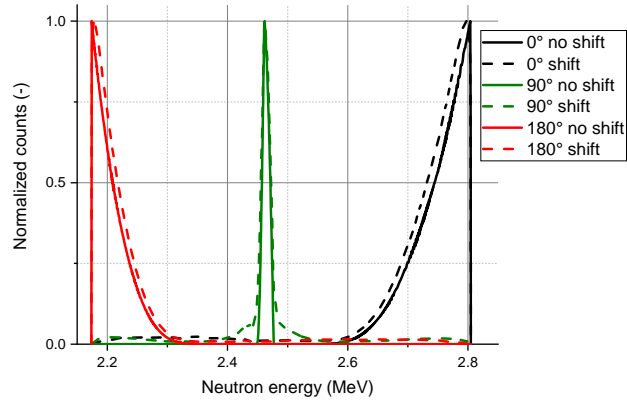
The deuteron source was considered as purely monoatomic - i.e. containing only D^+ ions - when in reality some of the ions are D^{2+} or D^{3+} . An experimental determination of the exact non-monoatomic fraction was not has not been carried out yet with the PSI generator. Although prototype generators such as this one are unique machines, it was decided to study the non-monoatomic fraction of a comparable ion source, which was measured to be on the order of 15% [34]. That 15% produces neutrons about 20% as efficiently as the rest due to its lower per-nucleon energy upon acceleration [35]. Overall, it means that they are effectively contributing to roughly 3.4% of the overall source neutrons. This contribution is therefore quite small and was neglected in simulations. It may contribute to the overall uncertainty attached to the models.



(a) Effect of the angular shift of the deuteron impact vector on the frame of reference.



(b) Probability density function (PDF) of the azimuthal angle of the impact vector.



(c) Effect for selected detector positions.

Figure 2.7 – Effect of a realistic deuteron impact vector on the final neutron spectrum.

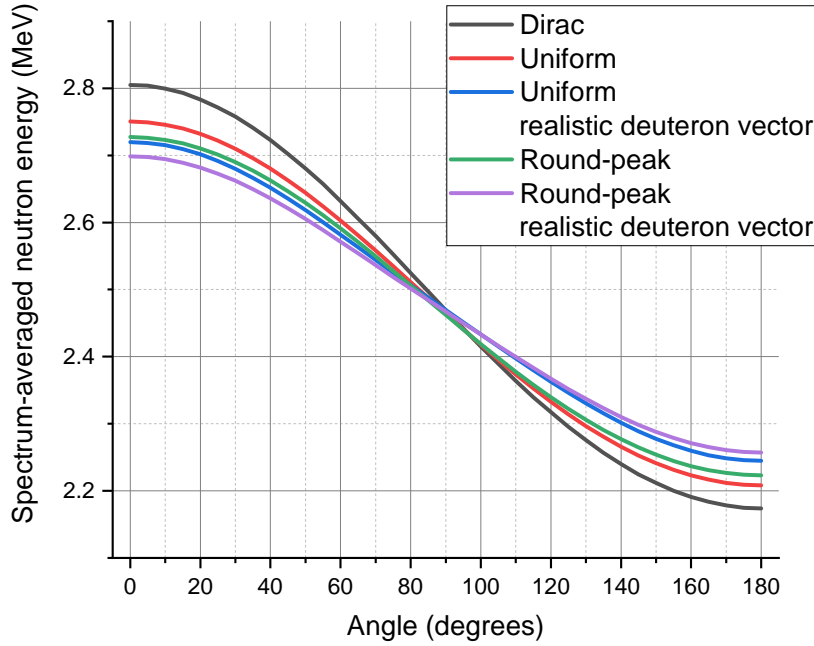


Figure 2.8 – Equivalence between the spectrum-averaged neutron energy and the neutron emission direction.

A simulation was also carried out to prove that the high-vacuum area in which the deuterons are flying between the ion source and the target has a negligible influence on the trajectory and energy of the deuterons. A beam of 80 keV deuterons was simulated in SRIM [31] flying in 10 cm of dry air with a density of $1.25 \cdot 10^{-8} \text{ g} \cdot \text{cm}^{-3}$, corresponding to a pressure of 10^{-5} bar or 1 Pa, a conservative estimate of the pressure in that region. Pressure sensors indeed indicated a pressure of about 10^{-4} bar in the ion source and 10^{-9} bar next to the turbomolecular pump². In spite of this conservative approach, only about 0.1 % of the particles interacted with the medium and therefore the beam characteristics were not significantly affected. This effect was not further considered in this study.

Although the custom models presented in the whole Section 2.1.2 carry some degree of uncertainty, they proved to be very useful as they could provide the best guess in terms of neutron spectrum which helped greatly in the nuclide and sample investigations that will be presented in the subsequent sections.

2.2 Experimental characterization of the PSI generator neutron spectrum

Spectroscopic measurements were realized with a high-resolution fast neutron spectrometer based on a gridded Helium-3 ionization chamber of type FNS-1 [37] from Jordan Valley Applied Radiation Ltd. The sensor comes with its own pre-amplifier and needs a matching linear amplifier with a shaping time of $8 \mu\text{s}$, which in this case was a Canberra 2022 Spectroscopy Amplifier [38]. The output of the amplifier was sent to a digital oscilloscope PicoScope 5244A [39], used to record

²This includes the correction factor of 2.4 needed for pure dihydrogen gas, for the Pfeiffer pressure gauge model PKR 251 [36].

the signals for later processing in order to perform the function of a multi-channel analyzer. The chamber is not position-sensitive, and has relatively large dimensions of about ten centimeters in diameter and length. Therefore, the objective was not to obtain an advanced characterization like the one with the associated particle technique mentioned in Section 2.1.2.2, but rather to get a potential validation of the custom models developed in the frame of this study.

The spectrometer is based on the capture reaction introduced in Section 1.8.1 and described by Equation 2.5. The neutron is captured by the Helium-3 nucleus, and as output a proton and a triton are emitted. The Q-value of the reaction is 0.764 MeV. The chamber has its own thermal neutron shield - consisting of two millimeters of boron nitride powder sandwiched between a half-millimeter thick sheet of Cadmium and a one millimeter thick stainless steel sheet - which reduces the thermal contribution by a factor of 50 to 100, according to the manufacturer. However, neutrons can be also thermalized within the detector itself. Since the capture reaction with Helium-3 has a very high cross-section in the thermal range - for example about 5316 b at 25 meV against only 0.7 b at 2.5 MeV [5] - a very large peak can be registered in that region. Scattered neutrons from the environment might also affect the results by creating a continuum of pulses. In the MeV range, the thermal shield is not so efficient. To solve the scattering issue, a “blinding cone” measurement was always added: a thick piece of high-density polyethylene essentially attenuates completely the direct contribution of the fast neutron beam, leaving only the scattered component. This measured parasitic scattered component was then subtracted from the main measurement, leaving only the direct contribution.



The spectrum of the source was measured at three different approximate emission angles: 0°, 90°, and 180°, at about half a meter from the source. Based on the kinetics theory presented in Section 1.7.2, even the “thick”-target models of Section 2.1.2.2 agree on the fact that in the 90° region, the spectrum is almost monoenergetic, with a FWHM of only few tens of keV. Preliminary measurements showed that the experimental data at 90° suggest a much larger FWHM, on the order of 200 keV. Hence, the measured spectrum at that angle can be considered to be the impulse response of the detector. Relying on that assumption, the spectra obtained from the different spectral models were convolved with this impulse response. The results of the convolution were then compared to the experimental spectroscopic data. The result is shown on Figure 2.9. For the sake of conciseness and because the results of the convolution were very similar for the three models, only the results obtained with the “uniform” model are shown.

The experimental peaks are not exactly aligned with the results of the convolution. This could be explained by the uncertainty of the detector angular location, which was done manually. The 90° region sees the sharpest energy peak and energy variation, as shown in Figure 1.9. If the spectrometer is at an angle slightly different than expected, it might capture neutrons at a different energy than expected, making the reference being then slightly off. A sensitivity study coupled to a more accurate spectrometer location system would help to reduce this uncertainty. Due to time constraints, it was however not possible to implement them within this work. The low-energy tail for the 180° case is not perfectly reproduced. It might come from the fact that the reference “impulse response” still includes some residual scattered contribution, despite the effort to suppress the scattered component with a blinding cone correction. When the impulse response is convoluted at other angles, it may induce an overestimated tail.

The main observation that can be made is that the detector features an inherent blur - which can be characterized by the FWHM at 90° - of almost 200 keV, which means it is difficult to resolve the neutron spectra below that limit. It is of a similar order of magnitude as the energy spreads modelled in Section 2.1.2.2. This also explains why the results of the convolution with the different models were so close to each other. Although the experimental validation of said models using

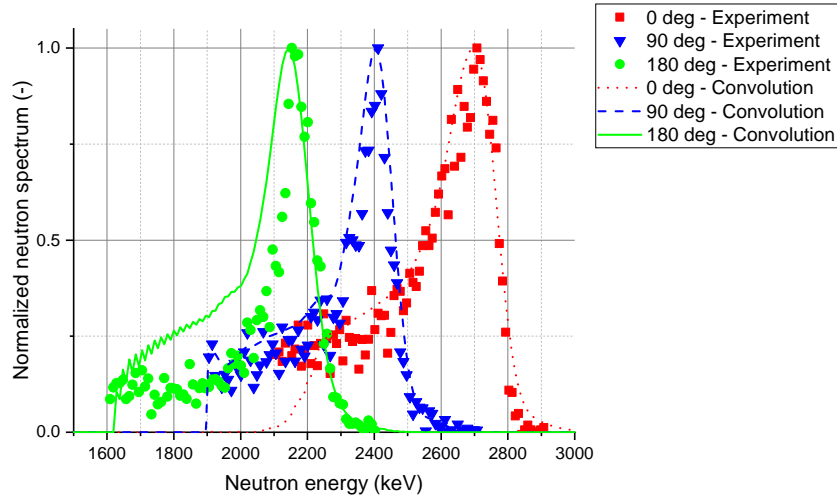


Figure 2.9 – Comparison of the experimental neutron spectra obtained with the Helium-3 spectrometer and the result of the convolution of the simulated spectra with the impulse response of the detector.

these measurements is of limited precision and significant uncertainties remain, the agreement is generally good and supportive of the assumptions made and the models used. These results are described in the frame of a comprehensive effort of characterization of the PSI neutron generator in [40].

2.3 Proof of principle with selected samples

After gaining a deeper understanding of the way the PSI neutron generator is emitting neutrons, the next logical step was to select a couple of well-characterized homogeneous samples and proceed with attenuation measurements to validate the models and prove the feasibility of the energy-selective technique.

2.3.1 Measurement apparatus

As demonstrated in Section 1.7.2, by scanning the azimuthal angle, it is possible to measure the attenuation at different neutron energies. In the “basis plane”, a simple rotation around the axis of the titanium target is needed to browse the azimuthal angle. Thus the basic design idea of the measurement apparatus is to carry the neutron detector and sample on a circular trajectory around the neutron source. It was deemed necessary to make the system entirely autonomous and remotely steerable. It is indeed not possible for the user to remain in the experiment room when the generator is in production mode, for obvious safety reasons. Since the experiments can last several hours, the acquisition procedure should be automated so as not to depend on user manipulations during the measurement. While it is running, only an occasional check of the vital parameters of the generator and detectors is needed. It is performed remotely from the control room.

The neutron detector is mounted on an aluminum plate, itself mounted on three omnidirectional ball casters. From now on, this ensemble will be referred to as the “trolley”. On the trolley, a stepper motor is installed. A cogwheel is attached to its shaft. The cogwheel was designed to match exactly the gearing of a large aluminum arc-shaped track, henceforth referred to as the

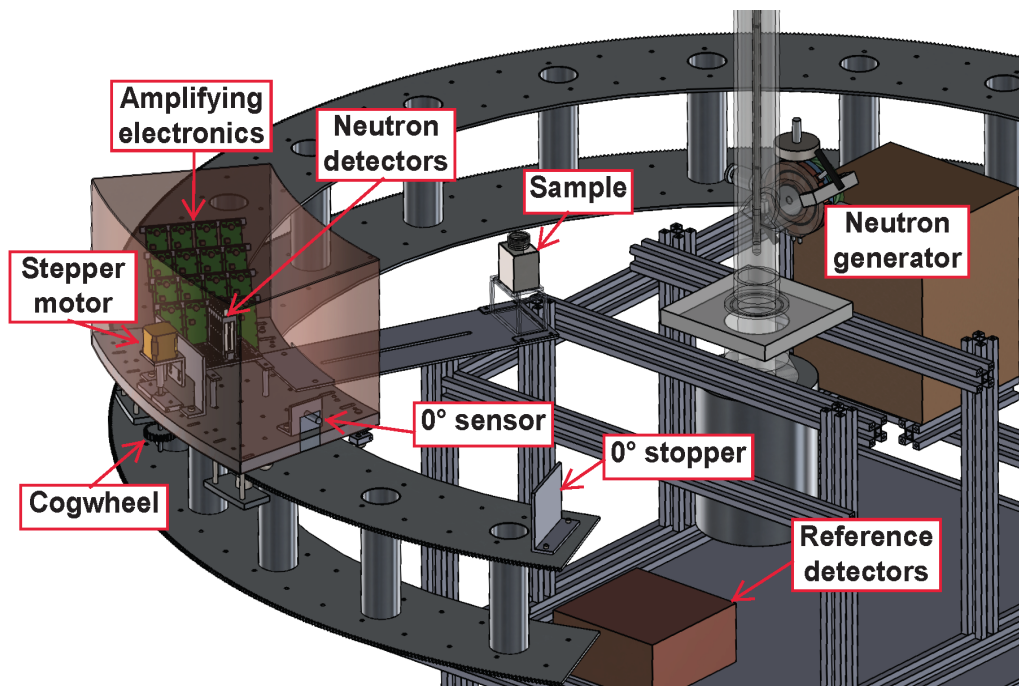


Figure 2.10 – CAD model of the measurement setup.

“track”. This track has a radius of about one meter and its outer side is geared while the inner one is flat. The region between inner and outer diameter is large enough so it can accommodate the wheels of the trolley. On the outer diameter, contact between the trolley and the track is made via the gear. On the inner side, two rubber wheels attached to the trolley complete a permanent three-point contact, and therefore an accurate guiding of the trolley motion along the track. When a measurement set starts, the trolley position is automatically initialized via a dedicated contact sensor which touches a fixed stopper figuring the 0° position. For practical purposes, this contact sensor has an RC filter which debounces the signal: since there are vibrations, it can happen that the contact signal switches rapidly from open to close status; it could send contradictory information to the driving electronics. A similar stopping arrangement exists at around 182° to stop the trolley in the event of a malfunction.

A digital drawing gives an overview of the situation in Figure 2.10. The stepper motor is visible in gold, its own shaft is linked to the cogwheel shaft below by an Oldham coupling, which can withstand some misalignment of the shafts. Just behind it stands the amplifying electronics in green, and in grey the stack of neutron detectors. This sensitive electronics part is protected by an RF shield made of thin copper, semi-transparent on the picture. The shield also reduces light ingress, which is beneficial since the detectors are light-sensitive. Several layers of opaque materials provide redundant protection against light as the shield is not perfectly light-tight. On the extender plate attached on the right of the trolley, a typical sample is visible. The neutron generator itself stands a bit more to the right. Figure 2.11 shows an actual photograph of the setup.

The bi-polar stepper motor [41] is powered through a Big Easy driver board [42] and the ensemble is piloted via an Arduino Uno [43]. To communicate remotely with the Arduino board, the latter was connected to a Raspberry Pi 3 Model B [44] which supports standard Ethernet connections. It means that only a power cable and an Ethernet cable with 8P8C connector were needed for the trolley to work properly. The Ethernet cable provides excellent shielding against stray electromagnetic fields, while standard USB cables - such as the ones that can be connected directly to an Arduino Uno board - offer a rather poor one.

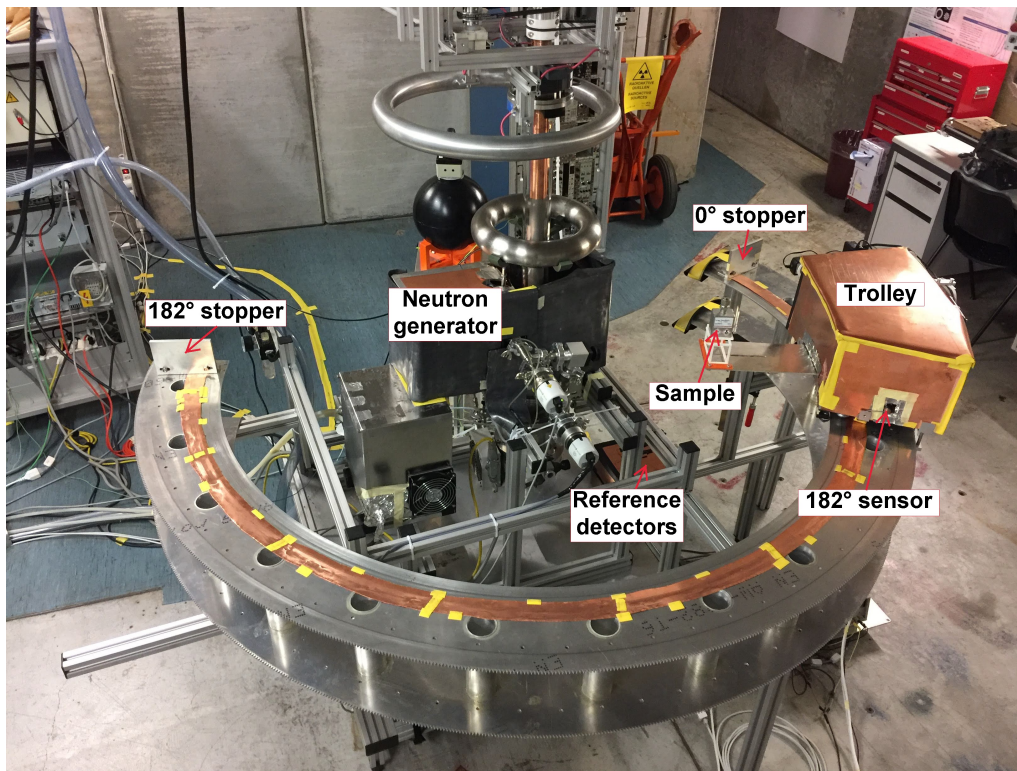


Figure 2.11 – Photograph of the measurement setup.

The neutron signal processing chain detection is identical to the one presented in Section 1.8.2. The output signal of the SiPM is processed by an amplifying board developed in a previous study [2]. If the signal amplitude is above a certain threshold - designed to cut undesirable Bremsstrahlung pulses as described in Section 1.8.2 - a count is registered. A flip-flop on the board is used to enable easy pulse counting by the Arduino Due [45]. When the signal goes above the threshold, the flip-flop latches high until it is counted and reset by the Arduino Due. The Arduino Due board also plays the role of the timekeeper and is connected via USB to the previously mentioned Raspberry Pi which can transmit all the information remotely. Twelve identical detectors with separate signal-processing chains are connected to the Arduino Due to get more counting statistics in a reduced amount of time, with the counts summed together and considered as one single neutron detector. All the data is handled via a unique overarching software, implemented in Matlab [46]. This software sends and receives data to and from the Raspberry Pi, which in turn communicates with the two Arduino boards. The whole network routing is summarized in Figure 2.12.

Because the generator is chemically and thermally a dynamic system, its output can slightly vary over time. To be sure that a reduction of the neutron flux behind the sample is indeed due to attenuation through matter and not to a temporary output fluctuation, four detectors with a similar detection chain were placed below the generator, at a fixed position visible in Figure 2.10. The counts registered on the trolley are then normalized to the counts recorded by these reference detectors.

2.3.2 Measurement method

The foundation of the quantitative elemental analysis lies in the comparison of the neutron flux with and without a sample in the field of view of the neutron detectors, like it has been described

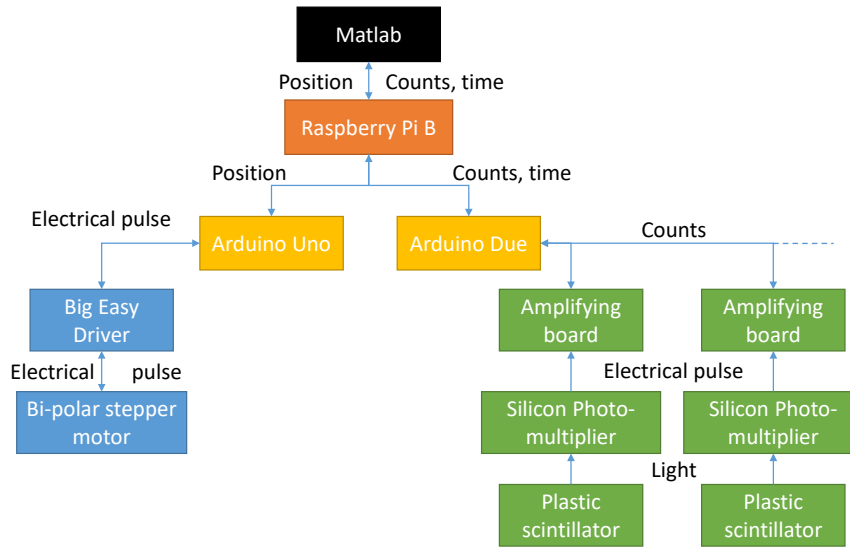


Figure 2.12 – Information routing overview of the measurement setup.

in Section 1.3.

However, it is possible that some spurious counts are registered due to various environmental contributions. The contribution of Bremsstrahlung X-rays should be negligible because the threshold within the amplifying electronics was previously tuned [23] in order to completely discard them. The experimental setup is located in the middle of a bunker of dimensions $6.7 \times 6.8 \text{ m}^2$, with a ceiling at 3 m from the ground. The walls are made of reinforced concrete blocks. A significant amount of neutrons can be scattered back in the detectors. The sample itself can also induce some scatter depending on its nature and size because it sits usually at less than 50 cm from the detectors.

To account for those two sources of scatter, two methods were applied in parallel. For the room scatter, a “blinding cone” measurement I_{BC} was added to the list. Instead of a regular sample, a very thick block of pure high-density polyethylene was placed in the field of view of the detector. With 21 cm of thickness, more than 99.75% of the direct component scatters within the material. Stochastic simulations showed that the effect of neutrons scattered by the blinding cone eventually reaching the detector was negligible. On the other hand, the overall scattered component - which comes from all directions of space - is only negligibly attenuated by the blinding cone. By subtracting the result of this blinding cone measurement from the “with sample” and “without sample” data, the room scattering and also dark counts due to the influence of the environment on the detection chain are corrected.

Concerning the sample scatter, it is experimentally more complicated to measure, therefore a simulation path was taken. The flux after the sample was modelled with the Monte Carlo code MCNP6 [47]. With an F4 tally, the average flux in a cell representing the detector was evaluated. Since it is possible to bin the results of the tally in energy, the binning was selected so that there would be a clear difference between direct and scattered component. For example, with a chosen monoenergetic neutron beam of 2.000001 MeV, all the neutrons registered in the bins up to 2 MeV represent only scattered neutrons, and the above 2 MeV bin is the direct flux only, because essentially all scattering events will move the neutron energy below the 2 MeV threshold. Overall, the two scatter corrections can be brought in to modify Equation 1.2 into Equation 2.6.

$$N_i = \frac{1}{\sigma_i \cdot \tau} \cdot \ln \left(\frac{I_\tau - (I_{BC} + I_{MCNP})}{I_{emp} - (I_{BC} + I_{MCNP})} \right) \quad (2.6)$$

It should be noted that the nature of the sample should be known in order to simulate it with MCNP6. This might seem contradictory since the main goal of this study is the investigation of unknown samples precisely to determine their nature. Luckily, the scatter contribution due to the sample can remain negligible if the latter is not of very large dimensions and does not sit too close to the detectors. For example, a typical sample of about 100 cm³ located half a meter away from the detector impacts the attenuation by less than 1%. The unknown samples investigation results will be only marginally affected by sample scattering. All the experimental data presented hereafter have been corrected for room- and sample-scatter.

2.3.3 Exposure time

An uncertainty study was carried out to characterize the random error due to the neutron count acquisition Poisson statistics. The mathematical details are given in Appendix Section C. The experimental results will hereafter be presented with an error bar of one relative standard deviation $\pm \kappa_{rel}$, corresponding to a confidence interval of 68%, i.e. the probability that the real value is within this error band if considering only Poisson counting uncertainty propagation. Higher numbers of counts generally means lower statistical uncertainty but require longer acquisition times. With some preliminary measurements, empirical standard deviation values were computed in order to determine an optimum measurement time.

With an 80 keV deuteron beam resulting in a 4π -output of about $2.2 \cdot 10^7$ n·s⁻¹, the following measurements were carried out: blinding cone, flat field, and with sample, namely alumina - Al₂O₃. Since the output is forward-biased, two neutron emission angles were studied: 0° and 110°. They represent practical high and low points of the real neutron output of the generator. For an arbitrarily selected exposure time of 219 seconds for each measurement, the counts presented in Table 2.2 were registered. According to Equation C.13, the relative standard deviation on the total macroscopic cross-section was calculated and is presented in the same table. Overall, it is bound between about 1.6% to 2.6%.

Varying the measuring time of the blinding cone affects the final error only marginally: doubling it would only reduce the relative error interval down to 1.5 and 2.5%. The effect is a bit stronger for the flat field: double measuring time results in a reduction of the interval down to between 1.4% and 2.3%. The strongest influence comes from the sample measurement itself: with double measuring time, the interval is reduced to between 1.3% and 2.1%. Some samples - such as steel - might be up to twice as absorbing per unit thickness than some other samples, which in this case means poorer counting statistics. However, in that case the final maximum statistical error was estimated to not exceed 3.3%, which was considered acceptable.

In order to balance optimization of the statistics of acquisition and to keep parameters consistent from one sample to the next, the final measurement time was chosen to be 200 seconds. In the worst case - at lowest output with a very absorbing sample - the relative error on the total macroscopic cross-section is expected to be bound between 1.6% and 3.4%. With a measurement every 5° degrees between 0° and 180°, adding up the time necessary for trolley positioning and other electronics dead time, each case then requires about two hours and fifteen minutes. Three to four cases can easily be treated during a standard day.

Table 2.2 – Counts registered for a 219 seconds exposure in the case of a 4π -output of about $2.2 \cdot 10^7 \text{ n}\cdot\text{s}^{-1}$.

		At 0°	At 110°
Alumina Al_2O_3	Main counts	82720	58501
	Reference counts	25382	25217
Blinding cone	Main counts	32616	28835
	Reference counts	27162	25126
Flat field	Main counts	173513	94353
	Reference counts	27364	26338
Relative error of calculated σ		1.6%	2.6%

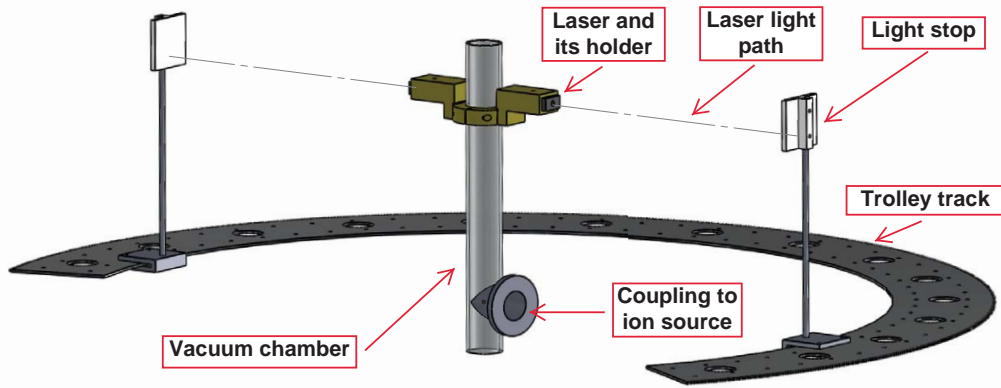


Figure 2.13 – Simplified CAD model of the first manual centering of the track with respect to the vacuum chamber. The golden piece is the adapter of the lasers to the vacuum chamber, which is the cylinder is the center. The dashed lines represent the laser light paths. The white flat pieces are light stops.

2.3.4 Alignment of the setup

In order to capture the correct energy, the centering and levelling of the track with respect to the point of emission of the neutrons should be as exact as possible. A first manual centering with laser distance sensors was performed, as described in Figure 2.13. The cylindrical vertical vacuum chamber was taken as reference and the distance from the chamber to various reference points on the track was measured. The position of the track was adapted accordingly, without forgetting the intrinsic eccentricity of the true center corresponding to the DD fusion point: it happens at the surface of the target, therefore it is shifted towards the 180° direction by a distance equal to half the diameter of the target.

A finer alignment step was subsequently implemented. It is inspired from Edge Spread Function (ESF) measurements previously realized at PSI [2]. In this case, pieces of aluminium of 10 mm thickness were progressively stacked to block the field of the view of the neutron detector, as illustrated in Figure 2.14a. The blocks can be stacked parallel to the basis plane³ to check the levelling of the track, i.e. if the track is not tilted with respect to this plane. They can also be stacked perpendicular to the same plane to check if the track is correctly centered with the DD fusion point. Each time the field of view is blocked a bit more with aluminum blocks, the detector counts less neutrons. The measured flux is then plotted versus the size of the obstacle as shown in Figure 2.14b. The operation was repeated from 0° to 180° every 45° around the generator. If the whole track was either tilted or had an eccentricity, these curves would not be aligned.

³Introduced in Section 1.7.2.

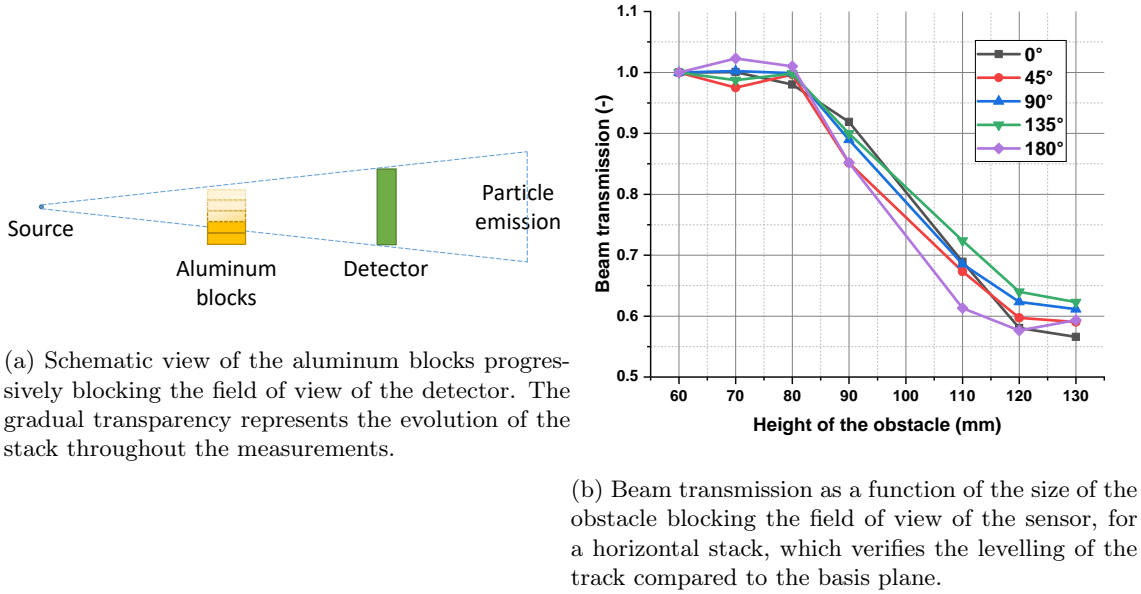


Figure 2.14 – Fine alignment method of the track with respect to the neutron generator.

2.3.5 Results and discussion with selected samples

In the available energy range, a well-known and prevalent cross-section structure was identified early on as a useful test case: it is the sharp drop in the total cross-section of oxygen at around 2.35 MeV. It is rather symmetrical as the cross-section sits at about 1 b at 2.2 and 2.5 MeV, but is only one tenth of that at 2.35 MeV. Oxygen is difficult to isolate under a high-density solid stable form. Instead, three compound samples were selected so that the combined elements do not disturb the oxygen dip: solid alumina - Al_2O_3 , solid magnesia - MgO , and deionized liquid water - H_2O . The results are shown respectively in Figures 2.15a, 2.15b, and 2.15c. The three deuterium implantation models are presented along with the experimental data. The deuteron impact vector is assumed to be either aligned with the forward 0° direction, or with a realistic angular spread. Both implantation and deuteron impact vector models were discussed in Section 2.1.2.2 and 2.1.2.3, respectively.

In order to efficiently compare the models, a version of the symmetric mean absolute percentage error (SMAPE) [48], defined in Equation 2.7, was computed for each of the three samples (Al_2O_3 , H_2O , MgO) and each of five physical models (“Dirac”, “uniform”, “uniform” with realistic deuteron angle, “round-peak”, “round-peak” with realistic deuteron angle). In Equation 2.7, p_i is the modelled value while a_i represents the experimentally measured value. It is brought to the attention of the reader that $\sum_{i=1}^m$ notation indicates a sum over the different m measurements, and should not be confused with the macroscopic cross-section. The bar graphs in Figure 2.16a and 2.16b summarize the SMAPE values according to a sample and a physical model grouping respectively. It can be seen that both thick-target deuterium implantation models (“uniform” or “round-peak”) yield better results than the thin-target (“Dirac”) approximation. Only small differences are visible between the two thick-target models. Finally, a realistic deuteron impact vector angle always brings an improved agreement. Because of the overall best agreement, for all the results showed next in this document, the **“uniform” deuterium implantation coupled to a realistic deuteron impact vector angle distribution is taken as the reference model** to be compared to the

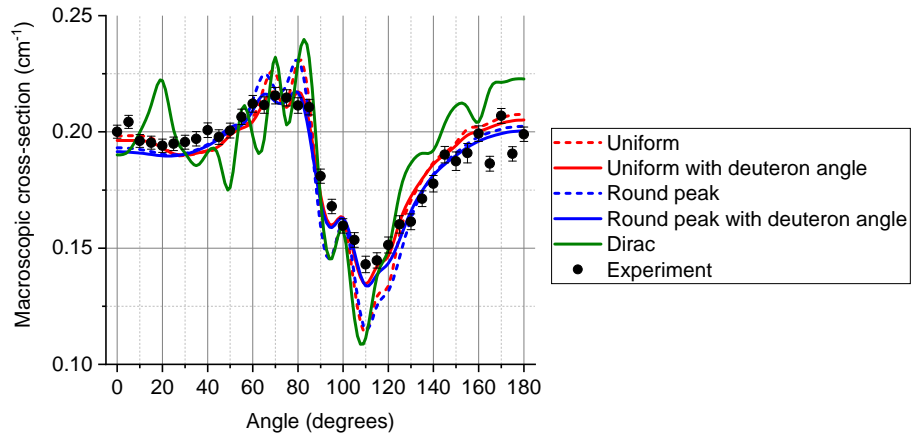
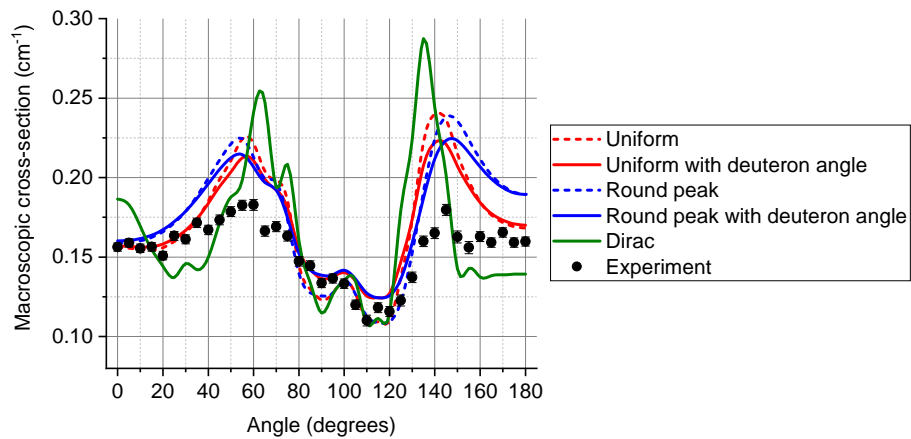
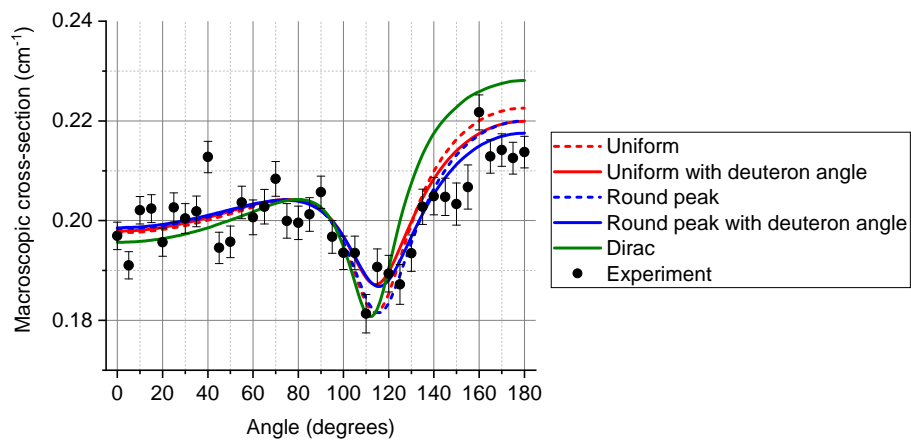
(a) Alumina - Al_2O_3 .(b) Magnesia - MgO .(c) Deionized water - H_2O .

Figure 2.15 – Macroscopic cross-section of alumina, magnesia, and deionized liquid water for a deuteron beam of 80 keV, compared to models without and with realistic deuteron angle distribution.

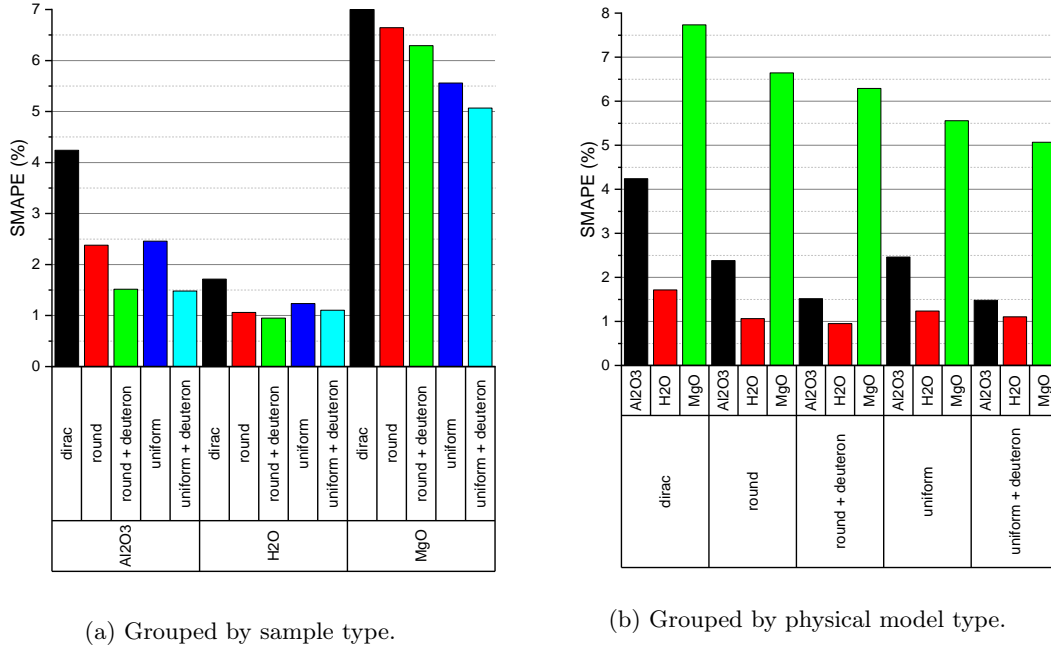


Figure 2.16 – SMAPE comparison of the experimental macroscopic cross-section and five different physical models.

experimental results.

$$SMAPE = \frac{100}{m} \cdot \sum_{i=1}^m \left(\frac{|p_i - a_i|}{|p_i| + |a_i|} \right) \quad (2.7)$$

Overall, the agreement with the models was very encouraging: this was a clear proof a principle of the energy-selective capability of the apparatus built around the source. It was particularly remarkable that the smaller variations of the water cross-section - in Figure 2.15c - were still captured by the measurement.

The deviations that are still visible - for example the general over-prediction of the macroscopic cross-section for the MgO sample - do not necessarily indicate that the experimental data are wrong. It should be noted that the custom models still carry assumptions that could not be entirely validated as it was discussed at length in Section 2.1. The manufacturer specifications concerning the purity of the sample can also be a source of error, effect that will be further studied in Section 2.5. Last but not least, the sample simulation required microscopic cross-section data as an input. It was taken from reliable sources [30]. However, they have their own degree of uncertainty that will be detailed separately in Section 2.3.6 to follow.

2.3.6 Limitations of reference cross-section data

The microscopic cross-section data σ were used twice until now in this study. First, as an input into the linear system Equations 1.4. Second, to help predict the sample macroscopic cross-section in the feasibility study in Section 2.3.5. In both cases, these input data are critical and uncertainties will have non-negligible repercussions on the results.

The international databases contain two kinds of microscopic cross-section data: the experimental ones, and the evaluated ones which are a model trying to fit best the experimental results and the most up-to-date physics models. All the data presented in this section were extracted from [30].

It appears that all experimental data come with their own uncertainties and that even for critical nuclides such as carbon, different sets can show large discrepancies between each other, as depicted in Figure 2.17. The latest evaluated data - depicted by the continuous plot - clearly do not agree with the most recent experimental datasets.

For some more exotic nuclides - for example Arsenic-75 shown on Figure 2.18 - the data can be simply non- or only partially existent in the MeV range. From this plot, it cannot be deduced that the cross-section is only flat in the sub-2.2 MeV region: the most recent experimental data from 1971 seem to have been used as basis for the evaluated data but it does not have any data point below 2.25 MeV. The only other dataset available from 1956 has some points in the sub-2.2 MeV region, but displays an amplitude which is roughly 15% higher. Consequently, it is difficult to select an absolute reference among all these data. Like in the case of the neutron spectrum, there are some persistent uncertainties. Section 2.4, following, will propose a solution to circumvent both the spectrum and cross-section uncertainties.

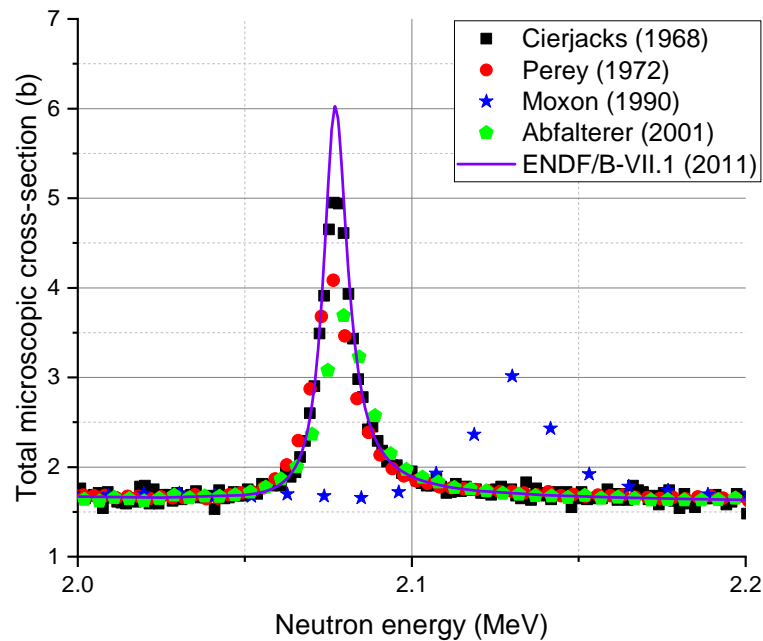


Figure 2.17 – Comparison of datasets for the microscopic cross-section of natural carbon. The scatter plots correspond to the experimental sets, while the continuous plot is an evaluated one [5].

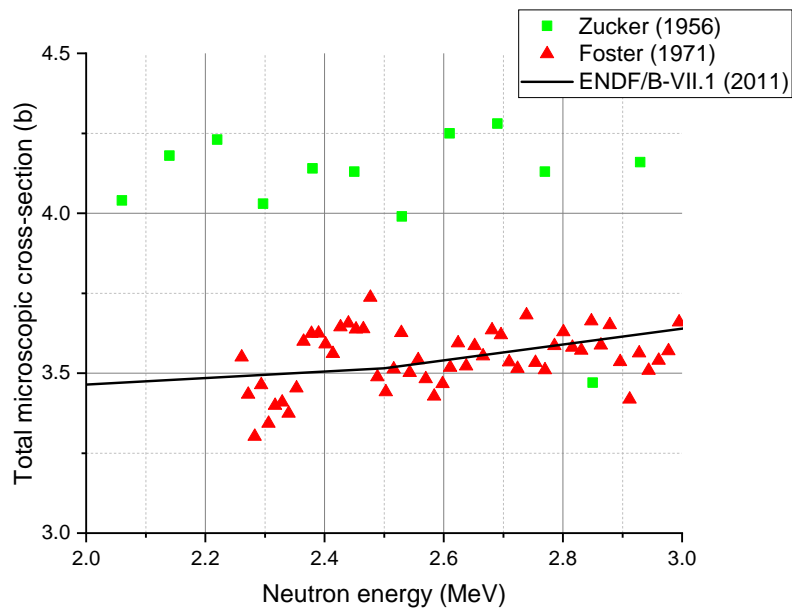


Figure 2.18 – Comparison of datasets for the microscopic cross-section of Arsenic-75. The scatter plots correspond to the experimental sets, while the continuous plot is an evaluated one [5].

2.4 Calibration with reference samples

2.4.1 Objectives of the calibration

The objective of this study is to be able to solve the linear system of Equations 1.4 so the elemental content of a studied sample can be characterized. On top of the sample thickness τ , the beam intensity without I_{emp} and with the sample I_{τ} covering entirely the field of view of the neutron detectors, the last input needed is the spectrum-averaged microscopic cross-section data $\bar{\sigma}$. This variable needs in turn the neutron spectrum $\Phi(E)$ and the discrete microscopic cross-section data σ_i to be computed according to Equation 1.9. As shown in Sections 2.2 and 2.3.6, these two variables are burdened with significant uncertainties.

These uncertainties would impede the quality and the robustness of the problem solving. To bypass them, another method will be employed. A list of **well-known reference samples** will be established and their elemental content determined in advance, without the help of attenuation measurements. Equation 1.5 will then be taken from another perspective: now that the elemental concentration \bar{N} is known along with the attenuation measurements $\bar{\Sigma}_{\text{meas}}$, the **spectrum-averaged microscopic cross-section** $\bar{\sigma}$ can be computed. The newly computed data are setup-specific and not precisely valid for other experimental setups, but it does not require any prior knowledge about neutron spectrum and discrete microscopic cross-section. When each nuclide has been properly isolated, the whole database will constitute a solid foundation to solve the standard problem of elemental content characterization in an unknown sample.

2.4.2 Identifying the elements of interest

A viable linear system such as in Equations 1.5 can only be solved adequately if the cross-section data of the nuclides under investigation show strong enough energy- and element-specific trends. The first step of the calibration was hence to determine the nuclides featuring obvious cross-section variations in the energy range of the generator.

The elements with an atomic number (Z) between 1 (hydrogen) and 20 (calcium) present such a behavior. For higher- Z materials, the cross-section features tend to be small and would fall within the uncertainty range of the experimental data. They would be difficult to detect. This is only a general observation, and some heavier nuclides do show some features while some lighter nuclides like hydrogen have a very smooth trend. For the sake of simplicity, this work will focus nevertheless only on the range $Z = [1..20]$. On top of that, the special cases of steel 316L, arsenic, and bromine will be considered. Steel 316L because it is a fairly common structural material. The two other elements are relevant for homeland security applications because they occupy a special place in the realm of chemical weapons: arsenic is found in several blister agents - such as Lewisite - while liquid bromine and other variants can be used in suffocating and irritating products [49].

The evaluated data library ENDF B-VII.1 [5] was used to carry out this investigation. It has its own limits as it was shown in Section 2.3.6. Nevertheless, it is rather reliable and provided enough information for this preliminary research step.

2.4.3 Sample preparation

After the cross-section investigation, the second step consisted of selecting homogeneous samples containing, where possible, exclusively one nuclide, in a stable form, and with a reasonable density, e.g. liquid or solid. Typical gas densities would imply very weak attenuation that would be hard to detect. The elemental content of the samples needed to be well-characterized prior to the measurement, so that the averaged cross-section data could be computed with minimum uncertainty.

For the most reactive species, such as oxygen, it is rather difficult to isolate the element. Instead, a two-fold procedure was followed: two carefully selected distinct samples were measured and, by subtraction, the data corresponding to the nuclide of interest could be isolated. In the case of oxygen, a pure aluminum sample, Al, and a alumina sample, Al_2O_3 , could be measured for example. By subtracting twice the pure aluminum cross-section from the alumina one, only three times the oxygen cross-section is left. The complete list of the selected samples is available in Table 2.3.

Although great care was put in the sample selection to find the best fit in terms of content, stability and associated risks, some samples represented non-negligible hazards and/or were available only under a form requiring containment (powder, evaporating liquid, hygroscopic material). A custom sealed stainless steel container was therefore developed to house individually most of the samples. The picture of Figure 2.19 shows the final product. Thanks to its standardized dimensions - $40 \times 50 \times 60 \text{ mm}^3$, with 1.5 mm walls - and its tightness, switching between samples proved to be very easy. The column "Container" of Table 2.3 summarizes the receptacle used for each sample, "SS" referring to the previously described stainless steel container. The container "LA" is an aluminium open-ended vessel that was specially designed for water, with dimensions of $200 \times 100 \times 50 \text{ mm}^3$ and walls of 1.5 mm. The rest of the samples did not need any container and are labelled accordingly. The dimensions and squareness of the containers were thoroughly checked and found not to exceed about 1% of the sample depth, therefore having a negligible effect on the beam attenuation.

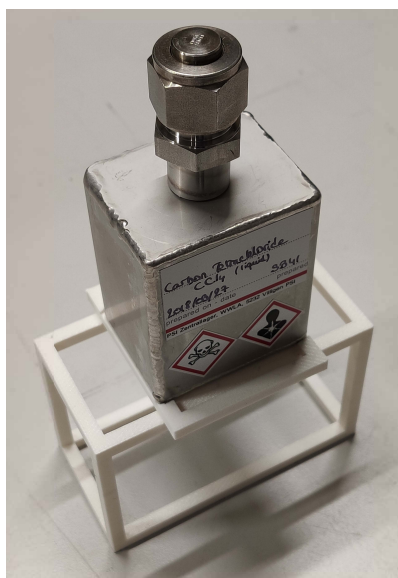


Figure 2.19 – Photograph of the sealed stainless steel container used during the calibration.

Table 2.3 – List of the investigated samples for the calibration.

Sample	State	Dimensions (height × width × depth, mm)	Number density (10^{22} cm^{-3})	Container	Correction shift (cm^{-1})	ζ
Alumina - Al_2O_3	Solid	$150 \times 100 \times 50$	2.16	None	$5.6 \cdot 10^{-3}$	
Aluminium - Al	Solid	$150 \times 100 \times 50$	6.09	None	$8.3 \cdot 10^{-3}$	
Aluminium Nitride - AlN	Powder	$59.8 \times 51.7 \times 40.3$	2.21	SS	$1.8 \cdot 10^{-2}$	
Arsenic - As	Powder	$60 \times 51.7 \times 40.4$	2.98	SS	$1.1 \cdot 10^{-2}$	
Beryllium oxide - BeO	Solid	$60 \times 52.9 \times 42$	6.89	SS	$9.1 \cdot 10^{-2}$	
Boron - B	Powder	$60.3 \times 50.9 \times 40.8$	5.41	SS	$2.4 \cdot 10^{-2}$	
Boron nitride - BN	Powder	$59.8 \times 51.3 \times 40.4$	1.69	SS	$1.5 \cdot 10^{-2}$	
Calcium - Ca	Powder	$59.8 \times 51.8 \times 40.2$	1.07	SS	$2.6 \cdot 10^{-3}$	
Carbon tetrachloride - CCl_4	Liquid	$60.1 \times 51.8 \times 40.1$	0.63	SS	$1.6 \cdot 10^{-2}$	
Graphite - C	Solid	$152 \times 101.5 \times 50.5$	8.68	None	$9.5 \cdot 10^{-3}$	
Hexabromobenzene - C_6Br_6	Powder	$60.1 \times 51.7 \times 40.1$	0.23	SS	$9.4 \cdot 10^{-3}$	
High-density polyethylene - C_2H_4	Solid	$150 \times 100 \times 50$	2.07	None	$3.9 \cdot 10^{-2}$	
Lithium Chloride - LiCl	Powder	$60.1 \times 50.8 \times 40.8$	1.80	SS	$1.9 \cdot 10^{-2}$	
Magnesia - MgO	Solid	$121 \times 70.4 \times 50.5$	4.77	None	$2.5 \cdot 10^{-2}$	
Magnesium - Mg	Powder	$60.2 \times 51.7 \times 40.3$	2.14	SS	$1.0 \cdot 10^{-2}$	
Phosphorus - P	Powder	$60 \times 51.2 \times 40.8$	2.35	SS	$8.0 \cdot 10^{-3}$	
Polytetrafluorethylene - C_2F_4	Solid	$150 \times 100 \times 54$	1.57	None	$1.7 \cdot 10^{-2}$	
Silicon - Si	Powder	$59.7 \times 50.4 \times 40.9$	2.80	SS	$9.2 \cdot 10^{-3}$	
Sodium Chloride - NaCl	Powder	$59.8 \times 50.7 \times 41$	1.49	SS	$1.6 \cdot 10^{-2}$	
Steel 316L	Solid	$146 \times 101 \times 24.2$	8.87	None	$2.9 \cdot 10^{-3}$	
Sulfur - S	Powder	$60.4 \times 51.8 \times 40.1$	1.92	SS	$5.6 \cdot 10^{-3}$	
Water - H_2O	Liquid	$200 \times 100 \times 50$	3.34	LA	$4.7 \cdot 10^{-3}$	

2.5 Results and discussion of the calibration

2.5.1 Macroscopic cross-section

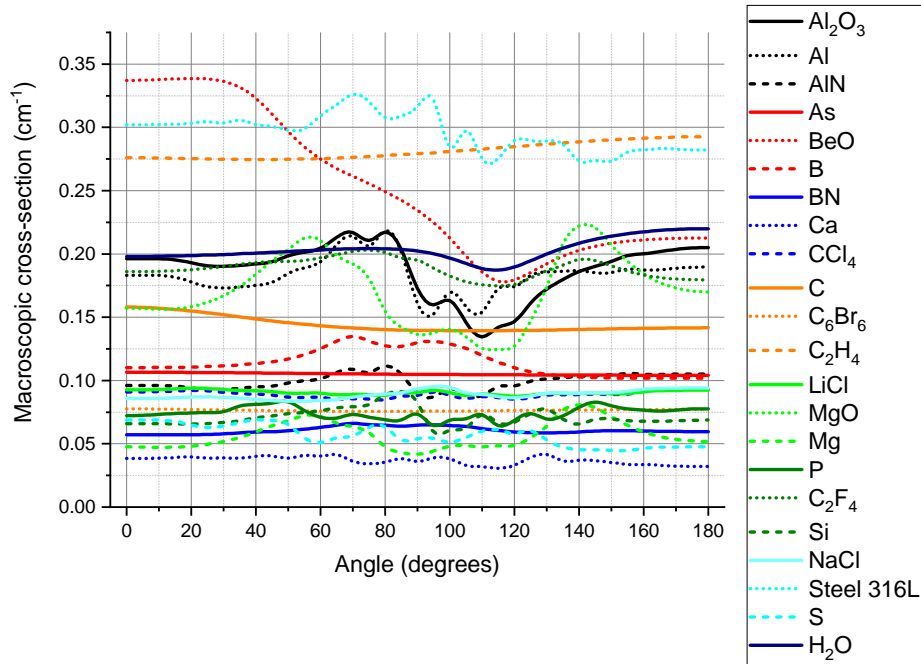


Figure 2.20 – Theoretical spectrum-averaged macroscopic cross-sections of all the samples studied, according to the “uniform” model, coupled to a realistic deuteron impact vector.

The experimentally-determined macroscopic cross-sections of all twenty-two samples of Table 2.3 are shown from Figure 2.21a to 2.24d. Figure 2.20 gives an overview of the situation, reproducing all the modelled sample cross-section data in an unique figure. The attentive reader will realize that the amplitude of the macroscopic cross-section can vary significantly from one sample to the other, and that the scale of each individual figure (Figure 2.21a to 2.24d) was adapted accordingly. For small-amplitude cases, it may give the impression of disproportionate uncertainty bars, but the ordinate scale should be carefully read.

It is visible that the *uncorrected* experimental results are not exactly aligned with the reference models. This discrepancy might be explained by the different assumptions that burden these models: the uncertainties about the neutron spectrum and the discrete cross-section data were emphasized in the previous sections. But there is also a residual doubt about the exact purity of the reference samples. They were carefully selected at the highest quality reasonably achievable, but they can never be completely pure. A small mix of random elements is likely to have a rather flat total cross-section overall, because all the structures will be more or less cancelling each other. Therefore it will only add a constant shift to the data throughout the angular range. A simple correction is accordingly applied, in the form of a constant shift ζ that is applied to the raw data so that $X_{\text{corr}} = X_{\text{uncorr}} + \zeta$. An optimization study was carried out in order to find the most suitable shift, i.e. until the *corrected* data were fitting best the models in the least-squares sense. The corrected data are plotted on the same figures to highlight the improvement. The correction factors are given in the last column of Table 2.3.

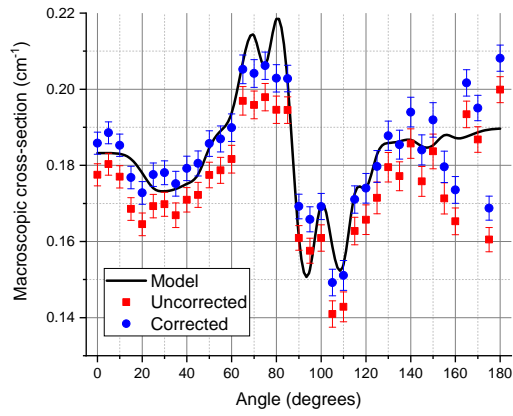
To illustrate further the issue of purity, a sample of aluminum nitride (AlN) with striking discrepancies is presented in Figure 2.25a. This is nominally a 98% (by weight) pure sample, but the nature of the impurities is not given. A little *Gedankenexperiment* detailed in Appendix D shows that if the impurity is only hydrogen, it could represent up to 29.5% of the atoms present in the sample. Fortunately, it was possible to obtain another AlN sample with a visibly improved purity, previously shown in Figure 2.21c and reproduced again in Figure 2.25b for an easy comparison.

In order to have a simple figure of merit of the goodness of fit between experimental and modelled macroscopic cross-section data, the SMAPE, introduced in Equation 2.7 was used here again. The SMAPE can be computed in two ways: either it assesses the error at a given trolley position (for a given neutron spectrum) across all the measured samples; but it can also quantify the error for a given sample, across all the trolley positions.

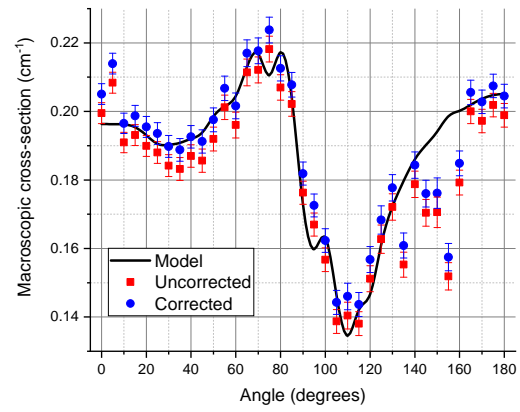
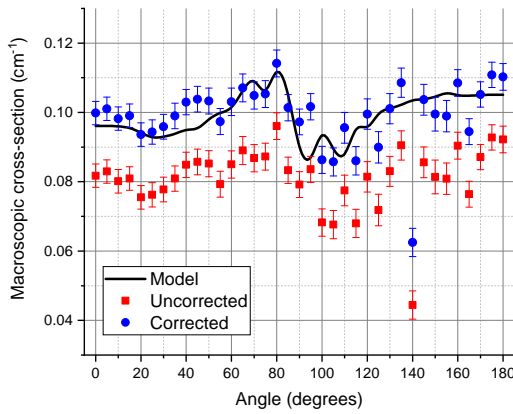
The study will start first with the SMAPE at given trolley positions, shown in Figure 2.26. The improvement due to the shift correction appears clearly. However, for most samples, the experimental data in range extending beyond 90° presents an increasing divergence from the model. It is supposed that in that region, in spite of all the precautions taken, the measurement apparatus is irretrievably affected by the neutron source and the results cannot be completely be trusted. There, the trolley is indeed closest to the RF antenna - as shown on Figure 2.27 - and the strong stray fields might have an adverse effect on the electronics. It was unfortunately not possible within the frame of this study to produce neutrons with the generator without the RF source. Using a second source such as Cf-252, which does not require external power, and switching the RF field on or off could allow to test this hypothesis but it was not possible to implement it in the frame of this work. The Cf-252 source itself would not allow to make energy-selective measurements since its output is an unique broad fission spectrum. A parallel doctoral study is focused on the replacement of the RF power source by a new one based on microwaves, but it has not yet been completed. Based on a precisely mounted series of waveguides, that can also play the role of a tight Faraday cage, it is supposed to overall reduce the interference.

The RF antenna should only marginally affect the neutron spectrum itself. Any foreign material, such as piping, antenna, etc. which is in the field of view of the detectors is expected to mainly induce scattering. Down-scattering is the only relevant type of scattering in the energy region of interest and should generally have an opposite effect that the one which can be seen. For example, on Figure 2.21b, the macroscopic cross-section is significantly under-predicted. Like the model shows for larger angle above 160° - where the energy decreases further according to the kinetic of the DD fusion - the cross-section tends to be higher at lower energies. Through down-scattering, an over-prediction of the cross-section would then be expected, but is clearly not observable.

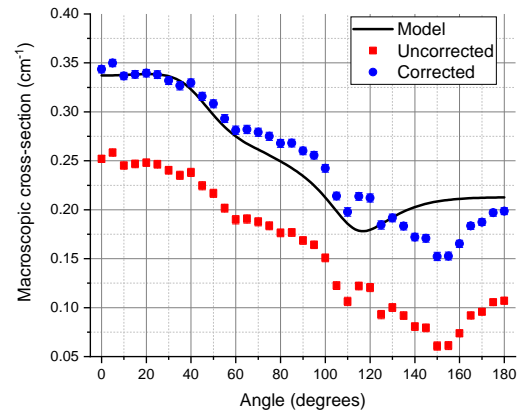
The SMAPE was first computed for the entire angular range (0° to 180°). The range beyond 90° is obviously affected by a larger disturbance of still unknown nature. It was therefore decided to analyse the SMAPE for the first quadrant (0° to 90°) separately as an additional criterion for the match of the measuring results with the reference data. Table 2.4 summarizes the different SMAPE values obtained for both the corrected and uncorrected data and for both position sets. The improvement of the agreement between model and shift-corrected is again limpid. Checking the SMAPE values while giving a close look at the curve trends individually, the position set limited to the first quadrant gives a more meaningful figure of merit to sort the different samples out. The agreement was found to be good, especially for samples featuring large cross-section structures such as Al_2O_3 , Al, and BeO - respectively shown in Figures 2.21a, 2.21b, and 2.21d. Samples with relatively smaller cross-section structures still show a general good agreement: among them AlN, B, C, C_2F_4 , H_2O , and Steel 316L, respectively shown in Figures 2.21c, 2.22d, 2.21e, 2.21f, 2.22b, and 2.24d. Samples with overall smaller macroscopic cross-sections (mainly because their respective densities are low, since they are in powder or liquid form) like As, Ca, CCl_4 , C_6Br_6 , LiCl, Mg, NaCl, P, S, and Si, show a partial agreement, as illustrated in Figures 2.22c, 2.23a, 2.23b, 2.21e, 2.22f, 2.23c, 2.23f, 2.24a, 2.24b, and 2.24c. Two samples, C_2H_4 and MgO in Figures 2.22a and



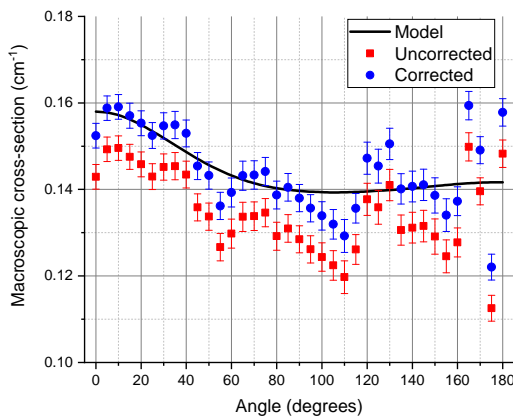
(a) Aluminium - Al.

(b) Alumina - Al₂O₃.

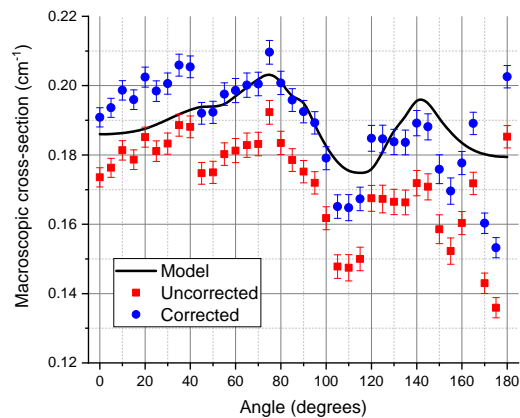
(c) Aluminium Nitride - AlN.

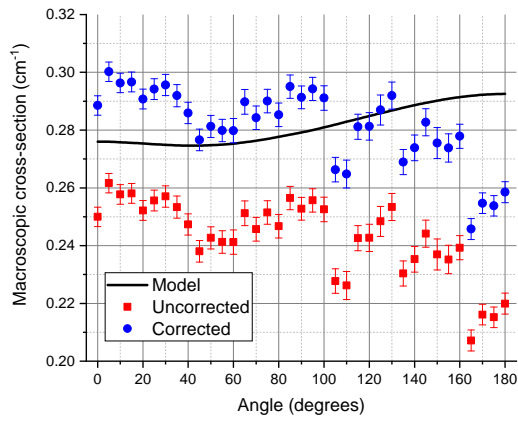
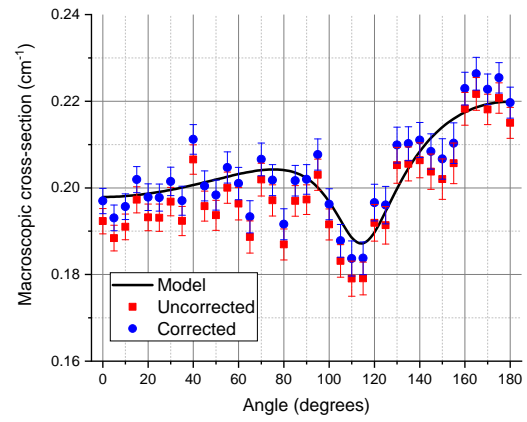
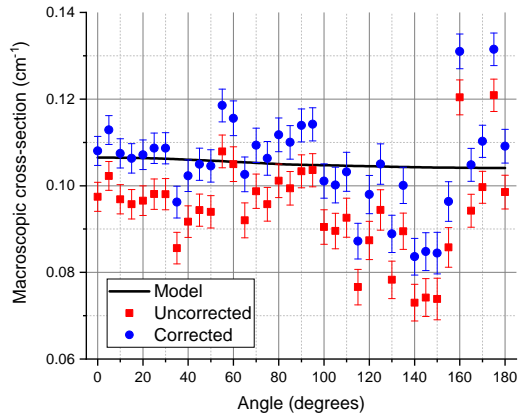


(d) Beryllia - BeO.

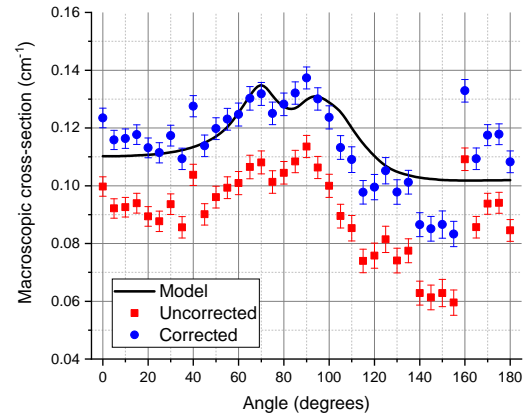


(e) Graphite - C.

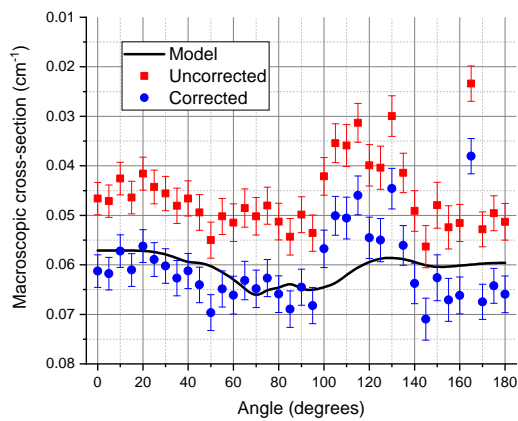
(f) Polytetrafluoroethylene - C₂F₄.Figure 2.21 – Macroscopic cross-section of Al, Al₂O₃, AlN, BeO, C, and C₂F₄. Deuteron beam of 80 keV.

(a) High-density polyethylene - C_2H_4 .(b) Deionized water - H_2O .

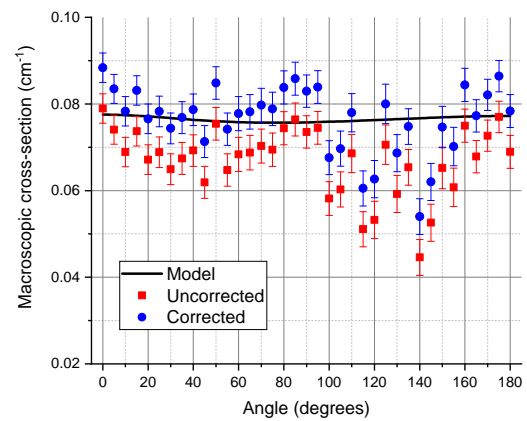
(c) Arsenic - As.

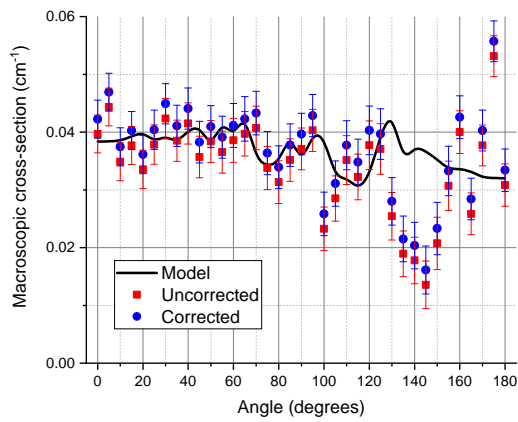


(d) Boron - B.

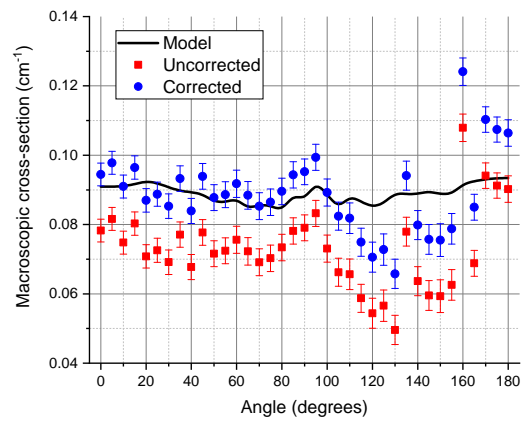
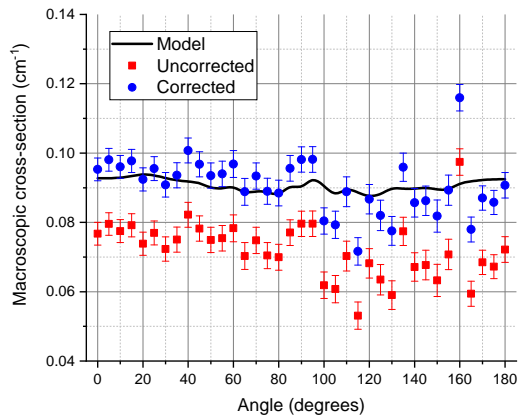


(e) Boron Nitride - BN.

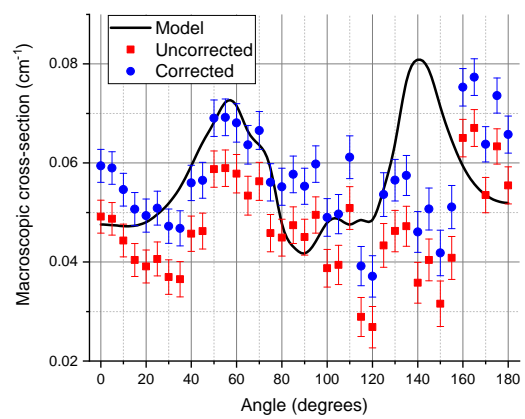
(f) Hexabromobenzene - C_6Br_6 .Figure 2.22 – Macroscopic cross-section of C_2H_4 , H_2O , As, B, BN, and C_6Br_6 . Deuteron beam of 80 keV.



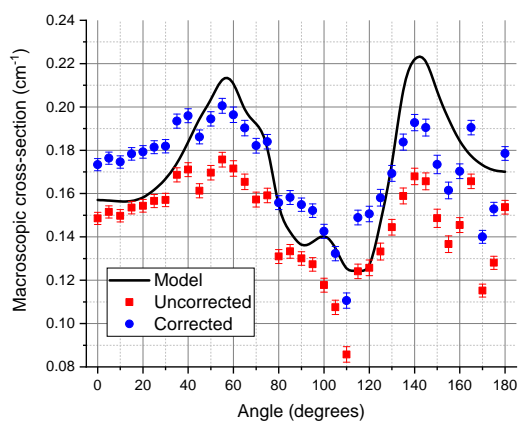
(a) Calcium - Ca.

(b) Carbon Tetrachloride - CCl₄.

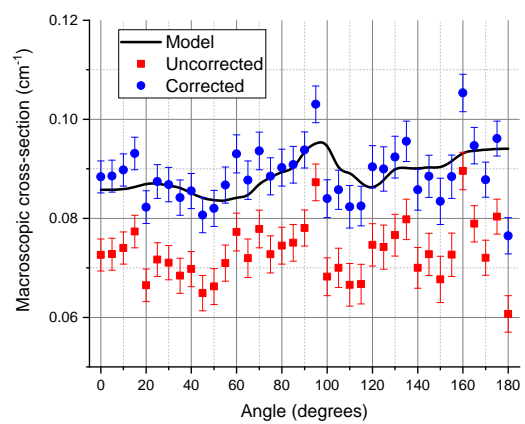
(c) Lithium Chloride - LiCl.



(d) Magnesium - Mg.

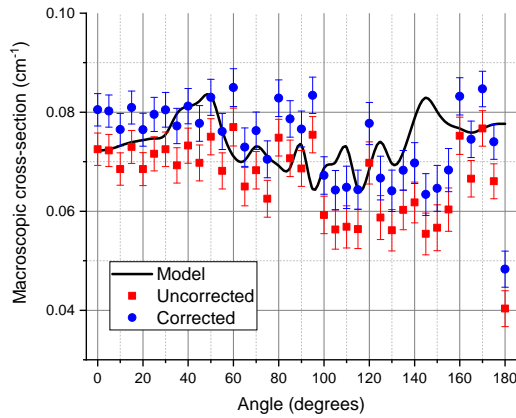


(e) Magnesium Oxide - MgO.

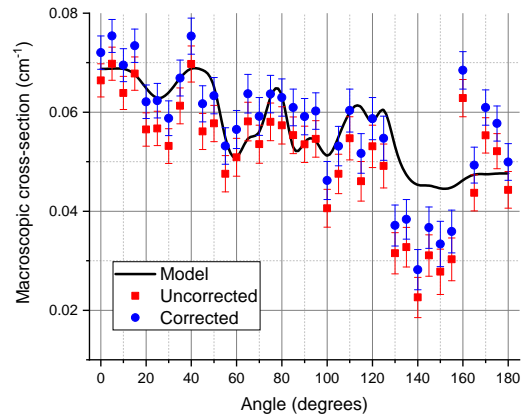


(f) Sodium Chloride - NaCl.

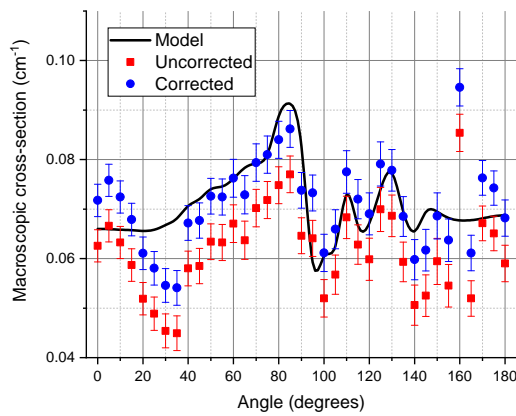
Figure 2.23 – Macroscopic cross-section of Ca, CCl₄, LiCl, Mg, MgO, and NaCl. Deuteron beam of 80 keV.



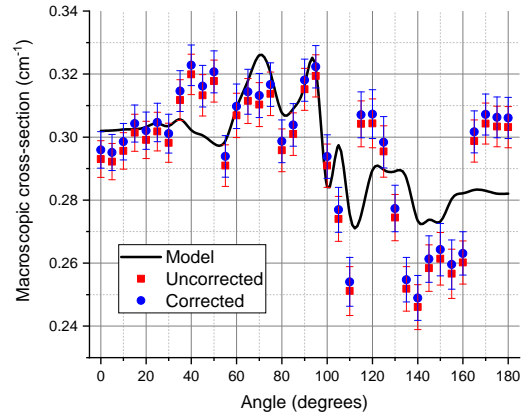
(a) Phosphorus - P.



(b) Sulfur - S.

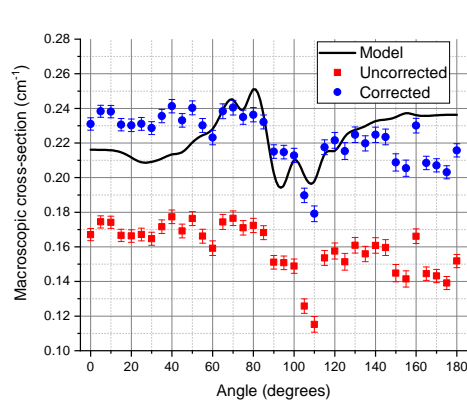


(c) Silicon - Si.

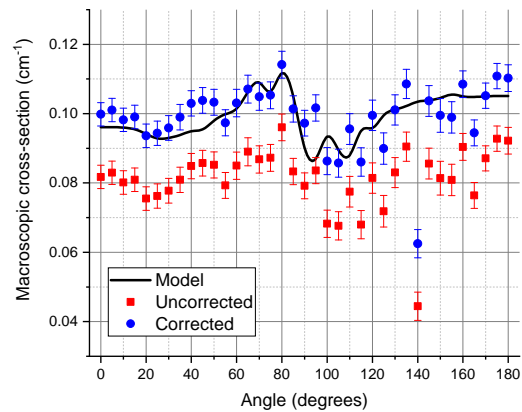


(d) Steel 361L.

Figure 2.24 – Macroscopic cross-section of P, S, Si, and Steel 316L. Deuteron beam of 80 keV.



(a) First sample with a declared purity of 98%.



(b) Second sample with a visibly higher purity.

Figure 2.25 – Two Aluminum Nitride - AlN samples with different qualities. Deuteron beam of 80 keV.

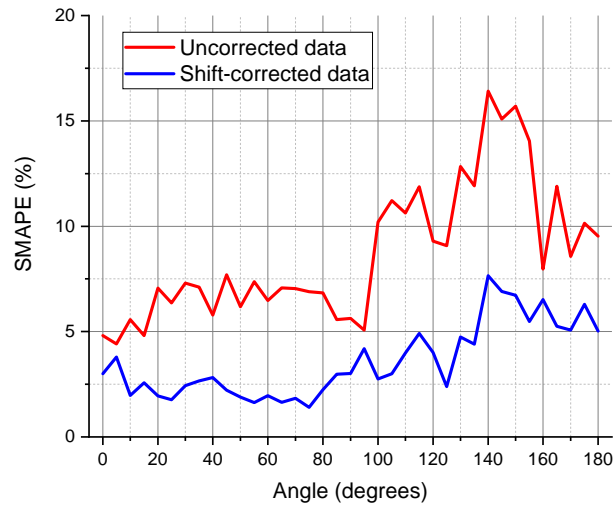


Figure 2.26 – SMAPE at given trolley positions, across all available samples.

2.23e, show rather large discrepancies that could not be resolved.

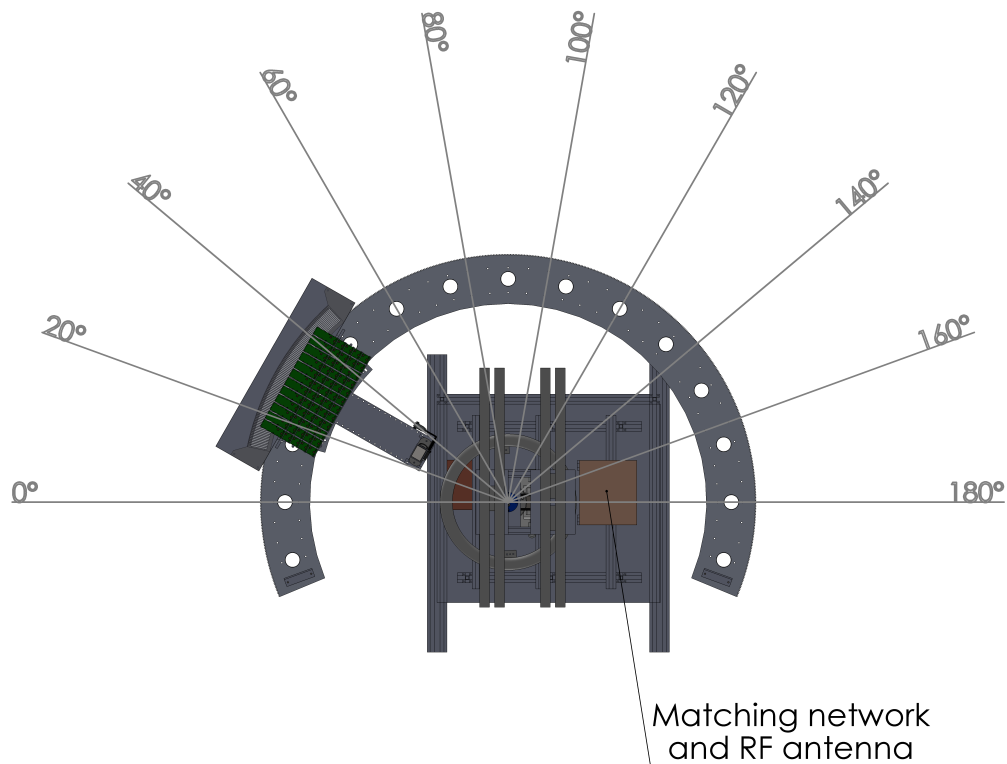


Figure 2.27 – Computer model of the measurement setup around the generator. Several emission angles are shown to highlight the growing proximity of the strong RF source beyond 90°.

Table 2.4 – SMAPE of the macroscopic cross-section data of the investigated samples.

Sample	SMAPE uncor- rected 0-180°(%)	SMAPE corrected 0-180°(%)	SMAPE uncor- rected 0-90°(%)	SMAPE corrected 0-90°(%)
Alumina - Al ₂ O ₃	2.23	1.89	1.34	1.12
Aluminium - Al	2.63	1.55	2.29	1.13
Aluminium Nitride - AlN	10.23	2.98	8.61	1.84
Arsenic - As	6.47	3.62	4.22	2.01
Beryllium oxide - BeO	24.79	4.25	16.05	1.80
Boron - B	12.20	3.73	9.52	1.95
Boron nitride - BN	14.28	4.70	11.42	2.36
Calcium - Ca	9.16	8.50	3.45	3.57
Carbon tetrachloride - CCl ₄	11.00	4.43	8.85	2.16
Graphite - C	3.78	1.69	3.41	0.87
Hexabromobenzene - C ₆ Br ₆	6.96	3.98	4.36	2.75
High-density polyethylene - C ₂ H ₄	7.41	2.72	4.83	2.33
Lithium Chloride - LiCl	11.84	3.08	9.17	1.94
Magnesia - MgO	7.67	4.76	5.07	4.01
Magnesium - Mg	12.54	8.98	8.94	5.52
Phosphorus - P	6.92	4.73	3.69	3.20
Polytetrafluorethylene - C ₂ F ₄	5.02	2.21	3.24	1.56
Silicon - Si	8.03	3.91	9.00	3.79
Sodium Chloride - NaCl	9.84	2.37	9.02	1.58
Steel 316L	2.31	2.17	1.33	1.12
Sulfur - S	8.08	5.90	3.82	3.11
Water - H ₂ O	1.48	1.03	1.70	0.90

These data could be further improved with longer measurements, giving better statistics and reduced uncertainties. The samples could also be more thoroughly characterized to identify potential impurities that might impact the effective sample cross-section. Within the scope of this study such chemical characterization was not feasible.

As a robustness check, it is possible to compute the SMAPE in a third way, i.e. across both all the angles and all the samples combined, in order to confirm the choice that was made in Section 2.3.5 about the reference model. The previous results encompassed only three samples (Al_2O_3 , MgO , and H_2O), but twenty-two can be used for this new calculation. Figure 2.28 outlines the results with both sample sets (counting three or twenty-two samples) for the shift-corrected results. The uncorrected results showed exactly the same tendencies and were omitted for the sake of conciseness. The tendencies are confirmed; the thick-target models (“uniform” and “round peak”) are very close to one another and seem to describe the reality better than the thin-target model (“Dirac”). A realistic distribution of the deuteron impact vector angle always improves the agreement in the results shown. The choice of the “uniform” deuterium implantation in the target with a realistic deuteron impact vector is therefore corroborated.

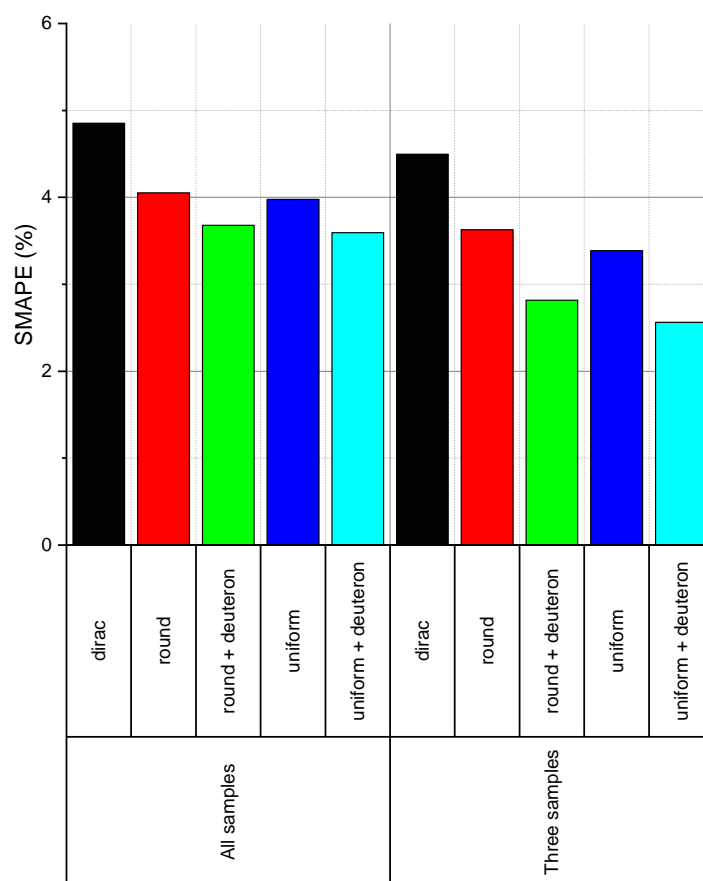


Figure 2.28 – SMAPE of the reference models, across samples and trolley positions. The first group “All samples” takes into account all twenty-two available samples. The group “Three samples” refer to the three samples (water, magnesia, and alumina) used for the proof of principle in Section 2.3.

2.5.2 Microscopic cross-section

The subtraction method - presented in Section 2.4.3 - was applied to the macroscopic cross-section data of Section 2.5.1 in order to isolate each of the nineteen elements of interest and to constitute the reference setup-specific microscopic cross-section database. The results are presented from Figure 2.30a to 2.33d. Figure 2.29 is also given beforehand for the reader to have an overview of all the cross-section data of the nuclides of interest. The same remark about the ordinate scale of the individual figures (from Figure 2.30a to 2.33d) and the appearance of the error bars remains valid as in the previous Section 2.5.1.

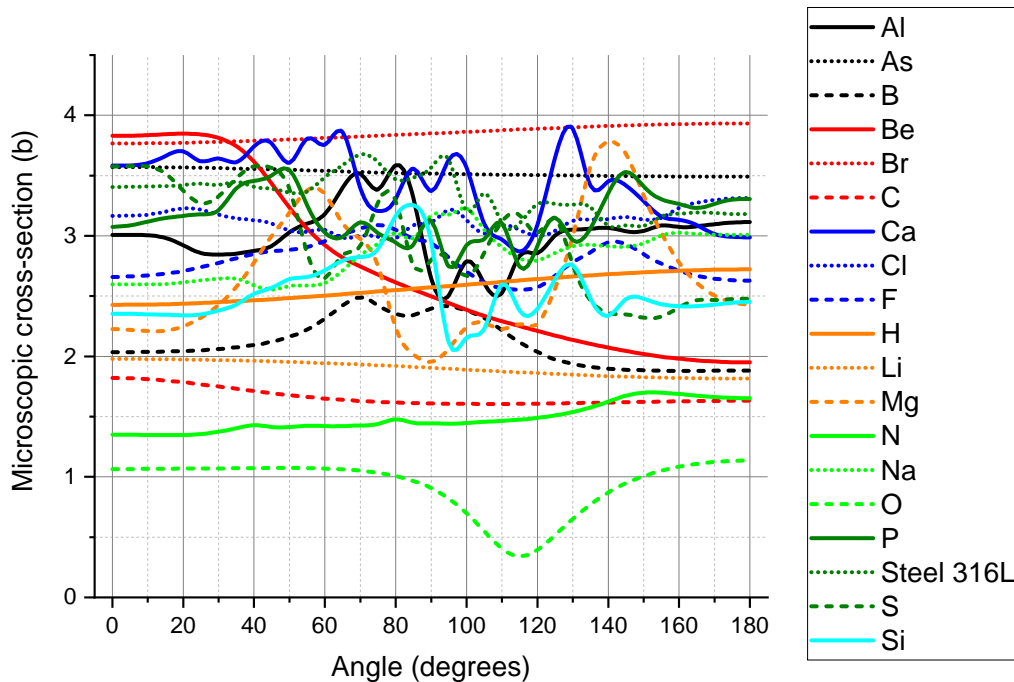
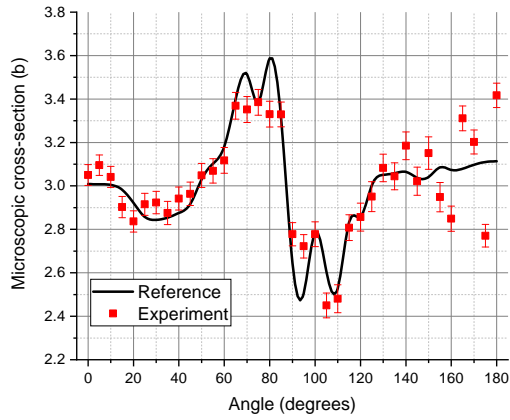


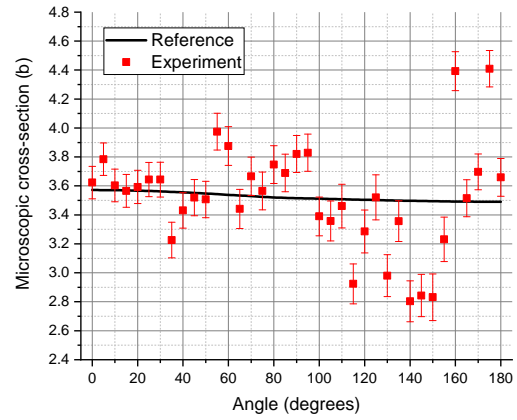
Figure 2.29 – Microscopic cross-sections of all the nuclides of interest studied, according to the “uniform” model, coupled to a realistic deuteron impact vector. Steel 316L is treated here as a pseudo-element because the material itself is of interest, as a commonly used structural material.

Since these results are exclusively using the macroscopic cross-section data from Section 2.5.1, it is not astounding to find the best microscopic cross-section data coming from samples with the best reference data. The SMAPE for each sample is recapitulated in Table 2.5. Like in Section 2.5.1, the SMAPE was computed for both positions sets, either the full 0° to 180° range, or only the first angle quadrant 0° to 90° , since beyond that point, the microscopic cross-section data seem affected by external phenomena not linked to pure attenuation of neutrons through matter. Here again, the first angle quadrant gives a more meaningful figure of merit to classify the different nuclides.

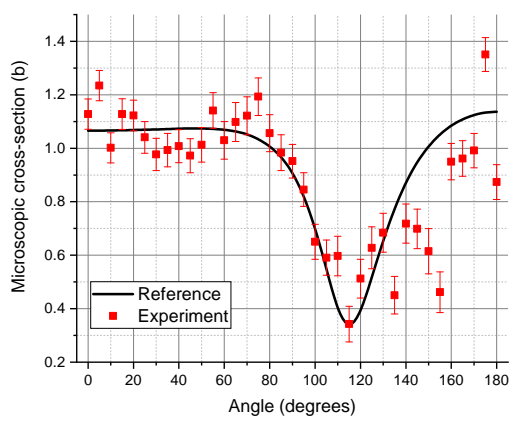
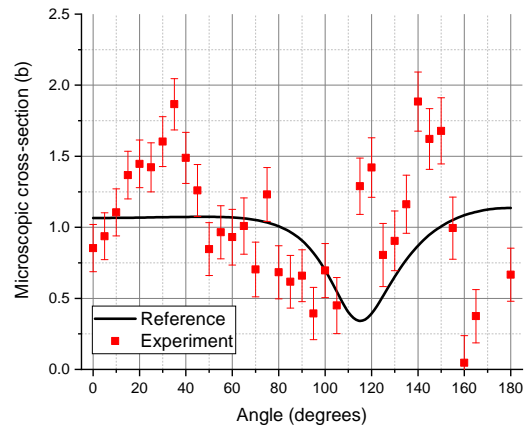
The main trends are very well captured for the following nuclides: Al, B, Be, and F shown in Figures 2.30a, 2.30e, 2.31a, 2.31d, respectively. The agreement is also good for nuclides such as C, Ca, Cl, Li, and Na - respectively in Figures 2.33d, 2.31b, 2.31c, 2.32a, and 2.32e. For Steel 316L, S, P, and Si, some trends are discernible in Figures 2.32f, 2.33b, 2.33c, and 2.33a, but a significant disagreement is still observable, notably for Si in the $20\text{--}40^\circ$ region. The results remain quite scattered for Mg in Figure 2.32b, which is not surprising since the results for the original



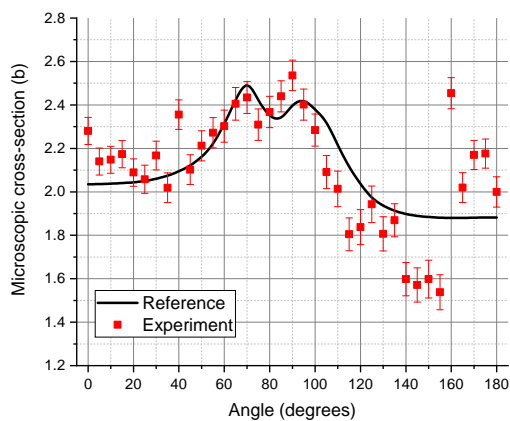
(a) Aluminium - Al from pure sample.



(b) Arsenic - As from pure sample.

(c) Oxygen - O from Al_2O_3 and Al.

(d) Oxygen - O from MgO and Mg.



(e) Boron - B from pure sample.

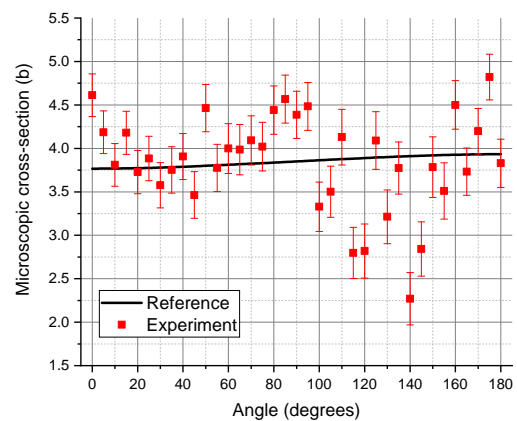
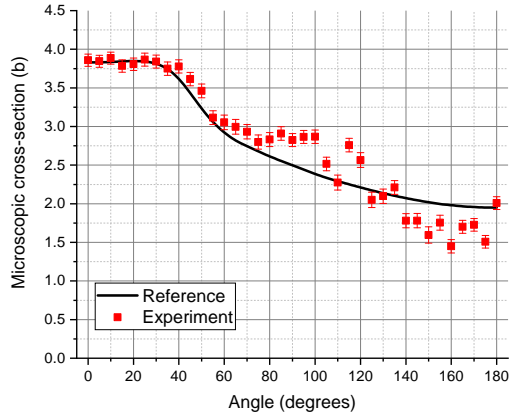
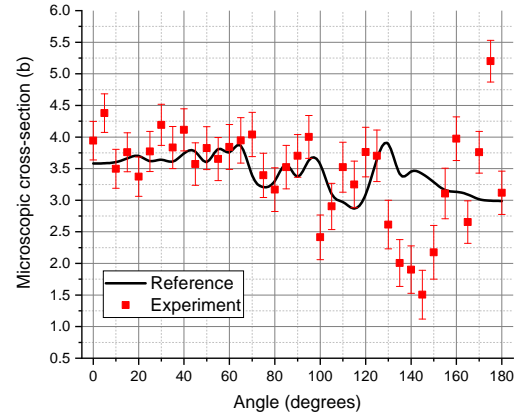
(f) Bromine - Br from C and C_6Br_6 .

Figure 2.30 – Microscopic cross-section of Al, As, O, B, and Br. Deuteron beam of 80 keV.

(a) Beryllium - Be from BeO, Al₂O₃, and Al.

(b) Calcium - Ca from pure sample.

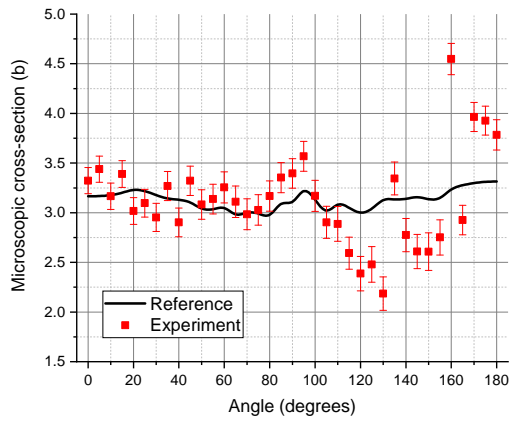
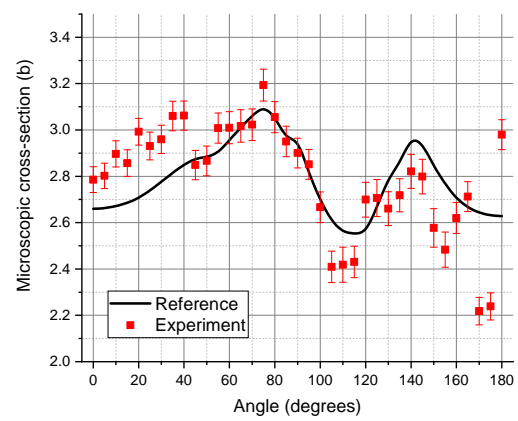
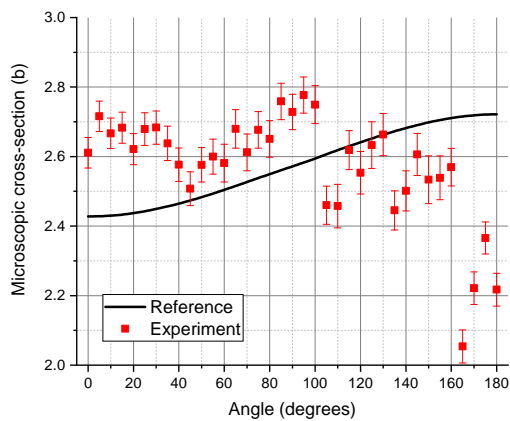
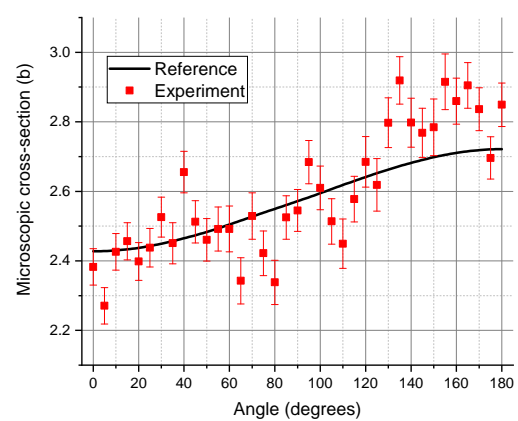
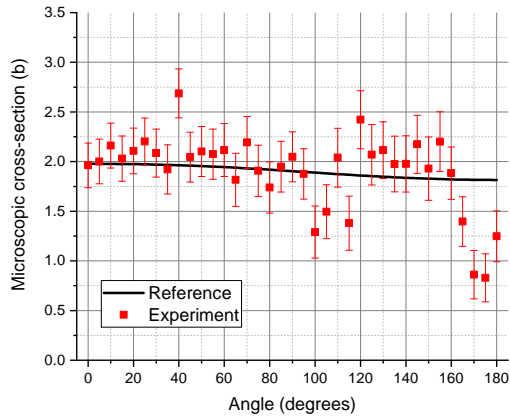
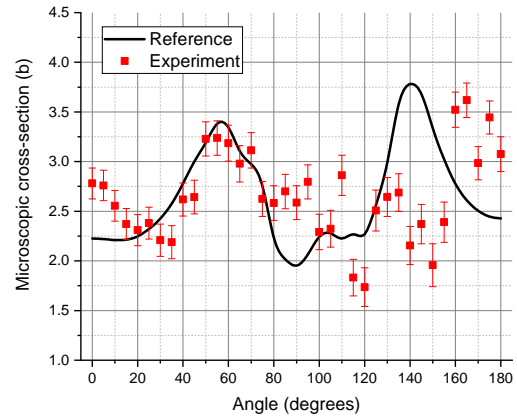
(c) Chlorine - Cl from CCl₄ and C.(d) Fluorine - F from C₂F₄ and C.(e) Hydrogen - H from C and C₂H₄.(f) Hydrogen - H from H₂O, Al, and Al₂O₃.

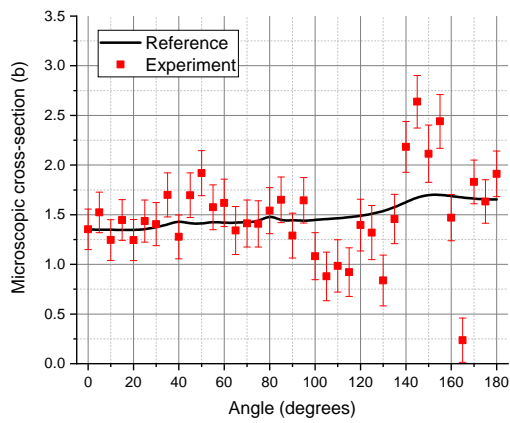
Figure 2.31 – Microscopic cross-section of Be, Ca, Cl, F, and H. Deuteron beam of 80 keV.



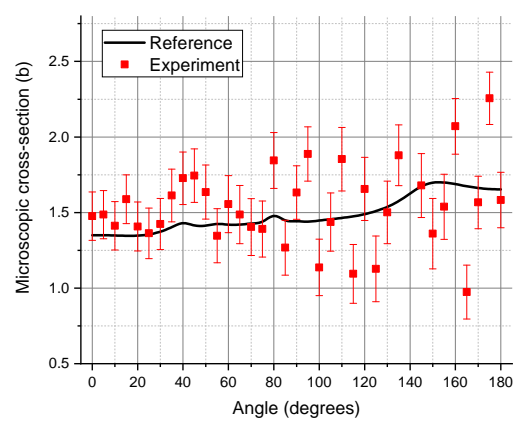
(a) Lithium - Li from LiCl, CCl₄, and C.



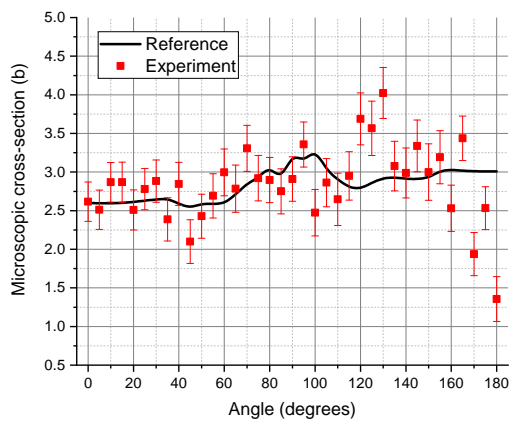
(b) Magnesium - Mg from pure sample.



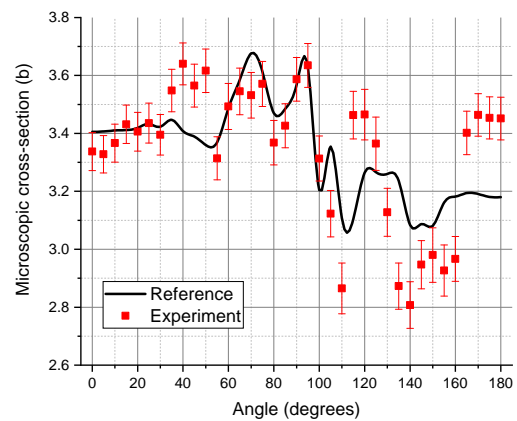
(c) Nitrogen - N from BN and B.



(d) Nitrogen - N from AlN and Al.

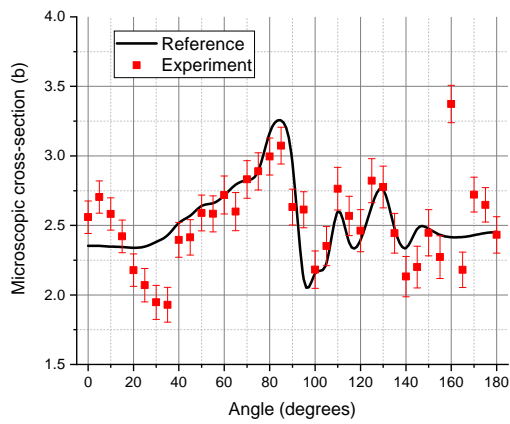


(e) Sodium - Na from NaCl, CCl₄, and C.

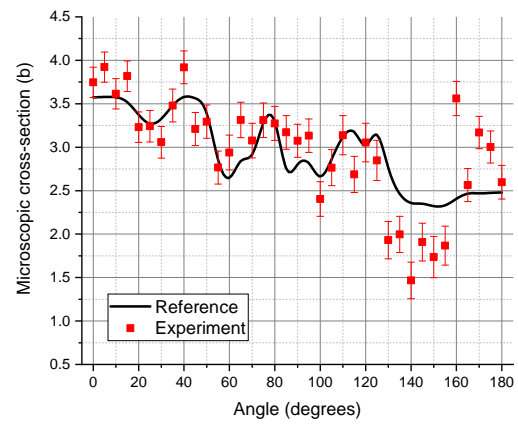


(f) Steel 316L, from pure sample.

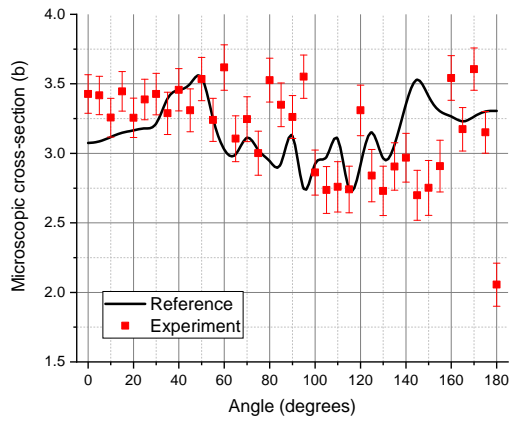
Figure 2.32 – Microscopic cross-section of Li, Mg, N, Na, and steel 316L. Deuteron beam of 80 keV.



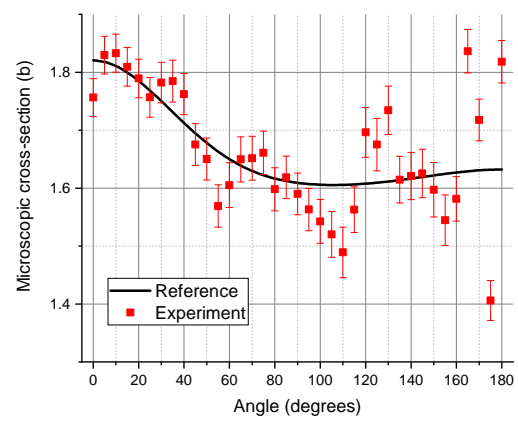
(a) Silicon - Si from pure sample.



(b) Sulfur - S from pure sample.



(c) Phosphorus - P from pure sample.



(d) Carbon - C from pure sample.

Figure 2.33 – Microscopic cross-section of Si, S, P, and C. Deuteron beam of 80 keV.

Table 2.5 – List of the nuclides of interest, with their SMAPE

Nuclide	Based on	SMAPE 0-180° (%)	SMAPE 0-90° (%)
Aluminium - Al	Al	1.55	1.13
Arsenic - As	As	3.62	2.01
Boron - B	B	3.73	1.95
Beryllium - Be	BeO, Al, and Al ₂ O ₃	4.34	2.09
Bromine - Br	C and C ₆ Br ₆	5.85	3.87
Carbon - C	C	1.69	0.87
Calcium - Ca	Ca	8.50	3.57
Chlorine - Cl	C and CCl ₄	5.07	2.51
Fluorine - F	C and C ₂ F ₄	2.63	2.01
Hydrogen - H	C and C ₂ H ₄	3.62	3.13
Hydrogen - H	H ₂ O, Al, and Al ₂ O ₃	1.64	1.27
Lithium - Li	LiCl, C, and CCl ₄	7.49	3.57
Magnesium - Mg	Mg	8.98	5.52
Nitrogen - N	AlN and Al	9.46	4.81
Nitrogen - N	BN and B	10.38	6.80
Sodium - Na	NaCl, C, and CCl ₄	6.41	3.80
Oxygen - O	Al ₂ O ₃ and Al	7.34	3.27
Oxygen - O	MgO and Mg	27.57	12.85
Phosphorus - P	P	4.73	3.20
Steel 316L	Steel 136L	2.17	1.12
Sulfur - S	S	5.90	3.11
Silicon - Si	Si	3.91	3.79

sample of magnesia - in Figure 2.23e - were already poor.

The quality of the results for H, O, and N is strongly affected by the choice of the original reference samples, as highlighted by the dramatic variations of the SMAPE. For H computed from C₂H₄ and C in Figure 2.31e, the general trend seems to be even completely inverted. Referring to the reference samples in Figures 2.22a and 2.21e, it can be seen that the results were not exceptional for both samples, especially for C₂H₄, which in turn explains the poor final results after subtraction. If instead, H₂O, Al, and Al₂O₃ are used - Figure 2.31f - the results are much more consistent with the models. The same phenomenon occurs with O: when Al₂O₃ and Al - Figure 2.30c - are used, the agreement is almost perfect from 0 to up to about 130°. If in lieu Mg and MgO are taken as reference, experiment and models are inconsistent - Figure 2.30d - mainly because of the initial poor performances of Mg. Although two subtraction procedures with different samples were used to compute the microscopic cross-section of N, shown in 2.32c and 2.32d, none of them gives significantly better results.

It shall be highlighted once again that the reference models carry their own uncertainties: a deviation of the experimental data from this reference does not necessarily mean that the experimental data are poor. Instead, it could be the model that shows its limit. For example, as mentioned in Section 2.3.6, the reference discrete cross-section data can be unreliable and/or scarce. It is particularly true for arsenic, as illustrated in Figure 2.30b. The ENDF B-VII.1 library [5] gives only three data points at 2, 2.5, and 3 MeV. Because of the uncertainty of the experimental data, it cannot be concluded that a more accurate cross-section curve was acquired and that new structures were discovered. They could partially be the result of counting statistics artifacts.

2.5.3 On the measurement reproducibility

An essential aspect of any scientific approach is its reproducibility. All the calibration results presented above were repeated at least twice in order to insure that the curves could be reliably reproduced, taking into account the expected data scatter due to counting statistics. As an illustration, Figure 2.34 reproduces all the datasets available for the alumina sample. It is clear that the main trends remain similar from one measurement to the other, proving hence the robustness of the method. Random errors can also be identified, such as at the end of the angular range: the two measurements from August 2019 show large discrepancies, in a rather opposite fashion, while older datasets remain closer to the model.

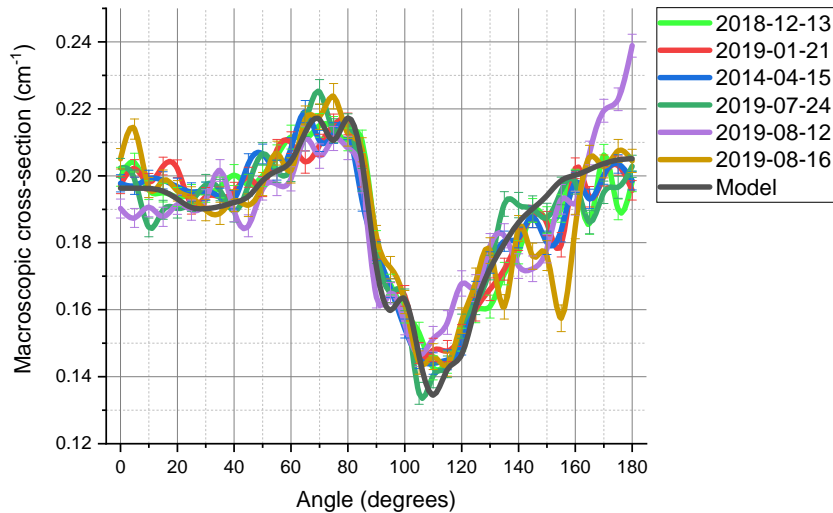


Figure 2.34 – Repeated measurement of the alumina macroscopic cross-section. The model corresponds to the “uniform” deuterium implantation, coupled to a realistic deuteron impact vector.

2.6 Summary

In Chapter 1, it was shown that spectrum-averaged microscopic cross-section data were critical to the establishment of a material decomposition technique around the PSI DD neutron generator. Beyond attenuation data, the neutron spectrum and the discrete microscopic data should therefore be accurately known input data.

In the current chapter, models of the neutron spectrum around the generator were presented, based on physical considerations and literature. The models were partially validated by spectroscopic measurements carried out with a high-resolution He-3 spectrometer. In spite of all the deployed efforts, uncertainties about the spectrum remained. The discrete microscopic cross-section data - available from external international database - also show limitations. It was therefore decided to circumvent both difficulties through a calibration method. Instead of trying to determine the intermediate variables - the neutron spectrum and the microscopic cross-section data - the spectrum-averaged cross-section data were directly measured via reference samples.

Due to technical difficulties, these setup-specific data also carry a certain degree of uncertainty. Since the main trends are still observable, they will nevertheless be kept as reference input data for the next chapter. The next chapter will focus on scaling up the material decomposition technique of Chapter 1 to two-dimensional tomographic images of unknown samples.

Die Farbe hat mich
Paul Klee

Chapter 3

From a one-pixel approach to full computed tomography

In Chapter 2, it was demonstrated that the PSI generator is suitable for energy selective attenuation measurements. Until now, all the data have been gathered with a 1-pixel setup applied to well-characterized samples. The following chapter is focused on scaling up the technique to a multi-pixel imaging device outputting 2D images of unknown samples. As it was mentioned in Section 1.8.3, the approach is in principle very similar and consists of treating each pixel of the reconstructed 2D image independently and apply to them the same kind of material decomposition.

3.1 The fast neutron CT setup

The trolley that was introduced in Section 2.3.1 was upgraded in order to reach the new objectives. The mechanics behind the motion remained identical albeit with a bigger stepper motor [50] since the total mass of the new trolley setup increased. The motor is placed upside-down compared to the previous versions, in order to accommodate the array of neutron detectors. There are exactly sixty individual plastic scintillators coupled to the dual SiPM configuration, described previously in Section 1.8.2, and they are set up in a fan-beam arrangement centered with the neutron source. This setup was developed in the frame of a previous study and details can be found in [51]. Each scintillator has an area facing the source of $5 \times 8 \text{ mm}^2$ and a depth of 80 mm. The pitch of the scintillators is 6 mm. The larger array of amplifying electronics is positioned on top of the scintillator array so it does not interfere with the CT field of view.

A rotation stage CR1-MZ7 from Thorlabs [52] is used to provide the second rotational degree of freedom needed for the CT imaging object projection angle. Connected via USB to the central unit - a role still played by a Raspberry Pi 3 Model B - the connection is subsequently channeled via a USB-server solution called VirtualHere [53]. The remote computer running the overarching software - still Matlab - will see the rotation stage as if it was directly connected to one of its local USB ports, although the computer can be anywhere as long as it is in the same Ethernet network. Matlab is then able to control accurately the stage via an ActiveX interface developed by its manufacturer Thorlabs. Figure 3.1 gives an updated version of the network routing. Figure 3.2 is a computer design of the setup, while Figure 3.3 is an actual photograph.

The rest of the experimental environment (room, shielding, etc.) was kept identical to the calibration of Chapter 2. This way, the previous reference measurements are still valid.

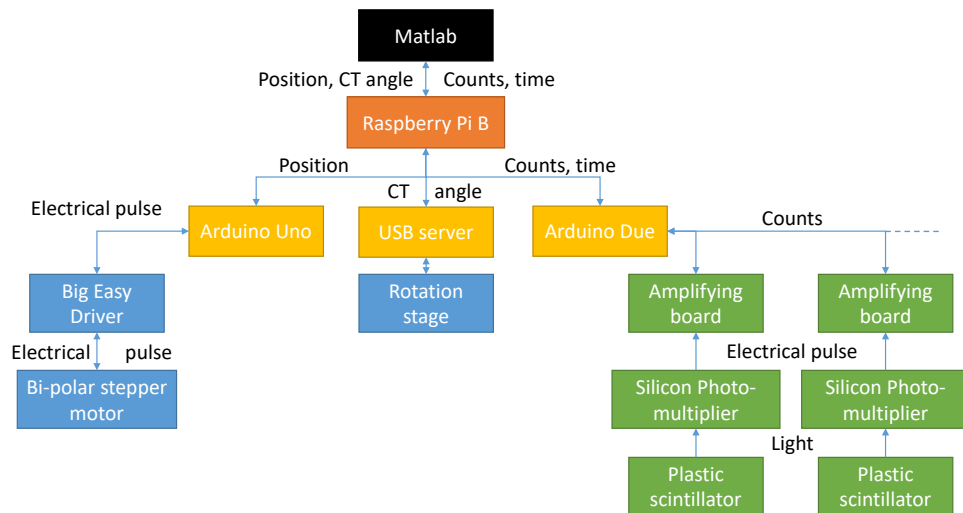


Figure 3.1 – Information routing overview of the CT measurement setup.

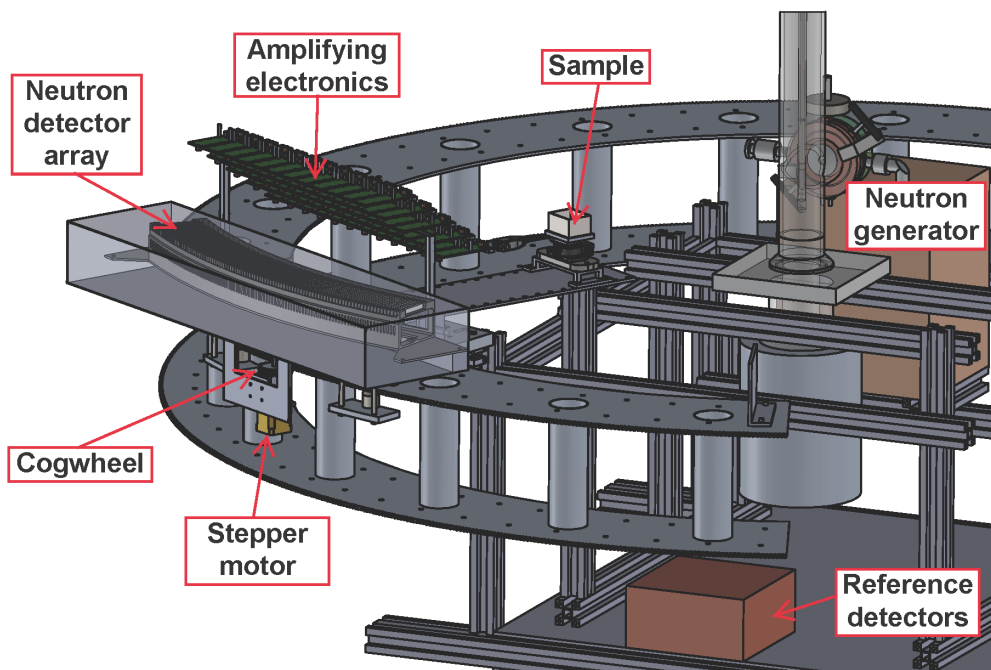


Figure 3.2 – CAD model of the CT measurement setup.

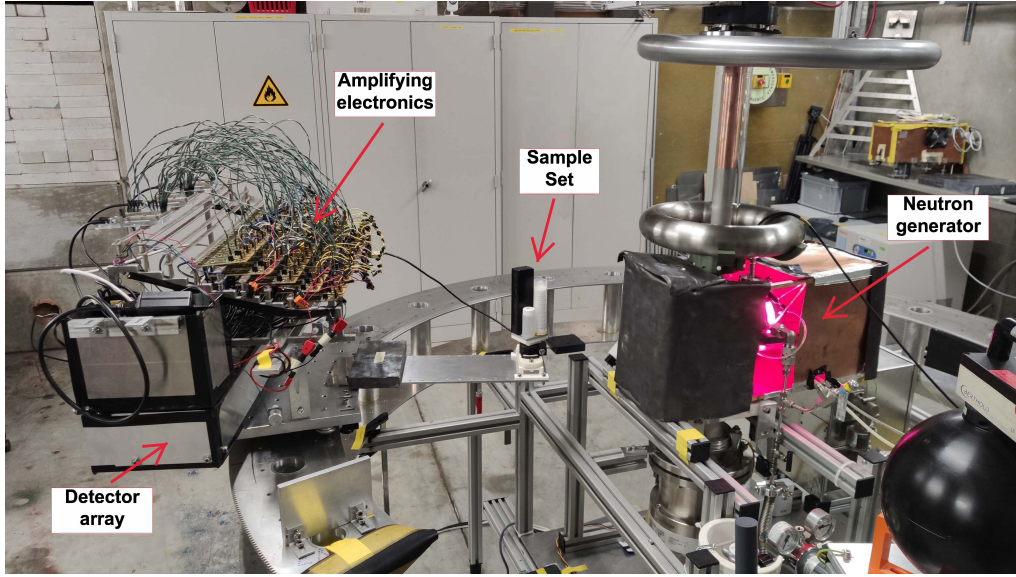


Figure 3.3 – Photograph of the CT measurement setup.

3.2 CT measurement method

The measurement methodology introduced in Section 2.3.2 for the 1-pixel setup is also followed for the CT measurements, with the exception of the MCNP6-based sample scattering correction. Indeed the samples treated here are not initially defined, therefore no accurate models can be established. Because the volume of the new samples was kept small and the distance object-detector similar to the 1-pixel arrangement, the contribution is expected to be similarly negligible as shown in Section 2.3.2. Hence, per sample and neutron spectrum (i.e. trolley position), only three kinds of attenuation measurement are needed: “flat field” I_{emp} , without the object in the field of view, “with sample” I_{τ} , and “blinding cone” I_{BC} - for the room scattering correction, an effect far from being negligible. Equation 2.6 can therefore be slightly simplified into Equation 3.1.

$$N_i = \frac{1}{\sigma_i \cdot \tau} \cdot \ln \left(\frac{I_{\tau} - I_{\text{BC}}}{I_{\text{emp}} - I_{\text{BC}}} \right) \quad (3.1)$$

For the CT to be successful, the attenuation measurement for a given sample and neutron spectrum should be repeated at different CT projection angles, i.e. after a step-wise rotation of the sample on itself thanks to the dedicated rotating stage. Exposure times and number of projections were chosen to be a balance between total measurement time and image quality. According to the Shannon-Nyquist sampling theorem [54], the minimum number of CT projections P should be greater than $\frac{\pi}{2} \cdot R$, with R the number of rays, i.e. the number of detectors. Since there are 60 detectors, that’s a minimum of 95 projections. To minimize reconstruction artifacts and secure a certain robustness of the method, more projections were used: 360 equally-spaced positions in steps of 1° from 0° to 359° were used. The exposure time was adapted to each trolley position to keep similar counting statistics by targeting a minimum of 500-1000 counts throughout the experiment. The final result of a CT acquisition for a given trolley position and sample is therefore three count matrices, (I_{τ} , I_{emp} , and I_{BC}) of dimensions 60×360 , the rows being the sixty neutron detectors and the columns the 360 CT projections. The following Section 3.3 will detail how from the three matrices an image can be reconstructed.

Two different “unknown” samples were investigated with the CT apparatus. They are only called unknown because a material decomposition will be attempted from their aggregated data. How-

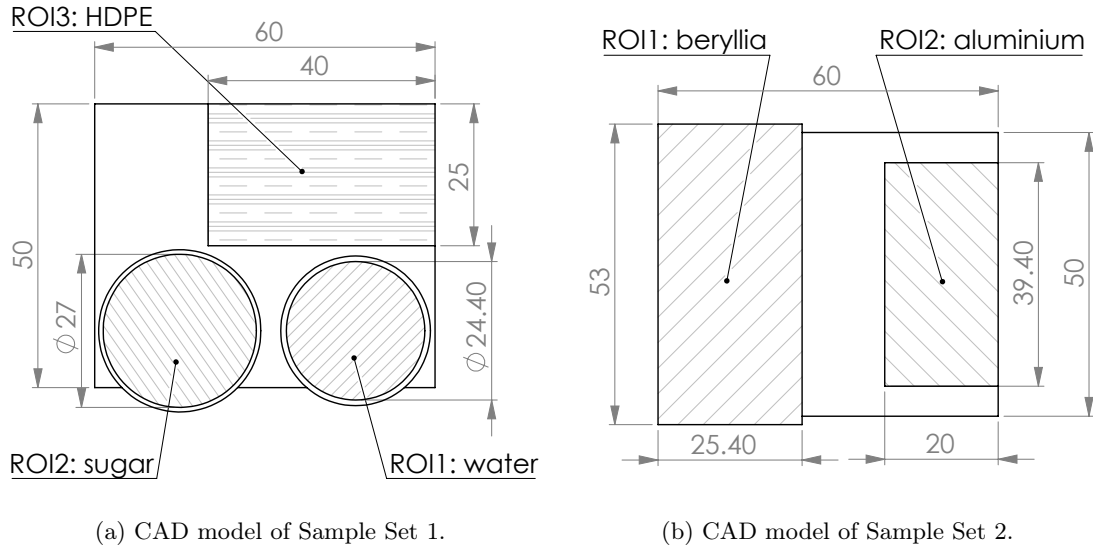


Figure 3.4 – The two sample sets used for CT imaging. The dimensions are given in millimeters.

ever, it is necessary that these samples are still in reality well-characterized to be able to assess the accuracy of the attempted material decomposition. *Sample Set 1* is made of a block of solid high-density polyethylene (C_2H_4), one cylinder of powder sugar ($C_{12}H_{22}O_{11}$) and one cylinder of liquid deionized water (H_2O). *Sample Set 2* consists of two solid blocks of aluminum (Al) and beryllia (BeO). A CAD model of both samples with their dimensions is shown respectively in Figures 3.4a and 3.4b. On these figures, the regions of interest (ROIs) are also introduced for a quicker reference hereafter.

The whole CT acquisition was repeated at several trolley positions (i.e. neutron spectra) that were selected to use most of the relevant cross-section structures that are susceptible to enhance the contrast: 0° , 40° , 60° , 90° , and 115° . The corresponding structures are highlighted in Figure 3.5. It should be noted that other trolley position combinations are possible. Due to time constraints and neutron beam availability, it was not possible to test thoroughly more of these combinations. Because the 120° to 180° region proved to be subject to interference, as shown in Section 2.5.2, it was decided not to acquire data in that region.

Both samples were also imaged with a photon source, namely a Cobalt-60 source of $1.32 \cdot 10^8$ Bq, to highlight the poor contrast obtained, compared to fast neutron imaging.

3.3 CT reconstruction steps

3.3.1 CT data normalization

Before any aggregation, it is necessary to preprocess the three matrices I_τ , I_{emp} , and I_{BC} . The data are first normalized to the counts registered by the four reference detectors which stay in a fixed position below the generator, to account here again for the neutron generator undesirable output variations, as for the 1-pixel arrangement of Section 2.3.1. A handful of isolated dead pixels also happened to send spurious information. The count rates of the dead pixels were discarded and replaced by values obtained with a piecewise cubic hermite interpolating polynomial based on the neighboring values.

The data can then be aggregated into a unique sinogram S by applying Equation 3.1 to each $n \times m$ matrix elements $S_{i,j}$ independently, as illustrated in Equation 3.2. A representation of the

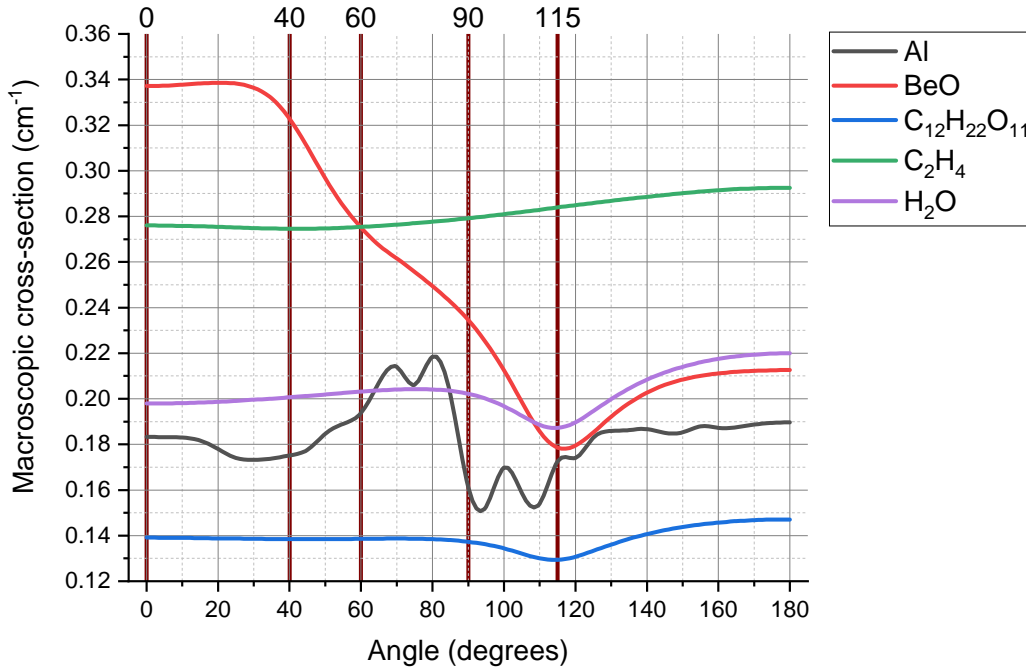


Figure 3.5 – Macroscopic cross-sections structures in the samples of interest, according to the model featuring a “uniform” deuterium distribution, and a realistic deuteron impact vector distribution.

sinogram structure is given in Figure 3.6: a column (i.e. a given CT projection) is highlighted in green, and a row (i.e. a given detector throughout all the CT projections) in yellow. At the crossing is located the value $S_{i,j}$ for a given detector i at a given projection j .

$$S_{i,j} = -\ln \left(\frac{I_{\tau,i,j} - I_{BC,i,j}}{I_{emp,i,j} - I_{BC,i,j}} \right) \quad (3.2)$$

Some further rectification of the sinogram was needed for robustness of the analysis. Because for some pixels the logarithm calculation lead to complex values - coming from negative arguments - only the real part of the result was kept for further analysis. The sinogram was then spot-filtered. This means that any given outlier value is replaced with a [10,1] median filtering, i.e. 10 in the sense of the neighboring detector values.

The standard CT reconstruction methods assume that the source, the sample rotation center, and the center of the CT imaging detector array are aligned along a straight line. In practice, except on dedicated high-precision measurement benches, such a geometrical constraint can only be approximately true and misalignment can cause artifacts on the reconstructed image. It was therefore necessary to shift the sinogram to correct for this real-world misalignment and avoid artifacts during the image reconstruction. This was applied on a sub-pixel basis, interpolating as necessary. In order to find the optimum shift, a sensitivity study was carried out on the comparison between the projections at 0° and 180° . Ideally, for a parallel beam CT arrangement, at 180° the CT projection is the mirrored version of the one at 0° . The current setup is in a fan beam mode, but thanks to the geometry of the problem (sample size, location, and pixel size), this 0° versus 180° is a good enough approximation because the reconstructed image is not very finely resolved. The optimum centering giving the best curve alignment for one of the sinograms

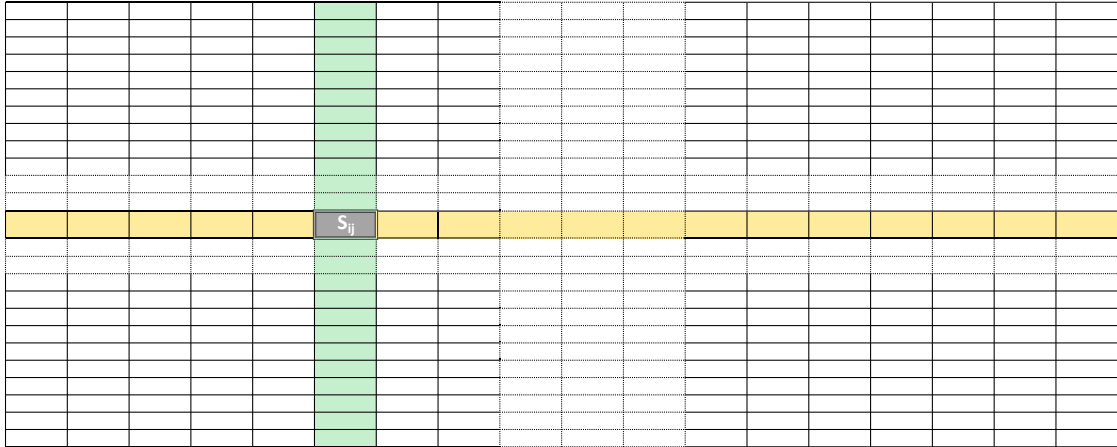


Figure 3.6 – Structure of the CT sinogram. A line, highlighted in yellow, corresponds to a given detector across all the Ct projections. A column, in green, represents a given CT projection across all the detectors.

Table 3.1 – Centering correction applied to each sinogram.

Sample	Imaging modality	Centering correction (pixel)
Sample Set 1	Co-60	none
Sample Set 1	Fast neutron	0.8
Sample Set 2	Co-60	none
Sample Set 2	Fast neutron	0.5

is shown in Figures 3.7a and 3.7b. The correction applied to each image is summarized in Table 3.1.

Since the Sample Sets are in fact well-characterized, it was possible to predict in advance their macroscopic cross-section. It was established that a further correction was needed so that the experimental cross-section data would match this estimate. A correction acting on the scattering component I_{BC} is proposed: a constant factor a_{BC} in front of it artificially increases its prominence in the calculation, transforming Equation 3.1 into Equation 3.3. A sensitivity study on this factor a_{BC} was carried out, and its results are shown in Figure 3.8. From this study, the factor $a_{BC} = 1.5$ fitted best. Physically, this correction means that the original blinding cone fails to capture the scattered component in its entirety. A much bigger blinding cone structure was used in the case of the CT, compared to the 0D case, since the imaging arc is much wider. It is possible that part of the scattered flux is absorbed along with the direct flux, and therefore not properly recorded. This effect is difficult to estimate because of the very intricate surroundings of the detector arc, filled with small components that would be difficult to simulate with MCNP6. This correction and hypothesis could be tested further in future simulations and measurements. New causes might be thereby identified.

$$N_i = \frac{1}{\sigma_i \cdot \tau} \cdot \ln \left(\frac{I_\tau - a_{BC} \cdot I_{BC}}{I_{emp} - a_{BC} \cdot I_{BC}} \right) \quad (3.3)$$

3.3.2 CT reconstruction algorithm

Once the data have been fully corrected, a CT reconstruction algorithm can be used. The most commonly used method, the filtered back-projection (FBP) [28], is relatively computationally expensive. In essence, it consists of smearing back each individual CT projection data, after

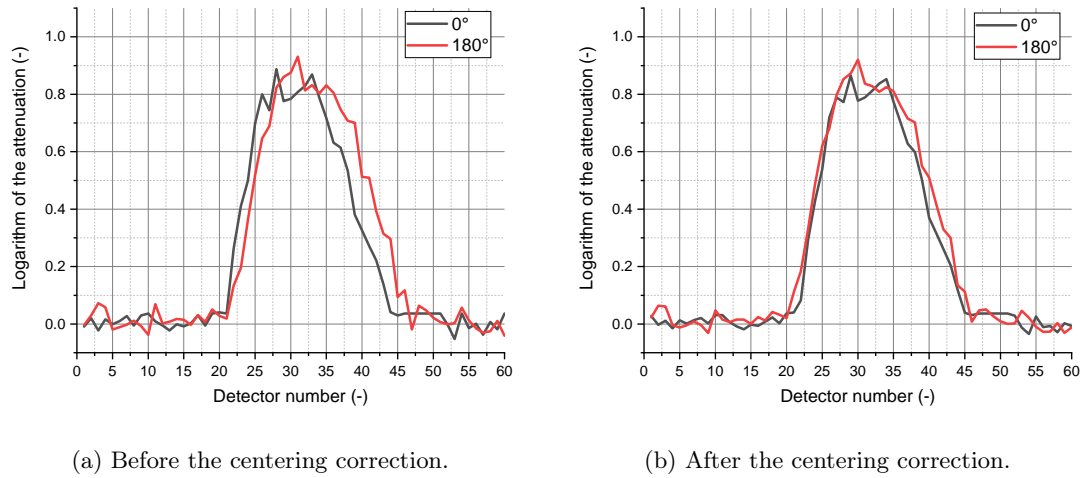


Figure 3.7 – Effect of the centering correction on the CT projection at 0 and 180°. The logarithm of the attenuation is plotted, according to Equation 3.2.

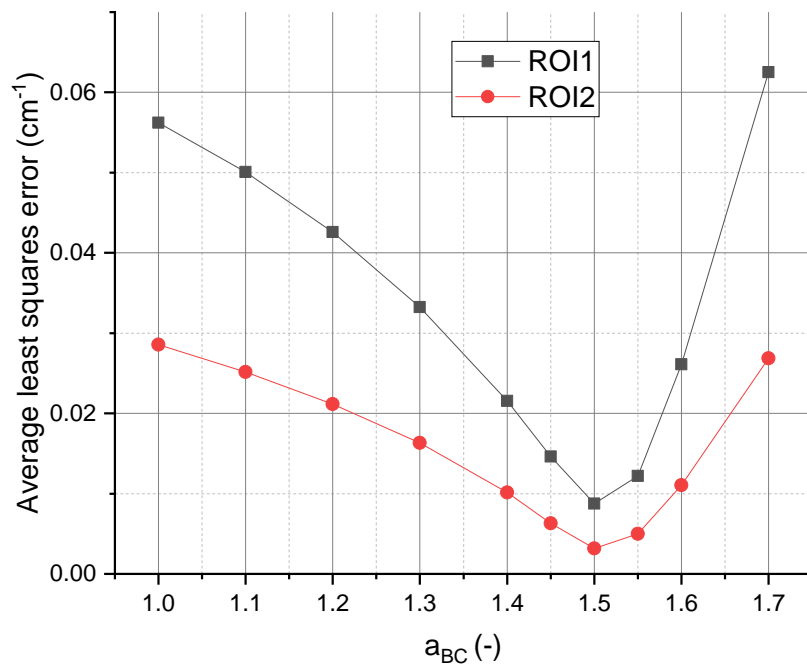


Figure 3.8 – Sensitivity study on the scattering component factor. The least squares study was computed over all the available trolley positions.

filtering, to form a reconstructed image. One option for filtering is the “Hann” filter which is typical when data is relatively noisy, as is the case here, and is therefore used in the frame of this work.

An alternative reconstruction algorithm, the Simultaneous algebraic reconstruction technique (SART) [55] was also tested. Since the current case is well-defined with many CT projections available consistently between 0° and 360°, the FBP algorithm already gives good results and the preliminary SART results did not bring significant improvements. They are therefore omitted here for the sake

Table 3.2 – Sample Set 1 - Median grayscale values (cm^{-1}).

ROI	0°	40°	60°	90°	115°
1	0.193	0.195	0.198	0.199	0.166
2	0.159	0.158	0.153	0.162	0.153
3	0.277	0.263	0.243	0.275	0.345

of conciseness. Further investigation and optimization of the SART algorithm - or other variants of algebraic reconstruction techniques - could bring more flexibility to the current material decomposition process. They are in general more robust techniques, less prone to artifacts especially in ill-defined cases such as when the CT projection set is sparse.

After the images have been reconstructed, the results obtained typically have a unit of attenuation as the inverse of a pixel characteristic length (i.e., height or width), since the reconstruction code works on a pixel basis. To convert the values into more useful macroscopic cross-sections, the grayscale values are divided by 0.252 cm, or the pixel size used for the image reconstruction. This pixel size was selected because this is comparable to what was demonstrated to be what the imaging setup could resolve [51].

3.4 CT results and discussion

3.4.1 Sample Set 1 - Images

The results of all the CT measurements are displayed for Sample Set 1 at 0, 40, 60, 90, and 115° in Figures 3.9a to 3.9e. The sinograms are critical data for the reconstruction, but they represent only an intermediary step. Therefore they are available in Appendix E.1. Since the samples are known to be homogeneous, the median grayscale value was computed over each ROI, as defined in Figures 3.4a and 3.4b. Each pixel could be considered individually, but taking the median of the ROI instead allows to reduce the unavoidable spread in the data due to counting statistics. The values are summarized in Table 3.2 and compared to the calibration macroscopic cross-section data from Section 2.5.1 in Figure 3.10. Thanks to the processing described in Section 3.3.2, the values are directly macroscopic cross-sections in cm^{-1} .

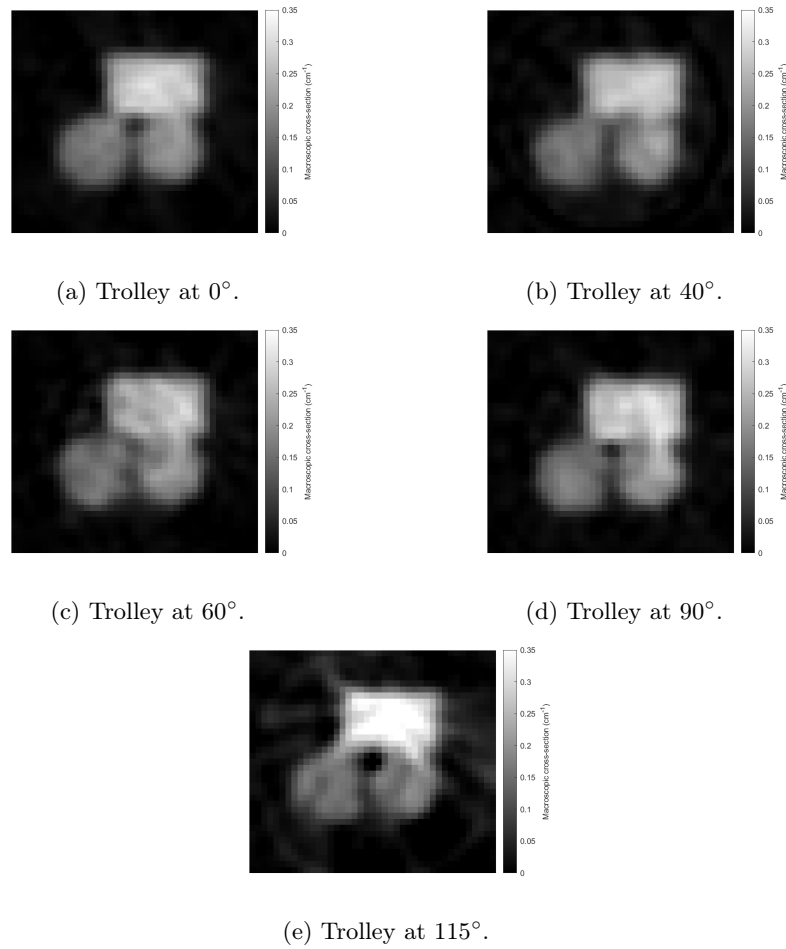


Figure 3.9 – Reconstruction of the CT of Sample Set 1 at 0, 40, 60, 90 and 115° with the FBP reconstruction algorithm.

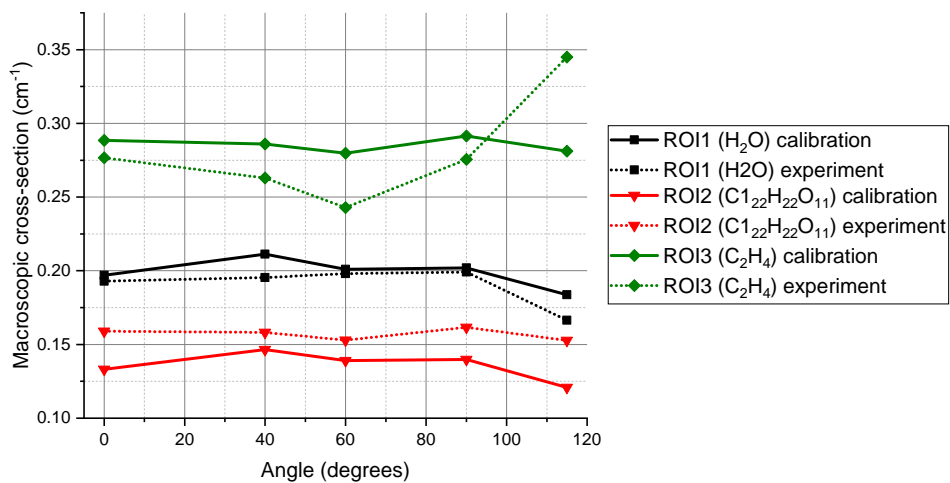


Figure 3.10 – Comparison for Sample Set 1 of the ROIs median grayscale value and the macroscopic cross-section from the calibration of Section 2.5.1.

3.4.2 Sample Set 1 - Material decomposition

The material decomposition, described by Equation 1.8, was then performed. The vector $\overline{\Sigma}_{\text{meas}}$ contains the median values of the macroscopic cross-section of the different ROIs. The matrix $\overline{\sigma}$ contains the microscopic data obtained from the calibration in Section 2.5.2.

Given that only five trolley positions are available for each Sample Set, a unique solution of the linear system of equations can be found only if there are a maximum of five unknowns, i.e. five different elements that are supposed to be present in the sample. Because the data acquired are less than ideal, five unknowns proved to be too challenging for the solver, and nonsensical solutions only were found. The number of unknowns was thereafter reduced to three, namely carbon, hydrogen, and oxygen. In this frame, the solver yielded very encouraging results, as shown in Figures 3.11a and 3.11b. The water (ROI1) and sugar (ROI2) are reasonably well reconstructed through the material decomposition process. On the other hand, the high-density polyethylene (ROI3) gives nonsensical results. It is not too surprising because, as shown in Figure 3.5, there are very few cross-section structures available and the solver struggled to differentiate one nuclide from the other.

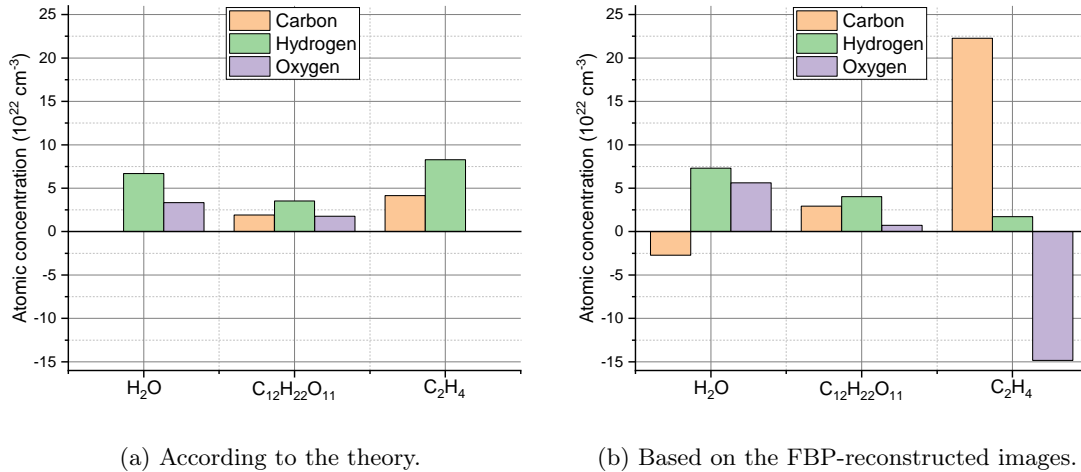


Figure 3.11 – Atomic concentrations of carbon, hydrogen, and oxygen for the three regions of interest of Sample Set 1, according to the theory and from the solution of the material decomposition linear systems.

3.4.3 Sample Set 2 - Images

The results for Sample Set 2 at 0, 40, 60, 90, and 115° follow in Figures 3.12a to 3.12e. The sinograms are also available in Appendix E.2. The median value for each ROI was computed and is summarized in the corresponding Table 3.3 and compared to the calibration macroscopic cross-section data from Section 2.5.1 in Figure 3.13.

Table 3.3 – Sample Set 2 - Median grayscale values.

ROI	0°	40°	60°	90°	115°
1	0.347	0.284	0.266	0.224	0.188
2	0.193	0.174	0.201	0.150	0.164

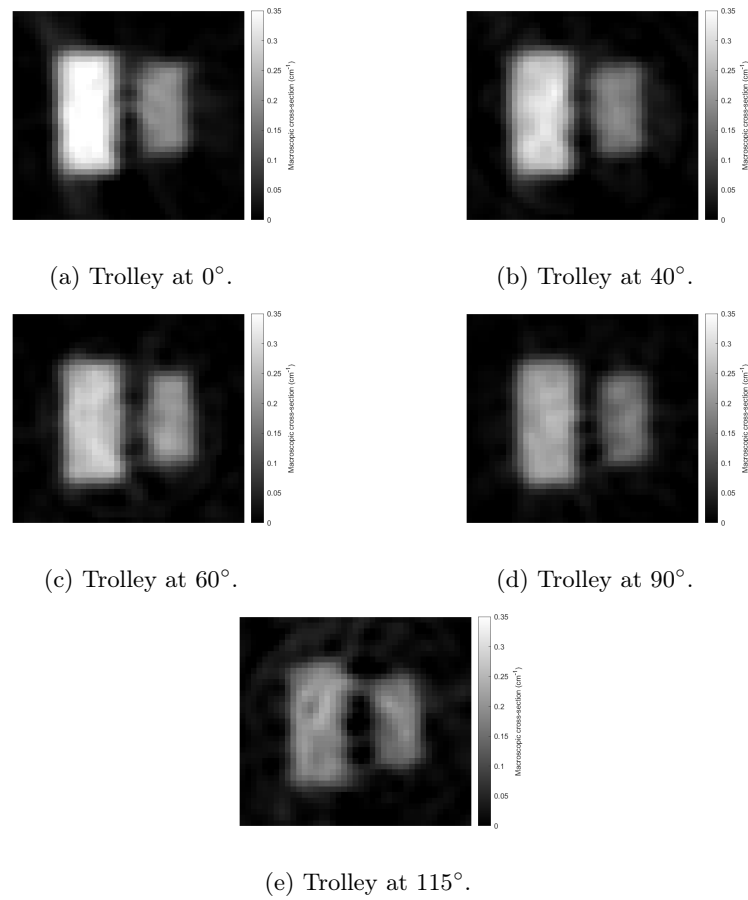


Figure 3.12 – Reconstruction of the CT of Sample Set 2 at 0, 40, 60, 90 and 115° with the FBP reconstruction algorithm.

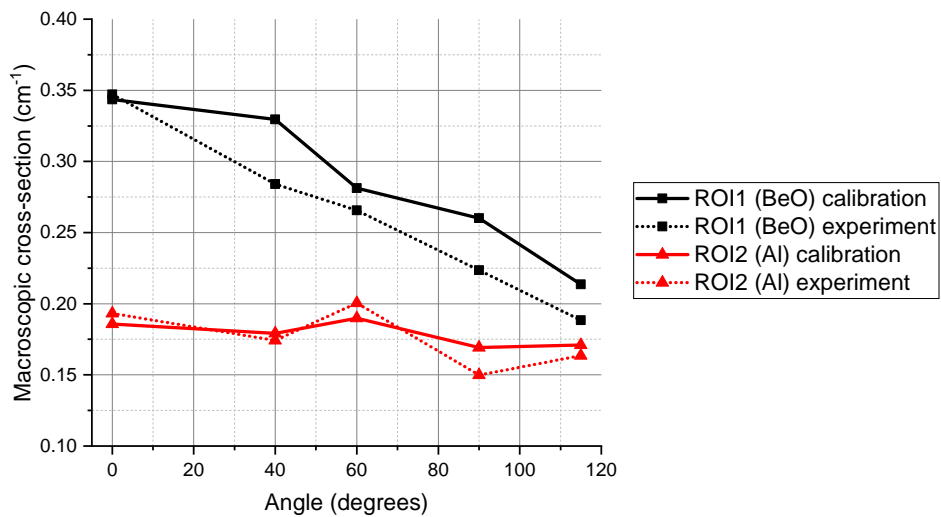


Figure 3.13 – Comparison for Sample Set 2 of the ROIs median grayscale value and the macroscopic cross-section from the calibration of Section 2.5.1.

3.4.4 Sample Set 2 - Material decomposition

The same material decomposition process described in Section 3.4.2 was also performed for Sample Set 2. The same comment about the number of unknowns remains valid and, in this case, the three unknowns elements whose concentrations should be computed are aluminium, beryllium, and oxygen. The results are available in Figures 3.14a and 3.14b. The results are very good for both ROIs, significantly better than for Sample Set 1. It is expected as the cross-section features are significantly larger for Sample Set 2, making it easier for the solver to discriminate the elements.

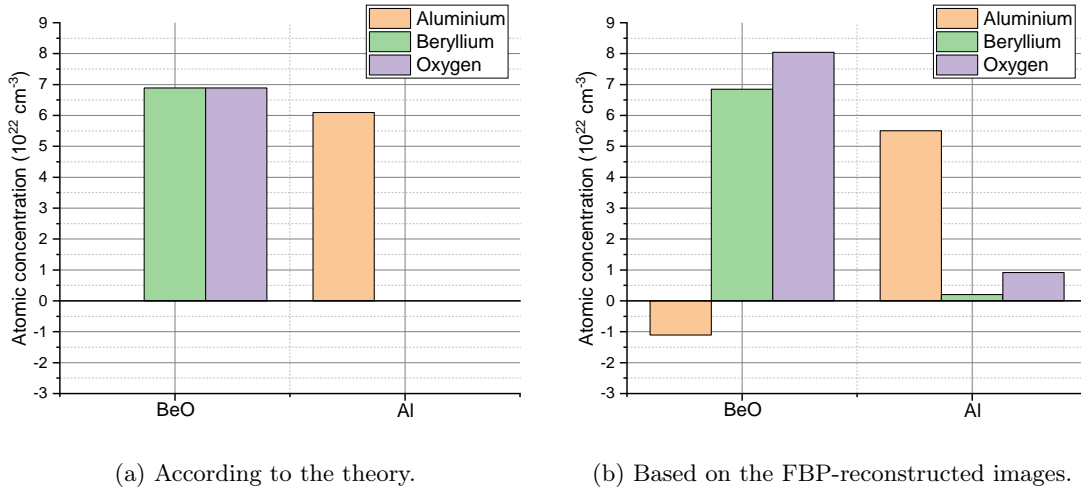


Figure 3.14 – Atomic concentrations of carbon, hydrogen, and oxygen for the three regions of interest of Sample Set 2, according to the theory and from the solution of the material decomposition linear systems.

3.5 CT with a photon source

Thanks to the licensing of the experimental area, it was possible to use a strong radioisotope Cobalt-60 source which emits mainly gamma rays at 1.17 MeV and 1.33 MeV. Since plastic scintillators are also sensitive to photons, no further major modification to the imaging setup presented in Section 3.1 was needed. Only a mechanical adapter was used to set up the radioisotope source at the same location as the neutron source, so that the imaging arc is properly centered, as shown in Figure 3.15. Because the cobalt source requires neither cooling nor external power, it was possible to leave the measurement setup unsupervised for long periods of time, for example overnight. Taking advantage of this stability, 720 CT projections were used, instead of 360 like in the neutron case, to improve the final image quality. The count rates registered were also on average ten times higher, enhancing further the quality of the reconstruction. The results for Sample Set 1 are shown in Figure 3.16a, and for Sample Set 2 in Figures 3.16b. Both sinograms are available in Appendix, Section E.3.

The contrast between the ROIs is much poorer compared to the fast neutron images, as it was already highlighted in [4]. This is clearly visible when looking at Table 3.4 which summarizes the median of the same ROIs as with fast neutrons. The grayscale values were arbitrarily normalized altogether. The normalization presented for neutrons in Section 3.3.1 was not applied here since the imaging conditions, especially scattering, are different. Because the objective of this section is to compare the attenuation of the ROIs relative to each other, the normalization to cm^{-1} is not necessary. The relative differences between ROIs were computed, using the ROI1 as reference for each image. The relative values for these particular samples are only of a few percents. This

photon source does not allow to properly discriminate, even visually, one type of sample from the others. Since it outputs only one kind of energy spectrum, it is also not possible to apply the material decomposition technique such as with fast neutrons.

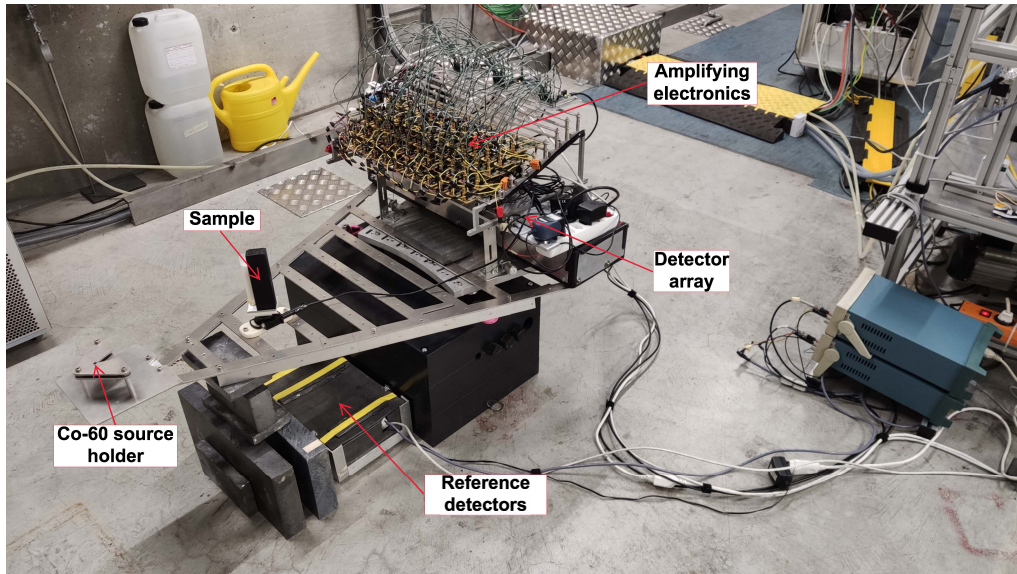
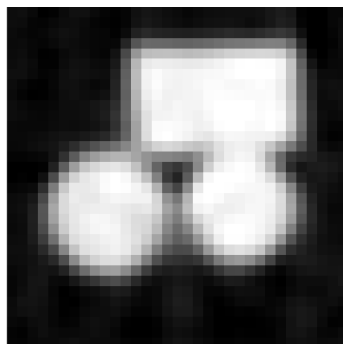
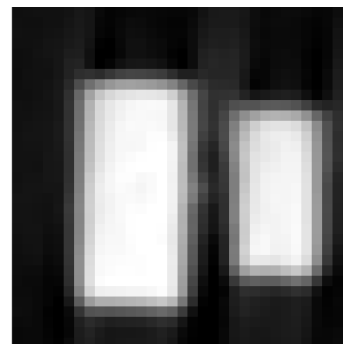


Figure 3.15 – Photograph of the CT measurement setup, adapted to the measurement with the Co-60 source.

Energy-selective photon imaging is an option that has been explored in the frame of other projects, but is intrinsically limited in its application because of the photon cross-section behavior described earlier in Figure 1.2. In order to find trends that are material or nuclide-specific, the low-energy range needs to be considered, in which probed density and depth are very limited, as mentioned in Section 1.4.1. Enhanced imaging is nevertheless obtained for applications such as in the medical field, with notably the so-called dual-energy imaging technique [56]. Additionally, since neutrons and photons interact with matter in intrinsically different manners - as detailed in Section 1.4 - they are likely to yield complementary information. The so-called dual particle imaging has been studied in the last decades with application such as homeland security [57, 58] or nuclear non-proliferation [59, 60]. Images acquired with both types of particles can then be overlapped and further information about the nature of the sample can be inferred.



(a) Sample Set 1.



(b) Sample Set 2.

Figure 3.16 – Reconstruction of the CT of Sample Set 1 and 2 around a Co-60 source, with the FBP reconstruction algorithm.

Table 3.4 – Contrast obtained with the Co-60 photon source

ROI		Sample Set 1	Sample Set 2
1	Median grayscale	1.33	3.21
	Relative difference (%)	-3.6	-2.9
2	Median grayscale	1.28	3.12
	Relative difference (%)	-3.6	-2.9
3	Median grayscale	1.34	-
	Relative difference (%)	1.2	-

3.6 Summary

This chapter was focused on the scaling up to 2D of the 0D energy-selective method introduced in Chapter 2.

CT data of two “unknown” heterogeneous samples were obtained with a fan-beam array of neutron detectors. The samples are in fact well-characterized but considered unknown so that their known composition could be compared with what was computed from the CT data. From the CT data acquired at five different trolley positions, cross-sectional images were reconstructed using FBP.

The material decomposition technique presented in Chapter 1 and based on reference data from Chapter 2 was then applied to the median of several ROIs defined for each sample. Albeit using only few trolley positions, very promising results were obtained for most of the samples. It should be highlighted that only three unknowns were introduced in each problem to be solved, making it easier for the solver to find a physical solution. More unknowns did not give satisfying results. To preserve the robustness of the approach with more unknowns, more trolley positions corresponding to unique cross-sections structures are needed.

Imaging with a Cobalt-60 photon source was attempted with the same CT arrangement since the detectors are also photon-sensitive. The poorer contrast between ROIs containing different materials and the lack of energy-selectivity with such a source were confirmed, as it was expected.

The following chapter will first focus on detailing several concepts that have potential to improve the overall performance and applicability of the energy-selective imaging approach, which can be considered for future work. The overall achievements will then be summarized and commented.

Per aspera ad astra

Chapter 4

Conclusion and outlook

The very promising results presented in the previous chapter could be brought further by some technical upgrades that will be presented thereafter. After the presentation of these potential improvements, the last section of this chapter will summarize all the achievements of this doctoral work.

4.1 Conceptual study of alternative sources

4.1.1 Increasing the deuteron acceleration

As shown in Figure 1.6 in the first chapter of this thesis, increasing the initial deuteron acceleration towards higher values would affect positively the total output since the DD fusion cross-section σ_{DD} increases monotonically until about 2.5 MeV. The power supply used in this study, an SR150KV-300W from TECHNIX [61]. can in principle reach a voltage of 150 kV at a maximum current of 2 mA. In the scope of the current study it was practically not possible to reach these values due to limitations such as frequent high voltage breakdowns. Heat dissipation is another issue which must be dealt with at increased power, as an overheated target leads to deuterium outgassing and lower fusion rate. At high voltage, however, even if current is reduced to keep overall power the same, there is a significant increase in neutron output. These practical aspects limited the maximum acceleration to 80 kV for the PSI neutron generator. Assuming that the generator does not run into other limitations and everything else is held constant, increasing the acceleration from 80 kV to 150 kV would increase the total neutron output by a factor of 4.9. If the power is kept constant, the increase in output is about 2.6.

This increase in voltage also brings in another improvement, which for the present study is even more critical than the output itself: it **extends the final neutron energy range**, as demonstrated in section 1.7.2. An extended neutron range means that more cross-section structures can be captured by the setup. As an example, Figures 4.1a and 4.1b show the the spectrum-averaged ENDF evaluated microscopic cross-section data [5] of four nuclides of great interest - hydrogen, carbon, nitrogen, and oxygen. The weighting was done with the “uniform” deuterium implantation model, with forward-aligned deuteron impact vector. Using the other models would not change dramatically the main trends of these curves. It is clear that a simple increase of 70 keV is beneficial since the carbon curve at 150 keV features a much larger peak in the 0° to 60° range, compared to the 80 keV case.

If a higher voltage power supply were available, and the practical limits were pushed further, e.g. to 300 kV, the output and energy spread would be further improved. If a more powerful accelerator were used to bring the deuteron energy into the MeV range, even more cross-section structures are covered. Taking for example a typical radio-frequency quadrupole acceleration energy (an option currently becoming more widely available outside of a research environment, e.g. as in a

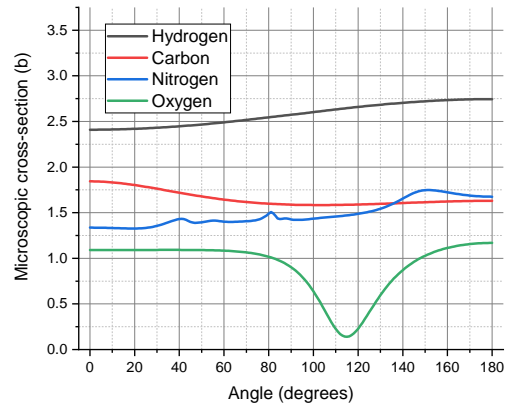
commercial generator produced by Starfire Industries [62]), a deuteron beam of 3900 keV was also simulated and the corresponding cross-sections for the same four elements of interest are plotted in Figure 4.1c. It should indeed be highlighted that in the case of a drive-in target technology, the neutron spectrum at each emission angle will get broader as the deuteron acceleration voltage increases. As long as the newly covered cross-section structures are remarkable enough in width - i.e. covered energy span - and amplitude, the averaging effect due to a wider spectrum - described previously with Equation 1.9 - could be counterbalanced.

With a potential future neutron generator, a different approach for energy-selective measurement could be used. Instead of a rotating trolley, the direction of the measurement could be fixed in the 0° direction, and the acceleration tuned according to the needs. Figure 4.2 shows what would be the effect on a couple of standard samples: water, graphite, the explosive RDX, and crude oil. The plots show the spectrum-averaged macroscopic data, with a similar weighting pattern as in Figures 4.1a, 4.1b, and 4.1c. The negative effect of the ever larger spectrum due to the stronger slowing down of deuterons is visible in the high end of the deuteron energy range. Although more and more element-specific cross-section structures are covered - as it was shown in Figures 4.1a and 4.1b - they are slowly averaged out and the relative tendencies from one sample to another do not differ strongly above 300 keV. It should also not be forgotten that in the lower end of the deuteron acceleration, the fusion rate significantly decreases due to smaller DD fusion cross-section. For example at 50 kV, the fusion is about 2.5 times less likely than at 80 kV. Longer exposure times would be needed to obtain sufficient statistics.

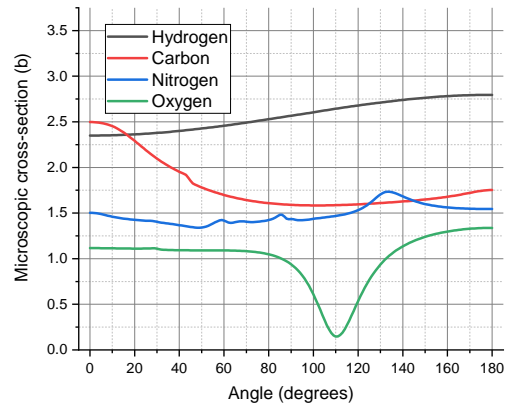
4.1.2 Reducing the neutron spread

The main drawback of the drive-in target technology used in the frame of this study is the very likely deuteron slowing down before fusion which leads to non-monoenergetic neutron spectra. A first solution would be to decrease the thickness of the host material, titanium, so that the end of the layer plays the role of cutoff. However, a 80 keV deuteron has an approximate range of only 1 μm in a material such as titanium hydride TiD_2 . It means that the titanium layer should be manufactured to be sub-micrometer sized. It would be technically challenging to produce such a thin layer and sputtering by the deuteron beam might lead to short target lifetime, as shown in [21]. Mechanically, the target could not only be made of such a thin layer of metal, since it is supposed to sustain several bars of pressure difference between the high vacuum section and the air cooling lines. A backing material - such as copper which is currently used - is needed. It is physically possible that deuterium would also integrate the copper matrix if it is within the range of the ions. It is not as good an host as titanium (1:1 maximum ratio with deuterium instead of 2:1 in the hydride form) so the fusion rate in that region would be smaller, but it would not provide the sharp cut-off that is needed to make the neutron spectrum monoenergetic. This happens at the price of some neutron output reduction.

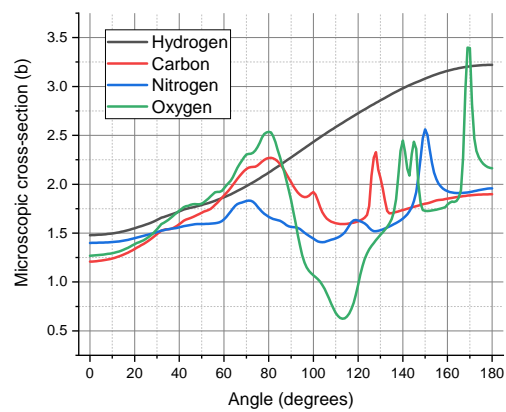
A change of paradigm is needed to reach the monoenergetic Holy Grail. Instead of a metal drive-in target, alternative designs have been explored in the past. A promising one is the deuterium gas target. A constant stream of deuterium gas moves in front of the deuteron ion beam and fusion might happen when they meet each other. Such a design was used in [63] to establish a very promising energy-selective measurement method, although only in radiography mode. The gas in the target chamber should ideally be maintained at several bars in order to provide decent deuterium concentration so as to achieve a good fusion rate. If the original design with the trolley rotating around the source is kept, then this solution has a major drawback. The straggling of the deuterons in the gas can be significant. For example, taking the working point of [63], a 1.6 MeV beam in 6 bars of D_2 will typically have a range of about 2.2 cm according to SRIM calculations [31]. Orthogonal to this straggling direction, the neutron emission point will be spread over more than two centimeters and far from an ideal point source. This will be a major disadvantage for imaging applications since it will add a large blur to the final image. If the gas chamber is large enough,



(a) 80 kV deuteron beam.



(b) 150 kV deuteron beam.



(c) 3900 kV deuteron beam.

Figure 4.1 – Evolution of the spectrum-averaged microscopic cross-section of hydrogen, carbon, nitrogen, and oxygen, depending on the initial deuteron energy.

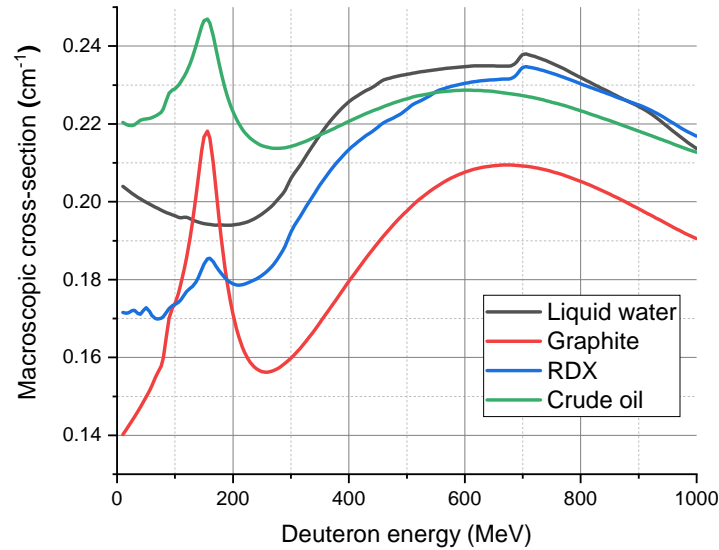


Figure 4.2 – Macroscopic cross-section variations for selected samples in the forward direction (0°) when the deuteron acceleration is modified.

it means the same effect as for the solid target will happen: the deuteron is slowed down entirely and the inherent spread of the neutron energy remains. However the gas cell can be shortened, so that is only a fraction of the energetic deuteron range. A second chamber containing a flowing inert denser gas such as argon can then be used as a beam dump [64]. The continuous argon flow removes deuterium from the system so that the fusion probability remains below detectable level. The neutron energy spread can then on the principle be significantly reduced.

4.1.3 Reducing the measurement time

For a given neutron output and detection efficiency, it is possible to use various techniques to reduce the total measurement time by using the source more efficiently.

Given the rotating apparatus that was built, a carousel mode could be easily implemented: instead of having a unique trolley, several of them would be distributed around the source. Several mechanical modifications would be needed to implement these solutions, among others a full 360° system so the trolleys would never bump into each other. Stochastic simulations would allow estimation of the cross-scattering contributions due to the simultaneous presence of several trolleys. Given that this contribution was only of a few percent in the case of sample scattering with a unique sample trolley - see section 2.3.2 - this effect is expected to be negligible. Given the footprint of the current CT array, about six of those could be accommodated around the generator, which means that the measuring time could effectively divided by six.

CT in itself is time consuming since many projections are needed for an accurate image reconstruction. However, advanced reconstruction algorithms such as the ones based on iterative approaches, already introduced in Section 3.3.2, are generally more suitable for few-projections approaches. Selecting the right algorithm allows achieving a good image quality while minimizing the number of projections used, and thus reducing the total measurement time. Another very recently investigated approach [65] shows promising results with an analytical reconstruction combined with machine learning - a topic which is current rapidly expanding in its range of application - and showed that only one third of the initial number of projections was needed to maintain the same quality of image as a traditional analytical Filtered-Back Projection method. A wide range of

approaches could be developed to improve the analysis of tomographic data collected at multiple energies. For example, first using automatic region of interest definition using segmentation and clustering, then second applying iterative methods to a simultaneous solution of multiple image datasets. These and other approaches could be explored in the future.

4.2 Conclusion

From the nature of fast neutron interaction with matter, it was shown that this particle is a good candidate for beam transmission studies of robust unknown samples to obtain material decomposition information. Thanks to the strong energy- and element-dependence of fast neutron cross-sections, obtaining enough images at different neutron energies can allow reconstruction of the atomic content of a sample, and therefore to identify its nature.

Looking next for a suitable tunable neutron source, the possibility to make energy-selective fast neutron images around a compact DD fusion generator was demonstrated. Thanks to the kinetics of the fusion reaction, it is possible to move a transmission measurement line - sample and detector - in a circular motion around the emission point and measure using different neutron energies in each direction. Since the neutron spectra proved to be not entirely monoenergetic, it meant that discrete cross-section data could not be used directly but should be first convolved with the spectrum observable in a given direction. Hence, the neutron spectrum was carefully studied and modelled. The models were validated as accurately as possible with experimental data.

Both the discrete cross-section data and the spectrum models proved to have significant remaining uncertainties. In order to overcome them, instead of computing these two variables (cross-section and spectrum data) first and then doing a convolution, a calibration step based on well-known reference samples was designed and implemented. From these experimental results, it was possible to build a setup-specific spectrum-averaged cross-section database.

Once calibrated, the transmission setup was upgraded with a full 2D computed tomography capability, and was used to image slices of two unknown sample sets and subsequently obtain space-dependent material decomposition information about them. Using only five trolley positions, it was possible to reconstruct fairly well the absolute elemental content of four samples out of five. The last sample offered no cross-sections structures at the selected trolley positions and evaded a proper identification. The methodology used only three unknown elements for each sample set. A more generic approach with more unknowns would require additional images at trolley positions featuring unique cross-section structures.

The sample sets were also imaged with a Cobalt-60 radioisotope gamma source. The lack of contrast between the different samples on the photon-based images was highlighted.

The neutron-based results obtained were promising and showed that fast neutrons are an innovative tool to get elemental information about unknown samples where more established techniques fail. For now significantly limited by long measurements times due to low generator output and not so high detection efficiency, the approach could be brought further by several improvements that were discussed in detail. If it becomes possible to obtain sufficient statistics in a few seconds per CT projection, energy-selective fast neutron imaging could very well become more practically applicable in some domains like explosive and drug detection, industrial oil/water mix cases, and many more.

Nec pluribus impar
Louis XIV, roi de France et de Navarre

Bibliography

- [1] “The SINQ facility.” [Online]. Available: <https://www.psi.ch/de/bsq/sinq-facility>
- [2] R. Adams, L. Bort, R. Zboray, and H.-M. Prasser, “Development and characterization of a D–D fast neutron generator for imaging applications,” *Applied Radiation and Isotopes*, vol. 96, pp. 114–121, Feb. 2015. [Online]. Available: <http://linkinghub.elsevier.com/retrieve/pii/S0969804314004084>
- [3] H. Liskien and A. Paulsen, “Neutron production cross sections and energies for the reactions T (p, n) ^3He , D (d, n) ^3He , and T (d, n) ^4He ,” *Atomic Data and Nuclear Data Tables*, vol. 11, no. 7, pp. 569–619, 1973. [Online]. Available: [http://dx.doi.org/10.1016/S0092-640X\(73\)80081-6](http://dx.doi.org/10.1016/S0092-640X(73)80081-6)
- [4] R. Adams, “Computed tomography with a compact fast neutron generator,” Ph.D. dissertation, ETH Zurich, 2015. [Online]. Available: <http://e-collection.library.ethz.ch/view/eth:48598>
- [5] M. B. Chadwick, M. Herman, P. Obložinský, M. E. Dunn, Y. Danon, A. C. Kahler, D. L. Smith, B. Pritychenko, G. Arbanas, R. Arcilla, R. Brewer, D. A. Brown, R. Capote, A. D. Carlson, Y. S. Cho, H. Derrien, K. Guber, G. M. Hale, S. Hoblit, S. Holloway, T. D. Johnson, T. Kawano, B. C. Kiedrowski, H. Kim, S. Kunieda, N. M. Larson, L. Leal, J. P. Lestone, R. C. Little, E. A. McCutchan, R. E. MacFarlane, M. MacInnes, C. M. Mattoon, R. D. McKnight, S. F. Mughabghab, G. P. A. Nobre, G. Palmiotti, A. Palumbo, M. T. Pigni, V. G. Pronyaev, R. O. Sayer, A. A. Sonzogni, N. C. Summers, P. Talou, I. J. Thompson, A. Trkov, R. L. Vogt, S. C. van der Marck, A. Wallner, M. C. White, D. Wiarda, and P. G. Young, “ENDF/B-VII.1 Nuclear Data for Science and Technology: Cross Sections, Covariances, Fission Product Yields and Decay Data,” *Nuclear Data Sheets*, vol. 112, no. 12, pp. 2887–2996, Dec. 2011. [Online]. Available: <http://www.sciencedirect.com/science/article/pii/S009037521100113X>
- [6] E. H. Lehmann, P. Vontobel, G. Frei, and C. Brönnimann, “Neutron imaging—detector options and practical results,” *Nuclear Instruments and Methods in Physics Research Section A: Accelerators, Spectrometers, Detectors and Associated Equipment*, vol. 531, no. 1-2, pp. 228–237, Sep. 2004. [Online]. Available: <http://linkinghub.elsevier.com/retrieve/pii/S0168900204011751>
- [7] I. Anderson, R. McGreevy, and H. Bilheux, Eds., *Neutron imaging and applications - A reference for the imaging community*, ser. Neutron scattering applications and techniques. New York, NY: Springer, 2009.
- [8] N. Kardjilov, I. Manke, R. Woracek, A. Hilger, and J. Banhart, “Advances in neutron imaging,” *Materials Today*, vol. 21, no. 6, pp. 652–672, Jul. 2018. [Online]. Available: <https://linkinghub.elsevier.com/retrieve/pii/S1369702117306594>
- [9] G. F. Knoll, *Radiation detection and measurement; 4th ed.* New York, NY: Wiley, 2010. [Online]. Available: <https://cds.cern.ch/record/1300754>
- [10] V. Zerkin, “EXFOR: Experimental Nuclear Reaction Data.” [Online]. Available: <https://www-nds.iaea.org/exfor/exfor.htm>

- [11] B. Datta, *Numerical Linear Algebra and Applications, Second Edition*, ser. Other Titles in Applied Mathematics. Society for Industrial and Applied Mathematics (SIAM, 3600 Market Street, Floor 6, Philadelphia, PA 19104), 2010. [Online]. Available: <https://books.google.ch/books?id=-tW8-FUoxWwC>
- [12] S. Tavernier, “Interactions of Particles in Matter,” in *Experimental Techniques in Nuclear and Particle Physics*. Berlin, Heidelberg: Springer Berlin Heidelberg, 2009, pp. 23–53. [Online]. Available: http://link.springer.com/10.1007/978-3-642-00829-0_2
- [13] K. A. Olive and P. D. Group, “Review of Particle Physics,” *Chinese Physics C*, vol. 38, no. 9, p. 090001, 2014. [Online]. Available: <http://stacks.iop.org/1674-1137/38/i=9/a=090001>
- [14] E. Bradley and International Atomic Energy Agency, *Research reactor modernization and refurbishment*. Vienna, Austria: International Atomic Energy Agency, 2009, oCLC: 449824878.
- [15] A. Krasa, “Spallation Reaction Physics,” *Faculty of Nuclear Sciences and Physical Engineering at Czech Technical University, Prague*, 2010. [Online]. Available: <http://ojs.ujf.cas.cz/~krasa/ZNTT/SpallationReactions-text.pdf>
- [16] B. Blau, K. N. Clausen, S. Gvasaliya, M. Janoschek, S. Janssen, L. Keller, B. Roessli, J. Schefer, P. Tregenna-Piggott, W. Wagner, and O. Zaharko, “The Swiss Spallation Neutron Source SINQ at Paul Scherrer Institut,” *Neutron News*, vol. 20, no. 3, pp. 5–8, Aug. 2009. [Online]. Available: <http://www.tandfonline.com/doi/abs/10.1080/10448630903120387>
- [17] W. Mondelaers and P. Schillebeeckx, “GELINA, a neutron time-of-flight facility for high-resolution neutron data measurements,” *Notiziario Neutroni e Luce di Sincrotrone*, vol. 11, no. 2, p. 7, 2006.
- [18] I. Mor, V. Dangendorf, M. Reginatto, F. Kaufmann, D. Vartsky, M. Brandis, D. Bar, and M. B. Goldberg, “Reconstruction of Material Elemental Composition Using Fast Neutron Resonance Radiography,” *Physics Procedia*, vol. 69, pp. 304–313, 2015. [Online]. Available: <http://linkinghub.elsevier.com/retrieve/pii/S1875389215006537>
- [19] G. Csikai, *Handbook of Fast Neutron Generators volume I*. CRC Press Inc., Boca Raton, FL, 1987, vol. 1.
- [20] J. Detaint, “Préparation et fonctionnement des cibles neutronigènes à hydrures métalliques,” Ph.D. dissertation, Faculté des Sciences de l’Université de Grenoble, Grenoble, Feb. 1971. [Online]. Available: <https://www.ipen.br/biblioteca/rel/R30970.pdf>
- [21] H. Kromer, R. Adams, B. Soubelet, R. Zboray, and H.-M. Prasser, “Thermal analysis, design, and testing of a rotating beam target for a compact D-D fast neutron generator,” *Applied Radiation and Isotopes*, vol. 145, pp. 47–54, Mar. 2019. [Online]. Available: <https://linkinghub.elsevier.com/retrieve/pii/S0969804318303233>
- [22] S. G. Crystals, “BC-400,BC-404,BC-408,BC-412,BC-416 Premium Plastic Scintillators,” Saint Gobain Crystals, Tech. Rep., 2016. [Online]. Available: <https://www.crystals.saint-gobain.com/sites/imdf.crystals.com/files/documents/organics-plastic-scintillators.pdf>
- [23] R. Adams, R. Zboray, M. Cortesi, and H.-M. Prasser, “Conceptual design and optimization of a plastic scintillator array for 2d tomography using a compact D–D fast neutron generator,” *Applied Radiation and Isotopes*, vol. 86, pp. 63–70, Apr. 2014. [Online]. Available: <http://linkinghub.elsevier.com/retrieve/pii/S0969804314000086>
- [24] M. Brandis, *Development of a Gamma-ray Detector for Z-Selective Radiographic Imaging*. thesis submitted towards the Ph. D. degree at the Hebrew University of Jerusalem, The Racah Institute of physics, 2013. [Online]. Available: http://www.iaea.org/inis/collection/NCLCollectionStore/_Public/46/135/46135164.pdf

- [25] B. Soubelet, R. Adams, H. Kromer, R. Zboray, and H.-M. Prasser, “Feasibility study of using a compact deuterium-deuterium (D-D) neutron generator for energy-selective transmission tomography,” *Radiation Physics and Chemistry*, vol. 156, pp. 292–299, Mar. 2019. [Online]. Available: <https://linkinghub.elsevier.com/retrieve/pii/S0969806X18300641>
- [26] AdvanSiD, “RGB SiPMs - Chip Scale Package (CSP) - Datasheet,” May 2015. [Online]. Available: http://advansid.com/attachment/get/up_53_1432741078.pdf
- [27] D. Renker, “New trends on photodetectors,” *Nuclear Instruments and Methods in Physics Research Section A: Accelerators, Spectrometers, Detectors and Associated Equipment*, vol. 571, no. 1-2, pp. 1–6, Feb. 2007. [Online]. Available: <https://linkinghub.elsevier.com/retrieve/pii/S0168900206018134>
- [28] A. Kak and M. Slaney, *Principles of Computerized Tomographic Imaging*. Society of Industrial and Applied Mathematics, 2001. [Online]. Available: http://www.mat.uniroma2.it/~picard/SMC/didattica/materiali_did/Anal.Armon./Principles_of_CT_Imaging/Kak&Slaney-CTI-reduced.pdf
- [29] F. Natterer, *The Mathematics of Computerized Tomography*, ser. Classics in Applied Mathematics. Universität Münster: SIAM, 2001, vol. 32.
- [30] N. Otuka, E. Dupont, V. Semkova, B. Pritychenko, A. Blokhin, M. Aikawa, S. Babykina, M. Bossant, G. Chen, S. Dunaeva, R. Forrest, T. Fukahori, N. Furutachi, S. Ganesan, Z. Ge, O. Gritzay, M. Herman, S. Hlavač, K. Katō, B. Lalremruata, Y. Lee, A. Makinaga, K. Matsumoto, M. Mikhaylyukova, G. Pikulina, V. Pronyaev, A. Saxena, O. Schwerer, S. Simakov, N. Soppera, R. Suzuki, S. Takács, X. Tao, S. Taova, F. Tárkányi, V. Varlamov, J. Wang, S. Yang, V. Zerkin, and Y. Zhuang, “Towards a More Complete and Accurate Experimental Nuclear Reaction Data Library (EXFOR): International Collaboration Between Nuclear Reaction Data Centres (NRDC),” *Nuclear Data Sheets*, vol. 120, pp. 272–276, Jun. 2014. [Online]. Available: <https://linkinghub.elsevier.com/retrieve/pii/S0090375214005171>
- [31] J. F. Ziegler, M. D. Ziegler, and J. P. Biersack, “SRIM - The stopping and range of ions in matter (2010),” *Nuclear Instruments and Methods in Physics Research B*, vol. 268, pp. 1818–1823, Jun. 2010. [Online]. Available: <http://dx.doi.org/10.1016/j.nimb.2010.02.091>
- [32] C. M. Bartle, N. G. Chapman, and P. B. Johnson, “A study of deuterium implantation in a copper drive-in target,” *Nuclear Instruments and Methods*, vol. 95, no. 2, pp. 221–228, Aug. 1971. [Online]. Available: <http://www.sciencedirect.com/science/article/pii/0029554X71903697>
- [33] T. Shimizu, H. Sakane, S. Furuichi, M. Shibata, K. Kawade, and H. Takeuchi, “An improved pneumatic sample transport system for measurement of activation cross-sections with d-D neutrons in the energy range between 2.1 and 3.1mev,” *Nuclear Instruments and Methods in Physics Research Section A: Accelerators, Spectrometers, Detectors and Associated Equipment*, vol. 527, no. 3, pp. 543–553, Jul. 2004. [Online]. Available: <http://linkinghub.elsevier.com/retrieve/pii/S0168900204006205>
- [34] Y. Wu, “Development of a Compact Neutron Generator to be Used For Associated Particle Imaging Utilizing a RF-Driven Ion Source,” Ph.D. dissertation, University of California, Berkeley, Berkeley, Jan. 2009. [Online]. Available: <http://escholarship.org/uc/item/35w719tr>
- [35] O. Waldmann and B. Ludewigt, “Measurements of beam current density and proton fraction of a permanent-magnet microwave ion source,” *Review of Scientific Instruments*, vol. 82, no. 11, p. 113505, Nov. 2011. [Online]. Available: <http://aip.scitation.org/doi/10.1063/1.3660282>
- [36] P. Vacuum, “Pfeiffer PKR 251 pressure gauge,” 2019. [Online]. Available: https://www.idealvac.com/files/brochures/Pfeiffer_PKR_251_Pirani_ColdCathode.pdf

- [37] S.-A. R. LTD., “Instrument Manual for Seforad Fast Neutron Spectrometer, Model FNS-1 - Volume 2,” Seforad, Israel, Tech. Rep., 1985.
- [38] C. Industries, “Canberra Model 2022 Spectroscopy Amplifier,” 2010. [Online]. Available: <https://www3.nd.edu/~wzech/Model-2022-SS-M3833.pdf>
- [39] P. Technology, “PicoScope 5244a User’s Guide,” Pico Technology, United Kingdom, Tech. Rep. ps5000ab.en r5, Sep. 2017. [Online]. Available: <https://www.picotech.com/download/manuals/picoscope-5000-a-and-b-series-users-guide.pdf>
- [40] H. Kromer, R. Adams, B. Soubelet, and H.-M. Prasser, “Detailed characterization of a compact D-D fast neutron generator including total output, emitting spot, and energy spectrum,” *Applied Radiation and Isotopes*, vol. (submitted), 2019.
- [41] S. fun Electronics, “Stepper Motor - 68 oz.in (400 steps/rev) - ROB-10846.” [Online]. Available: <https://www.sparkfun.com/products/10846>
- [42] —, “Big Easy Driver - ROB-12859.” [Online]. Available: <https://www.sparkfun.com/products/12859>
- [43] Arduino.cc, “Getting Started with Arduino and Genuino UNO.” [Online]. Available: <https://www.arduino.cc/en/Guide/ArduinoUno>
- [44] T. R. P. Foundation, “Raspberry Pi 3 Model B.” [Online]. Available: <https://www.raspberrypi.org/products/raspberry-pi-3-model-b/>
- [45] Arduino.cc, “Getting started with the Arduino Due.” [Online]. Available: <https://www.arduino.cc/en/Guide/ArduinoDue>
- [46] The MathWorks, “MATLAB and Statistics Toolbox Release 2016a,” Natick, Massachusetts, United States, 2016. [Online]. Available: <https://ch.mathworks.com/de/>
- [47] T. Goorley, M. James, T. Booth, F. Brown, J. Bull, L. J. Cox, J. Durkee, J. Elson, M. Fensin, R. A. Forster, J. Hendricks, H. G. Hughes, R. Johns, B. Kiedrowski, R. Martz, S. Mashnik, G. McKinney, D. Pelowitz, R. Prael, J. Sweezy, L. Waters, T. Wilcox, and T. Zukaitis, “Initial MCNP6 Release Overview,” *Nuclear Technology*, vol. 180, no. 3, pp. 298–315, Dec. 2012. [Online]. Available: <http://epubs.ans.org/?a=15346>
- [48] B. E. Flores, “A pragmatic view of accuracy measurement in forecasting,” *Omega*, vol. 14, no. 2, pp. 93–98, Jan. 1986. [Online]. Available: <http://www.sciencedirect.com/science/article/pii/0305048386900137>
- [49] D. Ellison, *Handbook of Chemical and Biological Warfare Agents*. CRC Press, 2010. [Online]. Available: <https://books.google.ch/books?id=G4xKKcgWTrsC>
- [50] S. fun Electronics, “Stepper Motor - 125 oz.in (200 steps/rev, 600mm Wire) - ROB-13656 - SparkFun Electronics.” [Online]. Available: <https://www.sparkfun.com/products/13656>
- [51] R. Adams, R. Zboray, and H.-M. Prasser, “A novel fast-neutron tomography system based on a plastic scintillator array and a compact D–D neutron generator,” *Applied Radiation and Isotopes*, vol. 107, pp. 1–7, Jan. 2016. [Online]. Available: <http://linkinghub.elsevier.com/retrieve/pii/S0969804315301858>
- [52] “Thorlabs - CR1-Z7 Motorized Continuous Rotation Stage.” [Online]. Available: <https://www.thorlabs.com/thorproduct.cfm?partnumber=CR1-Z7>
- [53] “VirtualHere.” [Online]. Available: <http://www.virtualhere.com/home>

- [54] F. Kharfi, "Mathematics and Physics of Computed Tomography (CT): Demonstrations and Practical Examples," in *Imaging and Radioanalytical Techniques in Interdisciplinary Research - Fundamentals and Cutting Edge Applications*, F. Kharfi, Ed. InTech, Mar. 2013. [Online]. Available: <https://doi.org/10.5772/52351>
- [55] A. H. Andersen and A. C. Kak, "Simultaneous Algebraic Reconstruction Technique (SART): A superior implementation of the ART algorithm," *Ultrasonic Imaging*, vol. 6, no. 1, pp. 81–94, Jan. 1984. [Online]. Available: <http://www.sciencedirect.com/science/article/pii/0161734684900087>
- [56] T. Johnson, C. Fink, S. Schönberg, and M. Reiser, Eds., *Dual energy CT in clinical practice*, ser. Medical radiology Diagnostic imaging. Berlin Heidelberg: Springer, 2011, oCLC: 698505317.
- [57] R. C. Runkle, T. A. White, E. A. Miller, J. A. Caggiano, and B. A. Collins, "Photon and neutron interrogation techniques for chemical explosives detection in air cargo: A critical review," *Nuclear Instruments and Methods in Physics Research Section A: Accelerators, Spectrometers, Detectors and Associated Equipment*, vol. 603, no. 3, pp. 510–528, 2009. [Online]. Available: <http://www.sciencedirect.com/science/article/pii/S0168900209003489>
- [58] N. G. Cutmore, Y. Liu, and J. R. Tickner, "Development and commercialization of a fast-neutron/x-ray Cargo Scanner," in *2010 IEEE International Conference on Technologies for Homeland Security (HST)*, Nov. 2010, pp. 330–336. [Online]. Available: <http://dx.doi.org/10.1109/THS.2010.5655030>
- [59] M. Licata and M. Joyce, "Concealed nuclear material identification via combined fast-neutron/ γ -ray computed tomography (FNGCT): a Monte Carlo study," *Journal of Instrumentation*, vol. 13, no. 02, pp. P02 013–P02 013, Feb. 2018. [Online]. Available: <http://stacks.iop.org/1748-0221/13/i=02/a=P02013?key=crossref.8192412ccf8d6b310ae4ba697014ac39>
- [60] N. P. Shah, J. VanderZanden, and D. K. Wehe, "Design and construction of a 1-D, cylindrical, dual-particle, time-encoded imaging system," *Nuclear Instruments and Methods in Physics Research Section A: Accelerators, Spectrometers, Detectors and Associated Equipment*, Jan. 2019. [Online]. Available: <https://linkinghub.elsevier.com/retrieve/pii/S0168900219300385>
- [61] Technix, "HV power supply SR150kv-300w Datasheet." [Online]. Available: https://www.technix-hv.com/technix/sites/default/files/downloads/DATASHEET_SR-300-2000-W-SERIES_ENG.pdf
- [62] S. Industries, "Centurion™ Ultra-Compact, Relocatable, High Brightness 1-5 MeV-Class Linear Accelerator," 2019. [Online]. Available: http://www.starfireindustries.com/uploads/2/2/1/1/22111816/datasheet_centurion_rev01-19.pdf
- [63] C. Gongyin, "Fast neutron resonance radiography for elemental imaging: theory and applications," Ph.D. dissertation, MIT, Massachusetts Institute of Technology - Dept. of Nuclear Engineering., Jun. 2001. [Online]. Available: <https://dspace.mit.edu/handle/1721.1/8681>
- [64] M. Johnson, S. Anderson, D. Bleuel, P. Fitsos, D. Gibson, J. Hall, R. Marsh, B. Rusnak, and J. Sain, "Development of a High-brightness, Quasi-monoenergetic Neutron Source for Neutron Imaging," *Physics Procedia*, vol. 90, pp. 47–54, 2017. [Online]. Available: <http://linkinghub.elsevier.com/retrieve/pii/S1875389217301773>
- [65] D. Micieli, T. Minniti, L. M. Evans, and G. Gorini, "Accelerating Neutron Tomography experiments through Artificial Neural Network based reconstruction," *Scientific Reports*, vol. 9, no. 1, p. 2450, Dec. 2019. [Online]. Available: <http://www.nature.com/articles/s41598-019-38903-1>

Appendix A

Updated polynomial fit of the thin target neutron spectra

The absolute reference for DD and DT fusion reactions parameters were published in [3]. Based on these data, the neutron generator handbook [19] proposes a thorough analysis and practical results. A rigorous comparison of both publications revealed a discrepancy in the handbook, namely in the Legendre polynomial fit proposed in Table 3, page thirteen. The inconsistency is particularly obvious at 100 keV and 300 keV. The updated coefficients are available in Table A.1, the corresponding plots in Figure A.1.

Table A.1 – New Legendre polynomial fit for neutron spectrum with the thin target assumption.

E_d (keV)	A_0	A_1	A_2	A_3	A_4	A_5	σ (mb/sr)
50	1	0.03678	0.62429	0.12302	0.02695	0.00666	0.31540
100	1	0.01677	0.88146	0.22718	0.08599	0.03481	1.01990
200	1	-0.03324	1.11482	0.39478	0.26575	0.10907	1.94920
300	1	-0.07839	1.20527	0.46686	0.49426	0.25766	2.66480
400	1	-0.11194	1.21033	0.48585	0.75701	0.42904	3.21250
500	1	-0.10485	1.10193	0.30733	1.09383	0.75703	3.63090

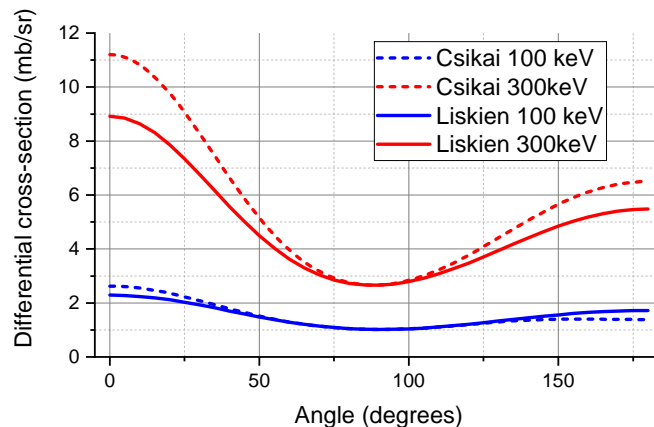


Figure A.1 – Comparison of the neutron spectrum before and after correction of the Legendre polynomials at 100 and 300 keV.

Appendix B

Scattering and nuclear reaction

B.1 Physics of neutron elastic scattering

The case is treated in the laboratory frame of reference. The figure B.1 gives an overview of the situation.

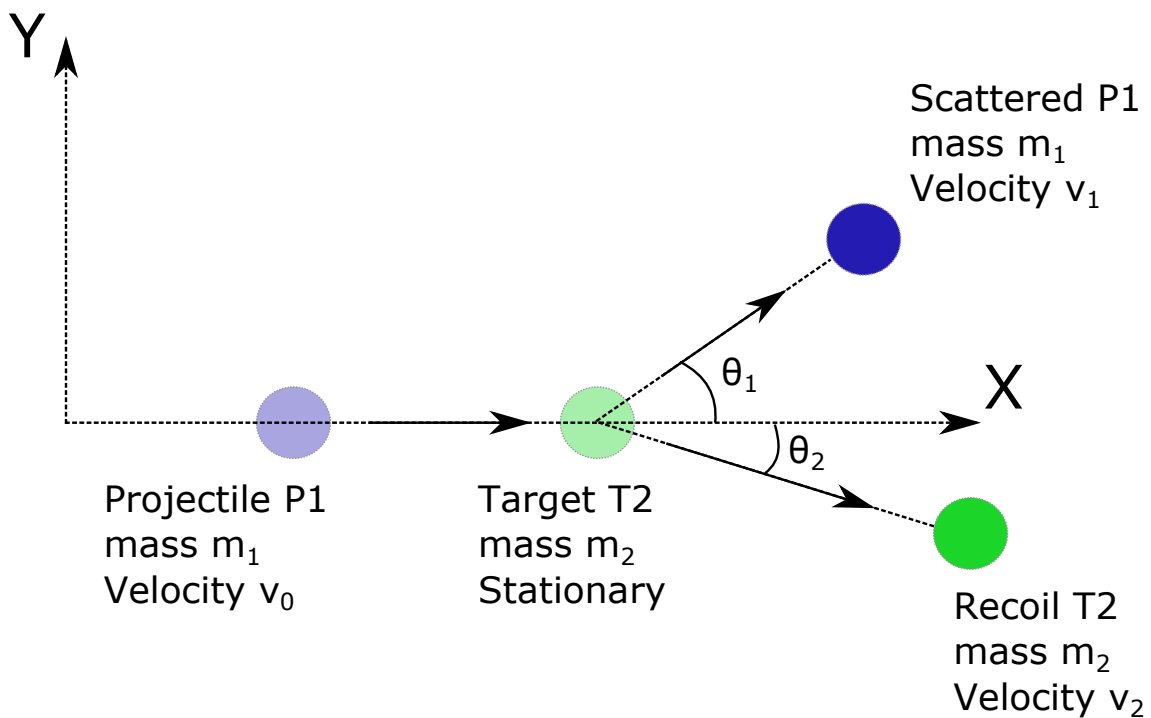


Figure B.1 – Scheme of an elastic scattering event. The least opaque disks indicate the position of the particles before impact, and the most opaque ones after impact.

It is assumed that a projectile P1 of mass m_1 and velocity v_0 is impinging on a stationary target T2 atom of mass m_2 and velocity thus equal to zero. It is also assumed that this is the case of elastic scattering, meaning the Q-value of the reaction is equal to zero; the binding energy (around ten eV) is negligible with respect to the kinetic energy; the case is considered as non-relativistic, it is thus valid for neutron energies below 20 MeV. After the collision, the direction of the scattered projectile P1 makes an angle θ_1 with its initial direction and has a velocity v_1 ; the recoiling atom T2 has an angle θ_2 with respect to the same reference and a velocity v_2 . The conservation of energy

gives:

$$\frac{1}{2}m_1v_0^2 = \frac{1}{2}m_1v_1^2 + \frac{1}{2}m_2v_2^2 \quad (\text{B.1})$$

Or if re-arranged:

$$v_2^2 = \frac{m_1}{m_2}(v_0^2 - v_1^2) \quad (\text{B.2})$$

And the conservation of momentum gives respectively along the X and Y axis:

$$m_1v_0 = m_1v_1\cos(\theta_1) + m_2v_2\cos(\theta_2) \quad (\text{B.3})$$

$$0 = m_1v_1\sin(\theta_1) - m_2v_2\sin(\theta_2) \quad (\text{B.4})$$

B.1.1 Projectile - scattered particle relation

First, a relation between the projectile energy and the scattered particle energy will be found, with any dependence with respect to the recoiling particle variables. The two previous equations B.3 and B.4 are squared (and in the first one, before squaring, the term $m_1v_1\cos(\theta_1)$ is moved to the left-hand side of the equation), they give respectively:

$$m_1^2v_0^2 + m_1^2v_1^2\cos^2(\theta_1) - 2m_1^2v_0v_1\cos(\theta_1) = m_2^2v_2^2\cos^2(\theta_2) \quad (\text{B.5})$$

$$m_1^2v_1^2\sin^2(\theta_1) = m_2^2v_2^2\sin^2(\theta_2) \quad (\text{B.6})$$

Then equations B.5 and B.6 are added; it yields:

$$m_1^2v_0^2 + m_1^2v_1^2(\cos^2(\theta_1) + \sin^2(\theta_1)) - 2m_1^2v_0v_1\cos(\theta_1) = m_2^2v_2^2(\cos^2(\theta_2) + \sin^2(\theta_2)) \quad (\text{B.7})$$

The trigonometry gives, for any angle α : $\cos^2(\alpha) + \sin^2(\alpha) = 1$, thus the equation B.7 can be simplified:

$$m_1^2v_0^2 + m_1^2v_1^2 - 2m_1^2v_0v_1\cos(\theta_1) = m_2^2v_2^2 \quad (\text{B.8})$$

Now, from equation B.2 v_2^2 is substituted in equation B.8, which then becomes:

$$m_1^2v_0^2 + m_1^2v_1^2 - 2m_1^2v_0v_1\cos(\theta_1) = m_1m_2(v_0^2 - v_1^2) \quad (\text{B.9})$$

Both sides of equation B.9 are divided by $m_1^2v_0^2$, which gives:

$$1 + \frac{v_1^2}{v_0^2} - 2\frac{v_1}{v_0}\cos(\theta_1) = \frac{m_2}{m_1}\left(1 - \frac{v_1^2}{v_0^2}\right) \quad (\text{B.10})$$

Re-arranging the terms and introducing the new variables $A = \frac{v_1}{v_0}$ and, the equation B.10 yields:

$$A^2\left(1 + \frac{m_2}{m_1}\right) - 2A\cos(\theta_1) + \left(1 - \frac{m_2}{m_1}\right) = 0 \quad (\text{B.11})$$

This is a second-order polynomial; assuming $\frac{m_2}{m_1} \geq 1$, the solution is:

$$A = \frac{2\cos(\theta_1) + \sqrt{4\cos^2(\theta_1) - 4(1 + \frac{m_2}{m_1})(1 - \frac{m_2}{m_1})}}{2(1 + \frac{m_2}{m_1})} \quad (\text{B.12})$$

Or if the equation B.12 is simplified and re-arranged (multiplying by $\frac{1}{2}\frac{m_1}{m_1}$ the right side of the equation, remembering that for any $a, b: (a + b)(a - b) = a^2 - b^2$ and that again, for any $\alpha: \cos(\alpha)^2 + \sin(\alpha)^2 = 1$):

$$A = \frac{m_1\cos(\theta_1) + \sqrt{-m_1^2\sin^2(\theta_1) + m_2^2}}{m_1 + m_2} \quad (\text{B.13})$$

The ratio of scattered particle energy and projectile energy is then:

$$\frac{E_1}{E_0} = \frac{\frac{1}{2}m_1v_1^2}{\frac{1}{2}m_1v_0^2} = A^2 = \left(\frac{m_1\cos(\theta_1) + \sqrt{m_2^2 - m_1^2\sin^2(\theta_1)}}{m_1 + m_2} \right)^2 \quad (\text{B.14})$$

B.1.2 Projectile - recoiling particle relation

If on the other hand, any reference to the scattered particle variables is to be removed, first the equation B.1 is re-arranged by multiplying both sides by $2m_1$:

$$(m_1v_0)^2 = (m_1v_1)^2 + m_1m_2v_2^2 \quad (\text{B.15})$$

Then the equations B.3 and B.4 are squared (and in the first one, before squaring, the term $m_2v_2\cos(\theta_2)$ is moved to the left-hand side of the equation), they give respectively:

$$m_1^2v_0^2 + m_2^2v_2^2\cos^2(\theta_2) - 2m_1m_2v_0v_2\cos(\theta_2) = m_1^2v_1^2\cos^2(\theta_1) \quad (\text{B.16})$$

$$m_1^2v_1^2\sin^2(\theta_1) = m_2^2v_2^2\sin^2(\theta_2) \quad (\text{B.17})$$

If now equations B.16 and B.17 are added, remembering that for any angle $\alpha: \cos(\alpha)^2 + \sin(\alpha)^2 = 1$:

$$m_1^2v_0^2 + m_2^2v_2^2 - 2m_1m_2v_0v_2\cos(\theta_2) = m_1^2v_1^2 \quad (\text{B.18})$$

From equation B.15, the term $m_1^2v_0^2$ is substituted in equation B.18:

$$m_1m_2v_2^2 + m_2^2v_2^2 - 2m_1m_2v_0v_2\cos(\theta_2) = 0 \quad (\text{B.19})$$

Simplifying equation B.19 yields:

$$\frac{v_2}{v_0} = \frac{2m_1\cos(\theta_2)}{m_1 + m_2} \quad (\text{B.20})$$

The ratio of energies between recoil particle and projectile is then:

$$\frac{E_2}{E_0} = \frac{\frac{1}{2}m_2v_2^2}{\frac{1}{2}m_1v_0^2} = \frac{m_2}{m_1} \frac{v_2^2}{v_0^2} = \frac{4m_1m_2\cos^2(\theta_2)}{(m_1 + m_2)^2} \quad (\text{B.21})$$

In the specific case of a neutron elastically scattering with a proton, assuming their masses are identical¹, the equation B.21 boils down to:

$$\frac{E_2}{E_0} = \cos^2(\theta_2) \quad (\text{B.22})$$

¹This is not exactly true as the proton has a rest mass of 938.3 MeV against 939.6 MeV for the neutron.

B.2 Physics of nuclear reaction

In this section, the laws governing a general nuclear reaction will be presented. The reaction $P + T \rightarrow S + R$ is considered in the laboratory frame of reference, as illustrated in figure B.2:

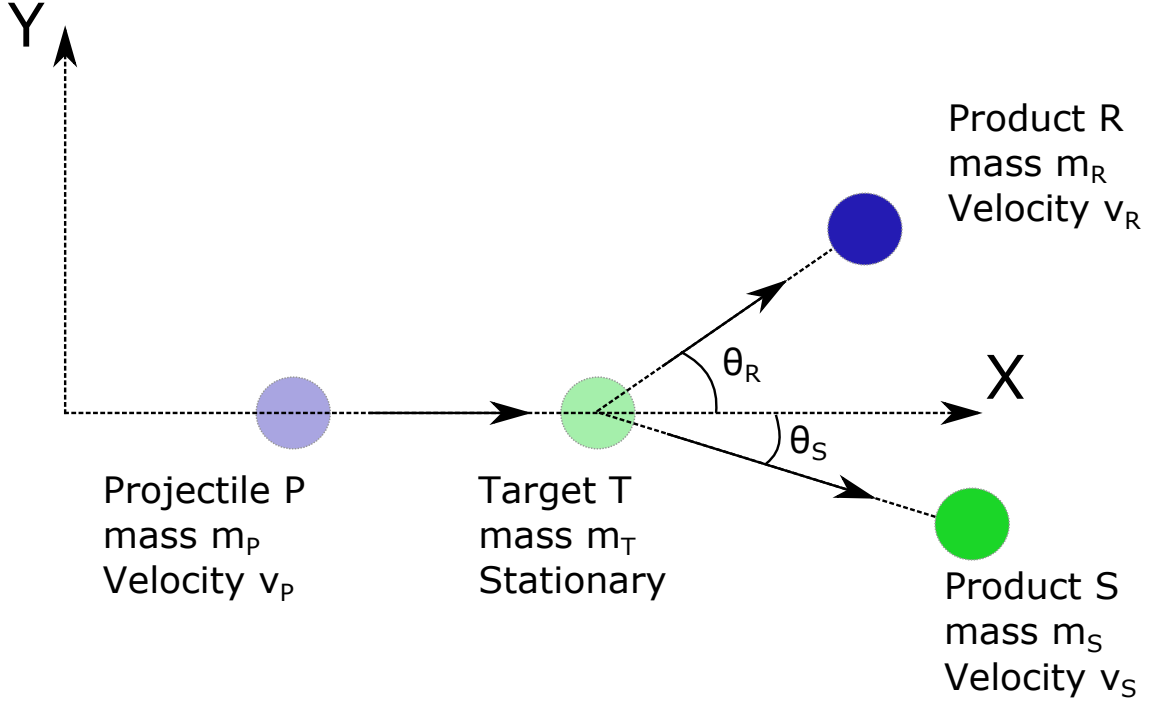


Figure B.2 – Scheme of a general nuclear reaction. The least opaque disks indicate the position of the particles before reaction, and the most opaque ones after.

The mass and velocity of each particle carries the corresponding index². The Q-value is not assumed to be zero and can be determined from the difference of masses³ between products and reactants of the reaction:

$$Q_{\text{value}} = m_P c^2 + m_T c^2 - m_S c^2 - m_R c^2 \quad (\text{B.23})$$

It is recalled that the electron binding energy is neglected; and that the target is stationary, having then a kinetic energy equal to zero; the case is supposed to be non-relativistic, and thus can be well approximated by a classical mechanics approach. The conservation of energy can be written as the balance between the mass change and the kinetic energies:

$$m_P c^2 + m_T c^2 + \frac{1}{2} m_P v_P^2 = m_S c^2 + m_R c^2 + \frac{1}{2} m_S v_S^2 + \frac{1}{2} m_R v_R^2 \quad (\text{B.24})$$

The previous equation B.24 can be re-written considering the definition of the Q-value introduced in equation B.23. The notation $K_i = \frac{1}{2} m_i v_i^2$ is also introduced to design the kinetic energy of the specie i .

$$Q_{\text{value}} = K_S + K_R - K_P \quad (\text{B.25})$$

²E.g. the incoming particle P has a mass m_P and a velocity v_P .

³Converted in energies through Einstein's mass-energy equivalence $E_{\text{particle}} = m_{\text{particle}} * c^2$.

Similarly to the the case of elastic scattering described in section B.1, the conservation of momentum can be written in the (X,Y) frame:

$$m_P v_P = m_R v_R \cos(\theta_R) + m_S v_S \cos(\theta_S) \quad (\text{B.26})$$

$$0 = m_R v_R \sin(\theta_R) - m_S v_S \sin(\theta_S) \quad (\text{B.27})$$

The momentum p_i of the species i are re-written so as to make their kinetic energies appear through $K_i = \frac{1}{2} m_i v_i^2 = \frac{1}{2 m_i} p_i^2$. The two previous equations B.26 and B.27 become respectively, with some term re-arrangement on each side:

$$\sqrt{2 m_P K_P} - \sqrt{2 m_R K_R \cos(\theta_R)} = \sqrt{2 m_S K_S \cos(\theta_S)} \quad (\text{B.28})$$

$$\sqrt{2 m_R K_R \sin(\theta_R)} = \sqrt{2 m_S K_S \sin(\theta_S)} \quad (\text{B.29})$$

Now the two equations B.28 and B.29 are squared:

$$\begin{aligned} 2 m_P K_P - 2 * \sqrt{2 m_P K_P} * \sqrt{2 m_R K_R \cos(\theta_R)} + 2 m_R K_R \cos(\theta_R)^2 \\ = 2 m_S K_S \cos(\theta_S)^2 \end{aligned} \quad (\text{B.30})$$

$$2 m_R K_R \sin(\theta_R)^2 = 2 m_S K_S \sin(\theta_S)^2 \quad (\text{B.31})$$

Equations B.30 and B.31 are then added (it is recalled that for any angle α : $\cos(\alpha)^2 + \sin(\alpha)^2 = 1$):

$$m_P K_P - 2 \sqrt{m_P K_P m_R K_R \cos(\theta_R)} + m_R K_R = m_S K_S \quad (\text{B.32})$$

The relation between kinetic energies and Q-value found in equation B.25 is used in equation B.32 to substitute K_S :

$$m_P K_P - 2 \sqrt{m_P K_P m_R K_R \cos(\theta_R)} + m_R K_R = m_S (Q - K_R + K_P) \quad (\text{B.33})$$

Or if equation B.33 is considered as a second-order polynomial of the variable $\sqrt{K_R}$:

$$\begin{aligned} (m_R + m_S) \sqrt{K_R}^2 \\ - 2 \sqrt{m_P K_P m_R \cos(\theta_R)} * \sqrt{K_R} + (m_S K_P - m_P K_P - m_S Q) = 0 \end{aligned} \quad (\text{B.34})$$

The solution of this polynomial is then:

$$\begin{aligned} \sqrt{K_R} = \frac{\sqrt{m_P m_R K_P \cos(\theta_R)}}{m_R + m_S} \\ + / - \frac{\sqrt{m_P m_R K_P \cos(\theta_R)^2 + (m_R + m_S)(m_S Q + K_P(m_S - m_P))}}{m_R + m_S} \end{aligned} \quad (\text{B.35})$$

In the case of a deuterium-deuterium fusion reaction, P and T are both deuterium nucleus of mass m_d , the incoming deuterium nucleus having an energy E_d . R is a neutron of mass m_n and energy E_n , flying in the direction defined by θ_n . S is a Helium-3 nucleus of mass m_H . The Q-value is

positive and denoted Q_{DD} , which means that the polynomial solution is only the version with the sign “+”. Thus equation B.35 becomes:

$$\sqrt{E_n} = \frac{\sqrt{m_d m_n E_d \cos(\theta_n)}}{m_n + m_H} + \frac{\sqrt{m_d m_n E_d \cos(\theta_n)^2 + (m_n + m_H)(m_H Q_{\text{DD}} + E_d(m_H - m_d))}}{m_n + m_H} \quad (\text{B.36})$$

Appendix C

Error propagation

Change standard deviation to another var name, to avoid confusion with XS

The error uncertainty of a function A , function of the variables X_i can be computed with the following formula:

$$\kappa_A = \sqrt{\sum_i \left(\left(\frac{\partial A}{\partial X_i} \right)^2 \cdot \kappa_{X_i}^2 \right)} \quad (\text{C.1})$$

For a number of events large enough - for example N counts - the Poisson distribution describing the spread of the count amplitudes can be very well approximated by a normal distribution with a standard deviation:

$$\kappa_N \approx \sqrt{N} \quad (\text{C.2})$$

Considering the case of transmission imaging measurements, the main detector count N_{main} is always normalized to a fixed reference N_{ref} to account for flux variations from the generator itself. Therefore according to equation C.1:

$$N_{\text{normalized}} = \frac{N_{\text{main}}}{N_{\text{ref}}} \rightarrow \kappa_{N_{\text{normalized}}}^2 = \frac{\kappa_{N_{\text{main}}}^2}{N_{\text{ref}}^2} + \frac{N_{\text{main}}^2 \cdot \kappa_{N_{\text{ref}}}^2}{N_{\text{ref}}^4} \quad (\text{C.3})$$

Considering that equation C.2 is applicable - i.e. $\kappa_{N_{\text{ref}}}^2 \approx N_{\text{ref}}$ and $\kappa_{N_{\text{main}}}^2 \approx N_{\text{main}}$ - then equation C.3 can be simplified into:

$$\kappa_{N_{\text{normalized}}}^2 = \frac{N_{\text{main}}}{N_{\text{ref}}^2} + \frac{N_{\text{main}}^2}{N_{\text{ref}}^3} \quad (\text{C.4})$$

In order to account for the room scattering, three separated sets of measurement are needed for each sample: the sample measurement B (the sample to be measured is covering the field of view), the flat field C (the field of view of the detector is completely free of any obstacle) and the blinding cone D (a thick high-density polyethylene block removes all the direct beam contribution). The final attenuation ratio A that is computed is as follows:

$$A = \frac{B - C}{D - C} \quad (\text{C.5})$$

Therefore, according to equation C.1, equation C.5 can be written as:

$$\kappa_A^2 = \left(\frac{\partial A}{\partial B} \right)^2 \cdot \kappa_B^2 + \left(\frac{\partial A}{\partial C} \right)^2 \cdot \kappa_C^2 + \left(\frac{\partial A}{\partial D} \right)^2 \cdot \kappa_D^2 \quad (\text{C.6})$$

And since:

$$\frac{\partial A}{\partial B} = \frac{1}{D-C} \quad \frac{\partial A}{\partial C} = \frac{B-D}{(D-C)^2} \quad \frac{\partial A}{\partial D} = \frac{C-B}{(D-C)^2} \quad (\text{C.7})$$

Then equation C.6 becomes:

$$\kappa_A^2 = \left(\frac{1}{D-C}\right)^2 \cdot \kappa_B^2 + \left(\frac{B-D}{(D-C)^2}\right)^2 \cdot \kappa_C^2 + \left(\frac{C-B}{(D-C)^2}\right)^2 \cdot \kappa_D^2 \quad (\text{C.8})$$

Therefore the relative standard deviation can be obtained by dividing both sides by $A^2 \equiv \left(\frac{B-C}{D-C}\right)^2$:

$$\frac{\kappa_A^2}{A^2} = \left(\frac{D-C}{B-C}\right)^2 \cdot \left[\left(\frac{1}{D-C}\right)^2 \cdot \kappa_B^2 + \left(\frac{B-D}{(D-C)^2}\right)^2 \cdot \kappa_C^2 + \left(\frac{C-B}{(D-C)^2}\right)^2 \cdot \kappa_D^2 \right] \quad (\text{C.9})$$

Which can be simplified to:

$$\frac{\kappa_A^2}{A^2} = \left(\frac{\kappa_B}{B-C}\right)^2 + \left(\frac{(B-D) \cdot \kappa_C}{(B-C)(D-C)}\right)^2 + \left(\frac{\kappa_D}{(D-C)}\right)^2 \quad (\text{C.10})$$

So in the end, the relative standard deviation is:

$$\frac{\kappa_A}{A} = \sqrt{\left(\frac{\kappa_B}{B-C}\right)^2 + \left(\frac{(B-D) \cdot \kappa_C}{(B-C)(D-C)}\right)^2 + \left(\frac{\kappa_D}{(D-C)}\right)^2} \quad (\text{C.11})$$

Each of the variables κ_B , κ_C and κ_D can be computed based on the absolute count values B , C and D thanks to equation C.4.

Finally, to propagate the error to the target variable in the case of a sample of thickness τ , it should be reminded that the total macroscopic cross-section κ_t can be computed through Equation C.12.

$$\kappa_t = -\frac{1}{\tau} \cdot \ln(A) \quad (\text{C.12})$$

Applying the Formula C.1 to Equation C.12 yields the following relation for the error on the macroscopic cross-section:

$$\kappa_{\kappa_t} = \frac{1}{\tau} \cdot \frac{\kappa_A}{A} \quad (\text{C.13})$$

Appendix D

Impurities in a reference sample

By definition, the number of moles of the molecule per unit of volume in a sample n_V is equal to the ratio between the density ρ and the molar mass M or to the ratio between the number of molecules per unit of volume N_V and Avogadro's number N_A :

$$n_V \equiv \frac{\rho}{M} \equiv \frac{N_V}{N_A} \quad (\text{D.1})$$

From Equation D.1, it can easily be deduced that:

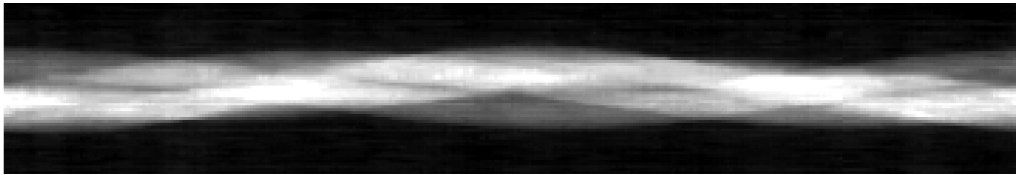
$$N_V = \frac{\rho \cdot N_A}{M} \quad (\text{D.2})$$

From Equation D.2 and taking the example of an Aluminium Nitride - AlN sample, with a density of 3.375 g.cm^{-3} , a molar mass of 41 g.mol^{-1} , and a purity of 98%, it means that there are $4.86 \cdot 10^{22}$ molecules of AlN per cubic centimeters, or $9.72 \cdot 10^{22}$ atoms of Al and N combined per cubic centimeters. If the 2% remaining percent are only made of hydrogen, then it represents $4.06 \cdot 10^{22}$ atoms per cubic centimeters, or 29.5% of the total amounts of atoms.

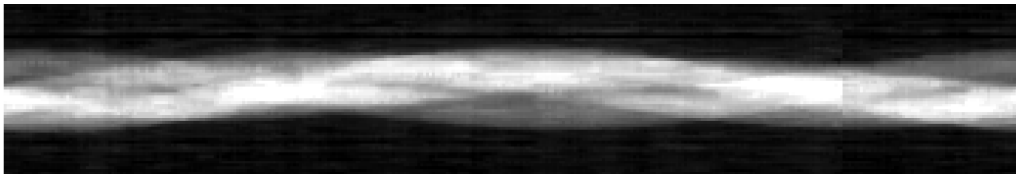
Appendix E

Sinograms of the CT data

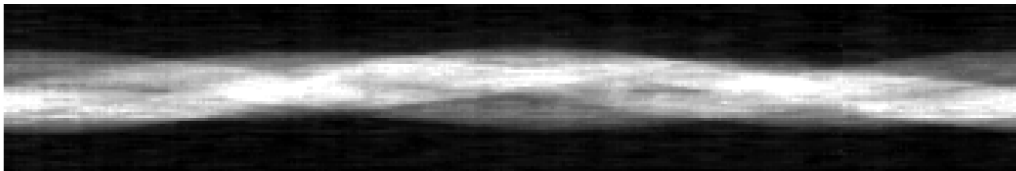
E.1 Sinograms of Sample Set 1



(a) Trolley at 0° , sinogram.



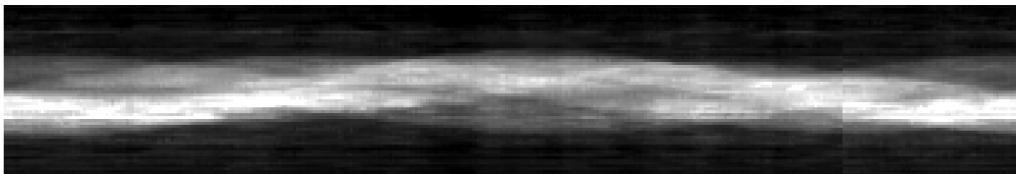
(b) Trolley at 40° , sinogram.



(c) Trolley at 60° , sinogram.



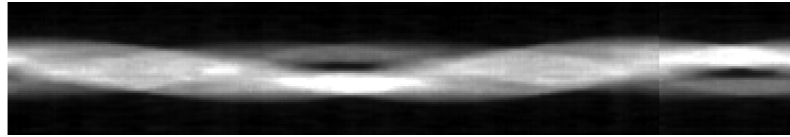
(d) Trolley at 90° , sinogram.



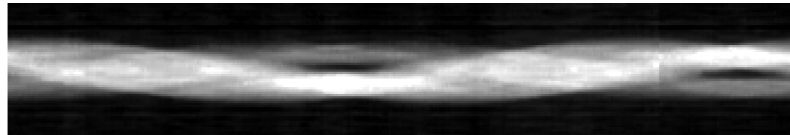
(e) Trolley at 115° , sinogram.

Figure E.1 – Sinograms of Sample Set 1 at 0, 40, 60, 90 and 115° .

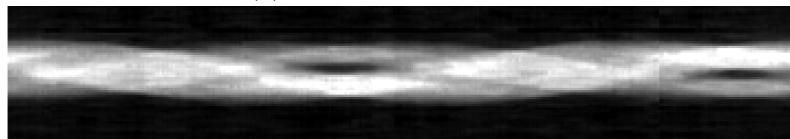
E.2 Sinograms of Sample Set 2



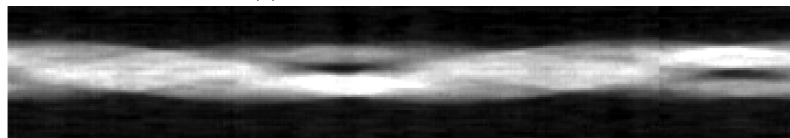
(a) Trolley at 0° , sinogram.



(b) Trolley at 40° , sinogram.



(c) Trolley at 60° , sinogram.



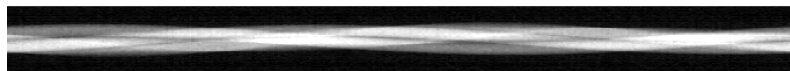
(d) Trolley at 90° , sinogram.



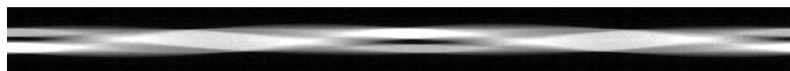
(e) Trolley at 115° , sinogram.

Figure E.2 – Sinograms of Sample Set 2 at 0° , 40° , 60° , 90° and 115° .

E.3 Sinograms with the Co-60 source



(a) Sample Set 1, with the Co-60 source, sinogram.



(b) Trolley at 115° , sinogram.

Figure E.3 – Sample Set 2, with the Co-60 source, sinogram.

BENOIT SOUBELET



Nuclear engineer, PhD candidate in nuclear engineering

📧 benoit.soubelet@gmail.com

☎ +41 79 138 05 25

🏠 Grünaustrasse 4, 8953 Dietikon, Switzerland

🌐 benoit-soubelet.synology.me

🌐 benoit-soubelet-6285a045

📅 France, February 3rd, 1991

🇫🇷 French national, B Swiss residence permit

EXPERIENCE

PhD candidate in nuclear engineering

ETH Zürich - Department of Mechanical and Process Engineering - Laboratory of Nuclear Energy Systems

📅 2015 - 2020

📍 Villigen, Switzerland

- "Development of energy-selective fast neutron imaging for nondestructive elemental analysis".
- Unique method giving contrast for heavily shielded samples where standard X-rays fail.
- Applications in: homeland security, oil industry, etc.
- Complementary approach with experimental work, computer simulations and theory.

Teaching assistant

ETH Zürich

📅 2018 - 2019

📍 Zürich, Switzerland

- Course: "Radiation-based imaging methods for nuclear and industrial applications".
- Preparation and animation of lectures and exercise sessions.

Intern

Paul Scherrer Institute - Center for Proton Therapy

📅 July 2014 - October 2014

📍 Villigen, Switzerland

- Nuclear interactions in pencil beams: predictions for Gantry-2 using state-of-the-art Monte Carlo simulations (Fluka and Geant4).

Intern

Sobegi - Methods and maintenance service

📅 May 2013 - August 2013

📍 Lacq, France

- Review and documentation of the cooling system of the onshore gas extraction platform.

Intern

Pharmaceutical laboratory Bioluz - Maintenance service

📅 January 2012 - February 2012

📍 St-Jean-de-Luz, France

- Review and documentation of the new production line.

Deputy policeman

Saint-Jean-de-Luz city hall

📅 Summer 2009 and 2010

📍 St-Jean-de-Luz, France

- Summer reinforcement. Patrolling and public information.

LIFE PHILOSOPHY

"I have a dream today." - Martin Luther King Jr.

EDUCATION

Dr.Sc. in Nuclear Engineering

ETH Zürich

📅 2015 - 2020

📍 Villigen, Switzerland

M.Sc. in Nuclear Engineering

ETH Zürich and EPF Lausanne

📅 2013 - 2015

📍 Zürich, Switzerland

- "Development of a new Open source tool for multi-physics analysis of a sodium-cooled fast reactor"

B.Sc. and M.Sc. in Engineering

Ecole Centrale de Lille

📅 2011 - 2013

📍 Lille, France

Higher School Preparatory Classes

Lycée Michel Montaigne

📅 2009 - 2011

📍 Bordeaux, France

High School Diploma

Lycée de la Sauque

📅 2009

📍 La Brède, France

EXTRACURRICULAR



Horse rider

for many years



Hiking and skiing fan

throughout the Alps



Avid traveller

and amateur photographer



Space enthusiast

The final frontier



Book lover

From Science Fiction to classic books

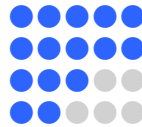
PRACTICAL SKILLS

Windows & Linux OS, Bash scripting, Microsoft Office
Programming (Matlab, Arduino, etc.)
Workshop skills (CAD design, CNC machining, 3D printing)
Nuclear engineering software (MCNP, CASMO, etc.)
Web design (HTML, CSS, JavaScript, PHP, SQL)



LANGUAGES

French (native)
English
German
Spanish



STRENGTHS

Enthusiastic Creative Adaptable Solution-oriented
Organized Reliable Autonomous

SELECTED PUBLICATIONS

Review Articles

- Kromer, Heiko, Robert Adams, Benoit Soubelet, and Horst-Michael Prasser (2019). "Detailed characterization of a compact D-D fast neutron generator including total output, emitting spot, and energy spectrum". In: *Applied Radiation and Isotopes* (submitted).
- Kromer, Heiko, Robert Adams, Benoit Soubelet, Robert Zboray, et al. (2019). "Thermal analysis, design, and testing of a rotating beam target for a compact D-D fast neutron generator". In: *Applied Radiation and Isotopes* 145, pp. 47–54. DOI: 10.1016/j.apradiso.2018.12.009.
- Soubelet, Benoit, Robert Adams, Heiko Kromer, et al. (2019). "Calibration technique and sample measurement database for material decomposition imaging using a compact deuterium-deuterium (D-D) fast neutron generator". In: *Radiation Physics and Chemistry* (submitted).
- Soubelet, Benoit, Robert Adams, and Horst-Michael Prasser (2019). "Computed tomography associated to a material decomposition technique using a compact deuterium-deuterium (D-D) fast neutron generator". In: *Radiation Physics and Chemistry* (not yet submitted).
- Soubelet, B. et al. (2019). "Feasibility study of using a compact deuterium-deuterium (D-D) neutron generator for energy-selective transmission tomography". In: *Radiation Physics and Chemistry* 156, pp. 292–299. DOI: 10.1016/j.radphyschem.2018.11.017.

PROJECTS

Deputy director

PolyHACK

 2018

 Zürich, Switzerland

- Organization of a 100-participant hackathon at ETH Zürich, focused on the applications of drones.
- Coordination of the logistics and of the team of volunteers.
- Main partners: ELCA, Sunflower Labs, EWAT, Verity Studios.
- Budget: 35'000 CHF.

Educative project

Ecole Centrale de Lille

 2011 – 2013

 Lille, France

- Glucodata: digital solution for gestational diabetes monitoring.
- Partnership with the regional hospital of Lille and the laboratory Roche.
- Management of a seven-member team.
- Budget: 20'000 €.

REFERENCES

Available upon request.

Title of work:

Development of energy-selective fast neutron imaging for non-destructive elemental analysis

Date:

2020

Jury:

Prof. Dr. Horst-Michael Prasser, examiner

Prof. Dr. Igor Jovanovic, co-examiner

Dr. Volker Dangendorf, co-examiner

Doctoral student:

Name: Benoit Pierre Soubelet
E-mail: sbenoit@lke.mavt.ethz.ch
Legi-Nr.: 13-802-897

Statement regarding plagiarism:

By signing this statement, I affirm that I have read and signed the Declaration of Originality, independently produced this paper, and adhered to the general practice of source citation in this subject-area.

Declaration of Originality:

http://www.ethz.ch/faculty/exams/plagiarism/confirmation_en.pdf

Zürich, 2020: _____